UCL Université catholique de Louvain

École polytechnique de Louvain (EPL)

epl

Development of a humanoid walker: simulation, control and design

Dissertation presented by
Sophie MAENHOUT, Simon RAUCQ

for obtaining the Master's degree in
Electro-mechanical Engineering

Supervisor(s)
Renaud RONSSE

Reader(s)
Paul FISETTE, Benoît RAUCENT, Nicolas VAN DER NOOT

Academic year 2016-2017

Acknowledgements

We would like to thank all people that helped us realising this master thesis.

First, we thank our supervisor, Professor Renaud Ronsse, who guided and advised us all along our work, allowing us to achieve our objectives.

We also thank Christophe Everarts and Nicolas Van der Noot for their great help and their availability. On the one hand, the advice of Christophe and his work were very useful for the design of our robot. On the other hand, the advice of Nicolas was also very helpful as well as the implementation of his controller, that was largely taken up in our work.

Moreover, we thank Aubain Verlé for his aid during the design process and François Heremans for his help regarding the simulation.

We also thank the Ecole Polytechnique de Louvain of the Université Catholique de Louvain for the university training we received and without which we could not have realised this master thesis.

Finally, we wish to thank our families and our friends for their continuous support and their encouragements throughout the elaboration of our master thesis.

Contents

Nomenclature

Abbreviations

Abbrv.	Description
AMBER	Advanced Mechanical Bipedal Experimental Robotics
BE	Buffer Elasticity
CAES	Compressed Air Energy Storage
CE	Contractile Element
CMA-ES	Covariance Matrix Adaptation Evolution Strategy
COMAN	COmpliant huMANoid
CVT	Continuously Variable Transmission
DARPA	Defense Advanced Research Projects Agency
DRC	DARPA Robotics Challenge
ECD	Electric Cable Differential
GAS	Biarticular GAStrocnemius muscle
GLU	GLUteus muscle group
HAM	Biarticular HAMstring muscle group
HFL	Hip FLexor muscle group
HZD	Hybrid Zero Dynamics
IIT	Italian Institute of Technology
IM-RMM	Ideal Model Resolved Motion Method
IVT	Infinitely Variable Transmission
JSK	Jouhou System Kougaku
MIT	Massachusetts Institute of Technology
MTU	Muscle-Tendon Unit
PE	Parallel Elasticity
PG	Planetary Gears
SE	Series Elasticity

SEA	Series Elastic Actuator
TO	Take Off
VAS	VASti muscle group
VSA	Variable Stiffness Actuator

Greek Symbols

Symbol	Description	Units
α	Tilt angle of the cones' shaft w.r.t. the sun in the CVT	$[rad]$
β	Inner factor of the hyperbolic tangent of the ground contact model	$[-]$
$\Delta\phi_k$	Knee's angle w.r.t. $\phi_{k,off}$	$[rad]$
Δt_m	Time delay of muscle m	$[s]$
$\dot{\theta}$	Derivative of the trunk's forward lean angle w.r.t. time	$[rad]$
η_{hip}	Powertrain mechanical efficiency to the hip joint	$[-]$
η_i	Mechanical efficiency of the element i	$[-]$
η_{knee}	Powertrain mechanical efficiency to the knee joint	$[-]$
γ	Ratio between maximum and minimum output torque in the IVT	$[-]$
λ	Parameter in the Hertz theory	$[-]$
μ	Friction coefficient of traction fluids	$[-]$
μ_{max}	Maximal value for the friction coefficient of the ground contact model	$[-]$
ν	Poisson's coefficient of a material	$[-]$
ω_1	Angular velocity of the sun in the PG	$[rad\,s^{-1}]$
ω_3	Angular velocity of the ring in the PG	$[rad\,s^{-1}]$
ω_4	Angular velocity of the planets carrier in the PG	$[rad\,s^{-1}]$
ω_5	Angular velocity of the sun in the CVT	$[rad\,s^{-1}]$
ω_7	Angular velocity of the ring in the CVT	$[rad\,s^{-1}]$
ω_8	Angular velocity of the planets carrier in the CVT	$[rad\,s^{-1}]$
ω_{screw}	Angular velocity required at the screw thread	$[rad\,s^{-1}]$
ϕ	Angular positions of the joints of the bipedal robot	$[rad]$
ϕ_k	Knee's angle	$[rad]$
$\phi_{k,off}$	Knee angle threshold related to its overextension	$[rad]$
ϕ_{max}	Threshold of angular positions of the joints	$[rad]$
σ_y	Yield strength of a material	$[Pa]$
σ_{max}	Maximum Hertzian stress	$[Pa]$
τ	Transmission ratio of the series of planetary gears	$[-]$

τ_m	Torque of muscle m	$[N\,m]$
τ_{CVT}	Transmission ratio of the CVT	$[-]$
$\tau_{joints,ref}$	Referential torques from the high level controller to apply to the joints	$[N\,m]$
τ_{joints}	Torques from the mid-level controller applied to the joints	$[N\,m]$
τ_{PG}	Planetary gears' train value	$[-]$
θ	Trunk's forward lean angle w.r.t. gravity	$[rad]$
θ_{ref}	Trunk's pitch at take off	$[rad]$

Roman Symbols

Symbol	Description	Units
$\dot{V}$	Derivative of V w.r.t. time	$[m^3\,s^{-1}]$
κ	Parameter in the Hertz theory	$[-]$
a	Half length of the long axis of the ellipsoid contact patch in the Hertz theory	$[m]$
b	Half length of the short axis of the ellipsoid contact patch in the Hertz theory	$[m]$
$B+A$	Parameter in the Hertz theory	$[-]$
$B-A$	Parameter in the Hertz theory	$[-]$
b_l	Barrel length for the spiral spring	$[m]$
C	Spring index	$[-]$
c	Distance between the neutral fibre and the edge of a rectangular bar	$[m]$
D	Resume of material characteristics	$[Pa^{-1}$
d	Distance travelled	$[m]$
D_a	Arbor diameter for the spiral spring	$[m]$
D_b	Barrel diameter for the spiral spring	$[m]$
D_s	Inner diameter of the stack of the spiral spring	$[m]$
d_{nom}	Nominal diameter of the thread	$[m]$
E	Young modulus	$[Pa]$
e_{15m}	Energy consumption of the robot after 15 [m] of travel	$[J\,m^{-1}]$
e_{7m}	Energy consumption of the robot after 7 [m] of travel	$[J\,m^{-1}]$
e_{dist}	Energy consumption per distance	$[J\,m^{-1}]$
$F+$	Positive force feedback	$[N]$
F_1	Tangential force on the sun in the planetary gears	$[N]$
F_3	Tangential force on the ring in the planetary gears	$[N]$
F_4	Tangential force on the planets carrier in the planetary gears	$[N]$

F_5	Tangential force between the cones and the sun in the CVT	$[N]$
F_6	Tangential force between the cones and the roller in the CVT	$[N]$
F_c	Contact force in Hertz theory	$[N]$
F_m	Force of muscle m	$[N]$
F_N	Normal ground contact force	$[N]$
F_s	Axial force applied to the sun in the CVT	$[N]$
F_t	Tangential ground contact force	$[N]$
$f_{distance}$	Fitness value related to the travelled distance	$[-]$
f_{energy}	Fitness value related to the energy consumption	$[-]$
F_{rc}	Tangential contact force in the roller/cones contact in the CVT	$[N]$
F_{rs}	Tangential contact force in the sun/cones contact in the CVT	$[N]$
f_{time}	Fitness value related to the walking time	$[-]$
F_x	Force of element x	$[N]$
G_m	Gain of muscle m	$[-]$
h	Thickness of the spiral spring	$[m]$
I	Moment of inertia of a rectangular area	$[kg\,m^2]$
K_D	Normal damping coefficient of the ground contact model	$[-]$
K_P	Normal stiffness coefficient of the ground contact model	$[-]$
k_s	Safety factor	$[-]$
k_{spring}	Stiffness of the spiral spring	$[N\,m\,rad^{-1}]$
L	Length of the spiral spring	$[m]$
$L+$	Positive length feedback	$[m]$
$l_{CE,m}$	Fibre length of muscle m	$[m]$
$l_{off,m}$	Offset length of muscle m	$[m]$
l_{opt}	Optimal length of CE	$[m]$
l_{slack}	Slack length of SE	$[m]$
lim_{travel}	Minimal distance to travel	$[m]$
M	Mass of the robot	$[kg]$
m	Module of a set of gears	$[-]$
m_r	Mass of the ring in the CVT	$[kg]$
n	Number of planets in the PG	$[-]$
N_1	Number of teeth of the sun in the PG	$[-]$
N_2	Number of teeth of the planets in contact with the sun in the PG	$[-]$

N_3	Number of teeth of the ring in the PG	$[-]$
N_p	Number of teeth of the planets in the planetary gears	$[-]$
N_r	Number of teeth of the ring in the planetary gears	$[-]$
N_s	Number of teeth of the sun in the planetary gears	$[-]$
$N_{2'}$	Number of teeth of the planets in contact with the ring in the PG	$[-]$
P	Power profile of the joint	$[W]$
p	Pitch of the thread	$[m]$
P_m	Mean power delivered by the main motor	$[W]$
$P_{m,IVT}$	Power of the motor controlling the IVT's transmission ratio	$[W]$
q	Generalised coordinates of the bipedal robot in Robotran	$[rad]/[m]$
qd	Generalised velocities of the bipedal robot in Robotran	$[rad\,s^{-1}]/[m\,s^{-1}]$
Qq	Joints' torque in Robotran	$[N\,m]$
$R2$	Lean angle of the trunk w.r.t. the inertial frame	$[rad]$
R_1	Pitch radius of the sun in the PG	$[m]$
R_3	Pitch radius of the ring in the PG	$[m]$
R_4	Radius of the planets carrier in the planetary gears	$[m]$
R_5	Radius of the sun/cones contact point w.r.t. the sun's axis in the CVT	$[m]$
R_6	Radius of the sun/cones contact point w.r.t. the cones' axis in the CVT	$[m]$
R_7	Radius of the ring in the CVT	$[m]$
R_c	Ratio between the ring and roller/cones contact point radius in the CVT	$[m]$
r_m	Lever of muscle m	$[m]$
R_s	Ratio between the sun and sun/cones contact point radius in the CVT	$[m]$
$R_{5'}$	Curvature radius of the edge of the dome-shaped sun in the CVT	$[m]$
$R_{6',max}$	Maximum cones radius in the CVT	$[m]$
$R_{6',min}$	Minimum cones radius in the CVT	$[m]$
$R_{6'}$	Radius of the roller/cones contact point in the CVT	$[m]$
$R_{7'}$	Curvature radius of the roller in the CVT	$[m]$
$R_{c,max}$	Maximum value of ratio R_c	$[m]$
$R_{c,min}$	Minimum value of ratio R_c	$[m]$
R_{ij}	Curvature radius of the element i in plane j in the Hertz theory	$[Pa]$
S_m	Stimulation of muscle m	$[-]$
$S_{0,m}$	Pre-stimulation of muscle m	$[-]$
t	Time between the max and min torque	$[s]$

t	Time of simulation	$[s]$
$T1$	Forward position of the trunk's centre of mass w.r.t. the inertial frame	$[m]$
$T3$	Vertical position of the trunk's centre of mass w.r.t. the inertial frame	$[m]$
T_1	Torque on the sun in the planetary gears	$[N\,m]$
T_3	Torque on the ring the planetary gears	$[N\,m]$
T_4	Torque on the planets carrier in the planetary gears	$[N\,m]$
T_5	Torque on the sun in the CVT	$[N\,m]$
T_6	Torque on each cones in the CVT	$[N\,m]$
T_8	Torque on the planet carrier in the CVT	$[N\,m]$
T_c	Torque on the planets carrier in the planetary gears	$[N\,m]$
t_f	Total simulation time	$[s]$
T_s	Torque on the sun in the planetary gears	$[N\,m]$
$T_{8'}$	Resulting torque on the planets carrier in the IVT	$[N\,m]$
$T_{IVT,max}$	Maximum torque provided by the IVT	$[N\,m]$
$T_{IVT,min}$	Minimum torque provided by the IVT	$[N\,m]$
T_{max}	Maximum torque required at the joint	$[N\,m]$
T_{min}	Minimum torque required at the joint	$[N\,m]$
T_{screw}	Torque required at the screw to slide the ring in the CVT	$[N\,m]$
T_{spring}	Mean torque required at the output of the spiral spring	$[N\,m]$
$t_{threshold}$	Time threshold to unlock the next fitness stage	$[s]$
V	Penetration volume of the ground contact model	$[m^3]$
v	Norm of the relative tangential speed between the foot and the ground at the contact point	$[m\,s^{-1}]$
W	Weight to slide the ring in the CVT	$[N]$
x	Axial position of the ring w.r.t. the top of the cone in the CVT	$[m]$

List of Figures

List of Tables

Introduction

Nowadays, plenty of bipedal robots have already been developed. The purposes of their development are highly diversified, as well as their field of activity. Some are conceived for entertainment, by playing football for example. Others are developed to help humans in their daily lives or in dangerous tasks such as extinguishing a fire. Still others are developed to execute complex tasks like removing debris or opening a valve. Robots can also be built for military purposes, etc. Today, research is still carried out, improving the existing bipedal robots or developing new ones.

Due to their variety, bipedal robots can be classified according to several criteria. Some robots are passive since they use no power source to move while others are active. There also exists 2D bipedal robots that are restricted to move in one plane, namely the sagittal plane, while those that are not limited to one plane are called 3D bipedal robots.

The objective of this master thesis is to simulate, control and design a new 2D humanoid walker composed of five bodies (two calves, two thighs and one trunk but no feet) and four compliant joints (two hips and two knees). Its main particularity is that its four joints will all be actuated by a single power motor through the use of differentials and transmissions. More precisely, Infinitely Variable Transmissions (IVTs) developed at the UCL by Christophe Everarts will be used and allow to adapt the output torque according to the requirements.

To summarise, the purpose of this master thesis is thus to validate the principle of multiple actuation with IVTs in a 2D bipedal robot with four degrees of actuation.

This master thesis will be divided into six chapters. First, as a contextual setting, a state of the art of existing 2D and 3D bipedal robots is presented. Then, the IVT is described and its use in this application is justified by explaining the biomechanics of human locomotion. After that, the mechanical design of the robot is covered, presenting all steps leading to the final morphology of the robot meeting the specifications. In parallel to the mechanical design of the robot, a simulation was realised to determine the quantities required for the mechanical dimensioning of the main part of the robot, such as the torque profile in each joint, the power profile during the walk, the evolution of the position of the centre of mass, etc. To achieve this simulation, a high level control was implemented based on a neuromuscular model. This latter is then described, followed by the results of the simulation. These results are presented and then compared to human walking data as well as to the data of another 2D bipedal robot having feet. After, the last chapter addresses the mechanical dimensioning of the powertrain of the robot, defined as the transmission chain from the power motor to the transmission to the joints. Finally, conclusions are drawn and prospects for improvement are given.

Chapter 1

State of the art of humanoid robots

Today, many 2D and 3D bipedal robots have already been developed. All the bipedal robots described here below are active and are differentiated by their development's purpose, number of degrees of freedom, dimensions, etc.

This chapter will first deeply present some 2D bipedal robots that were useful for the design of the robot of this master thesis: RABBIT, ERNIE, DURUS-2D, MABEL and ATRIAS. Each of those has specific features that are interesting to deepen to potentially include them in the design if it turns out to be useful. Then, this chapter will briefly present some 3D bipedal robots in order to show the additional complexity of their design and control but also to show the numerous interactions they can have with the environment. These robots are ASIMO, ATLAS and WALK-MAN. Another 3D bipedal robot, COMAN, will also be described since its simulation results will be used in the last chapter to make a comparison with the robot of this master thesis. Finally, a less known 3D bipedal robot is presented, called Kengoro, as it has a special feature compared to other existing robots.

1.1 2D bipedal robots

The 2D bipedal robots being described in this section were mainly designed for research in control. Some characteristics of these bipedal robots are given in table 1.1.

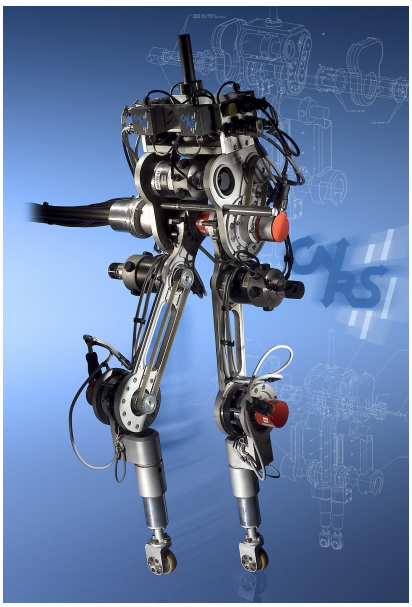

Figure 1.1: RABBIT [1].

First of all, RABBIT, which is depicted in figure 1.1, is a test bed robot that was created by members of seven French laboratories but also from Michigan and Ohio universities [1, 2]. The French Institute for Research in Computer Science and Automation also took part in this project. This latter started in 1997 and ended in 2004. Designed to walk and run, RABBIT was developed to compare powered bipedal robot locomotion to passive locomotion as well as to understand the impact of the mechanical and control design choices on its locomotion [2]. This bipedal robot has five or seven degrees of freedom, depending on the phase of motion, and 4 degrees of actuation.

RABBIT only moves around a circle and is maintained in its sagittal plane by means of a two metres long boom connected to a central column. Moreover, it has no feet in order to demonstrate that a stable locomotion is achievable with no ankles, allowing thus to reduce the

total weight of the robot. As feet, it has wheels perpendicular to its sagittal plane so that its motion can be assumed to be that of a planar robot. [2]

Concerning the control of this bipedal robot, several dynamical models are necessary in order to describe the evolution of the system [1]. Each of these models corresponds to either a support phase, i.e. when there is one or more legs in contact with the ground, or a flight phase, i.e. when there is no ground contact. Between each phase, there is an impact of one or more legs with the ground, except before a flight phase. This impact requires a supplementary model that determines the energy dissipated in the impact and the initial conditions of the model of the following phase.

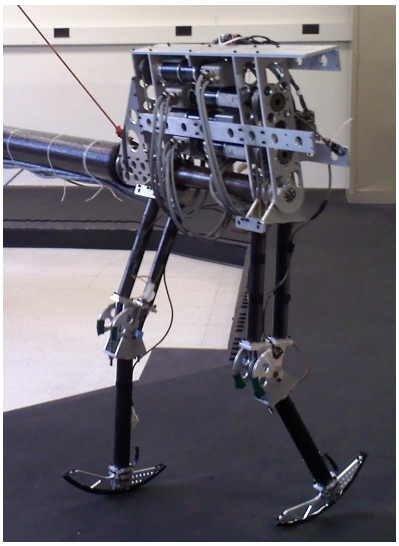

Figure 1.2: ERNIE [3].

Next, there is ERNIE, a test bed bipedal robot developed by the Ohio State University's Locomotion and Biomechanics Lab in 2005 [2]. It is represented in figure 1.2 and was created with the aim of developing novel control strategies for bipedal walking and running. This robot has seven degrees of freedom and is controlled by a technique using direct nonlinear optimization to generate dynamically feasible system trajectories [3]. ERNIE can either walk around a circle or on a treadmill, according to the available space [2].

Its morphology is similar to that of RABBIT: a torso and two legs with knees but no feet. However, some interesting features have been added compared to RABBIT [2]. First, its legs are modular allowing to ease the study of robot asymmetry, walking with feet, etc. Moreover, its boom and legs are mainly made of carbon fibre, reducing the weight and thus the torques required at the joints. After, all actuators are located in its torso resulting in lighter legs and thus smaller motors but also in more complicated transmissions. Besides, in order to reduce the peak power requirements of ERNIE, parallel compliance can be added at its knees. Finally, by using gear reducers with staged planetary gear sets instead of harmonic drives, ERNIE's joints have less friction than those of RABBIT.

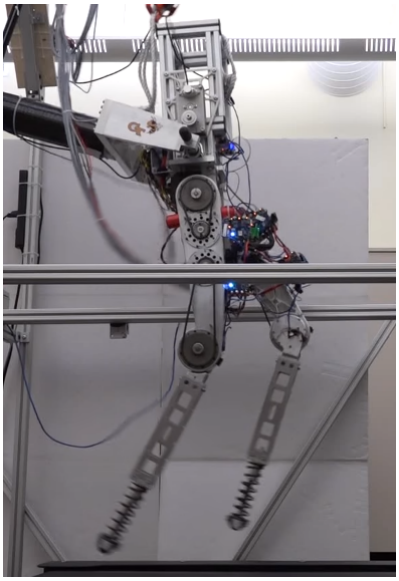

Figure 1.3: DURUS-2D [4].

A third robot, DURUS-2D, represented in figure 1.3, is a bipedal robot created by the Advanced Mechanical Bipedal Experimental Robotics (AMBER) Lab [5]. This laboratory, which was previously situated in the Georgia Institute of Technology, is currently located at the California Institute of Technology (Caltech) and is notably dedicated to experimental research in bipedal robotics and prosthetic design [4]. This project is still under development: the most recent versions of this robot evolved to 3D [5].

DURUS-2D has the same morphology than the two robots presented before and has seven degrees of freedom. Such as ERNIE, it can either walk in a circle or on a treadmill [5].

However, what differentiates it from the two previous bipedal robots is its ability to run on a treadmill and to reach thirteen centimetres off the ground while jogging [6]. Moreover, it has a human-like gait.

In order to achieve bipedal robotic walking, human walking data is used, as well as ideal torque controllers via the ideal model resolved motion method (IM-RMM), which integrates forward the actual state of the hardware to determine the desired positions and velocities commands [7]. Given its human-inspired control, DURUS-2D contributes thus to the development of more human-like robotic prosthesis [6].

Figure 1.4: MABEL [8].

After, MABEL is a bipedal robot developed by the Oregon State University Dynamic Robotics Laboratory in 2009 [8]. It is depicted in figure 1.4 and was designed to be both a robust walker and a fast runner. MABEL is able to run, walk, jump and it generally behaves in a highly dynamic manner, maximizing its energy efficiency, speed and stability [8, 9]. Its control is based on the hybrid zero dynamics (HZD) method that has been modified to add an actuation during the stance phase of running [10]. Additional outer-loops event-based were also added in order to increase the stability and the robustness. Being capable of sprinting at a speed up to 10.9 [km/h], it is the world's fastest "kneed" bipedal robot [11].

MABEL has the same morphology as RABBIT, ERNIE and DURUS but includes large fibreglass springs used to store the energy of a running gait [9].

The main difference with the previously presented bipedal robots is that this robot is based on the Electric Cable Differential (ECD) Leg [9]. The name "ECD Leg" comes from the method of actuation and power transmission. Indeed, electric motors are used to actuate the joints instead of pneumatic or hydraulic actuators because they are more easily and more precisely controlled. Then, these electric motors are connected to the robot's joints thanks to steel cables wrapped around aluminium pulleys. Besides, several mechanical differentials are used to link the electric motors, the springs and the joints, according to the required ratios between these parts.

Figure 1.5: ATRIAS 2.1 [12].

Finally, ATRIAS is a series of robots implemented in order to develop agile and efficient robotic locomotion but also to understand ground-running bird locomotion strategies [13, 14]. They were developed by the Oregon State University Dynamic Robotics Laboratory and there are currently three prototypes based on the ATRIAS concept [8]. They were designed based on the spring-mass model, that allows them to walk and run efficiently, on even or uneven ground, and in a similar way than humans and other animals [13].

The realization considered here is the last one, ATRIAS 2.1, which is a human-scale bipedal robot. It has been created in 2012 and is represented in figure 1.5.

What differentiates ATRIAS 2.1 from other common bipedal robots is its leg design, which is central to its agility and efficiency [13]. Indeed, the four bar mechanism is very lightweight, allowing to soften each footfall, reducing the shocks felt

by the body.

Table 1.1: Characteristics of RABBIT, ERNIE, DURUS-2D, MABEL and ATRIAS.

RABBIT [1, 2]		
Height of its hip	0.8	[m]
Total height	1.425	[m]
Total mass	36.0	[kg]
ERNIE [2]		
Height of its hip	0.72	[m]
Total height	1.0	[m]
Total mass	18.6	[kg]
DURUS-2D [7]		
Height of its hip	0.89	[m]
Height of the centre of mass of its torso	1.05	[m]
Total mass	31.5	[kg]
MABEL [10]		
Length of its legs	1.0	[m]
Total mass	65.0	[kg]
ATRIAS [15]		
Total height	1.71	[m]
Total mass	62.0	[kg]

1.2 3D bipedal robots

As their movements are not limited to the sagittal plane, 3D bipedal robots can perform far more actions than 2D ones. However, this also add some complexity in their design and control because of their additional degrees of freedom. The robots presented here were chosen due to their notoriety and because together they are sufficient to clearly represent these two points.

First, one of the famous 3D bipedal robot is ASIMO [16], which is represented in figure 1.6a. This humanoid robot results from years of humanoid robotics research (it secretly started in 1986) by Honda engineers whose primary objective was to create a walking robot. They first focused on human walking then on walk stabilization and stair climbing before adding a head, a trunk and two arms. After numerous improvements, they finally built ASIMO. This latter has 34 degrees of freedom actuated by servo motors and has a rechargeable battery giving an autonomy of one hour. It can perform a lot of actions (see figures 1.6b to 1.6e) such as walking on even and uneven ground, running, climbing stairs, turning and grasping objects. He also can react to voice commands and recognize a face. In the future, it could be used to help humans like elderly or disabled persons in their daily lives but it could also be of help in dangerous tasks like extinguishing a fire.

(a) General view.

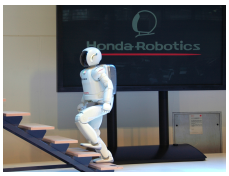

(b) Climb stairs.

(c) Carry a tray.

(d) Open a bottle.

(e) Play football.

Figure 1.6: ASIMO and some of the actions it can perform [17].

Then, ATLAS [18] is a humanoid robot created by Boston Dynamics in 2013 and depicted in figure 1.7a. It has 28 degrees of freedom hydraulically actuated and powered from an off-board electric power supply. Moreover, it is controlled through inverse kinematics and inverse dynamics [19].

This humanoid robot took part in the DARPA Robotics Challenge (DRC) which was a prize competition funded by the Defense Advanced Research Projects Agency (DARPA) [20]. This latter is an agency of the U.S. Department of Defense responsible for the development of emerging technologies for military use [21]. The goal of the DRC is to develop human-supervised ground robots capable of executing complex tasks in dangerous, degraded, human-engineered environments [22]. The robots that participated in this competition were asked to use standard tools and equipment commonly available in human environments, ranging from hand tools to vehicles [22]. The tasks that have to be realised are the following: drive a vehicle, walk on rubble, remove debris, open a door, climb a ladder, use tools, connect a fire hose and turn on or close a valve [20].

ATLAS has therefore been designed to negotiate outdoor, rough terrain (1.7b) and can use its arms to interact with the environment (1.7c), to carry loads (1.7d) but also to climb (1.7e). Its hands are articulated and equipped with sensors allowing it to use tools designed for humans, as requested by the DRC's rules.

(a) General view.

(b) Walk on uneven ground.

(c) Open/close a valve.

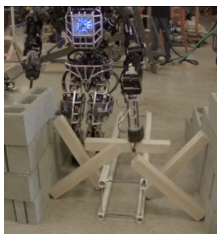

(d) Remove debris.

(e) Climb a ladder.

Figure 1.7: ATLAS and some of the actions it can perform [18, 19, 23, 24].

In addition to ATLAS, a lot of other robots took part in the DRC, of which WALK-MAN, developed by the Italian Institute of Technology (IIT) in 2013 [25, 26]. This humanoid robot is depicted in figure 1.8. The aim of the WALK-MAN project was to developed a completely original and new body design. Moreover, its degrees of freedom are actuated by electric motors and their control can be realised in different ways: position, torque or impedance control. Some of the actions WALK-MAN can perform are depicted in figures 1.8b to 1.8d.

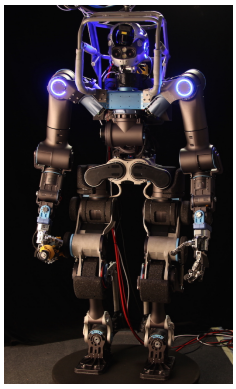

(a) General view.

(b) Drive a car.

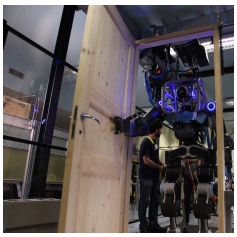

(c) Open a door.

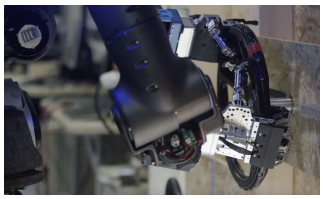

(d) Open/close a valve.

Figure 1.8: WALK-MAN and some of the actions it can perform [25, 27].

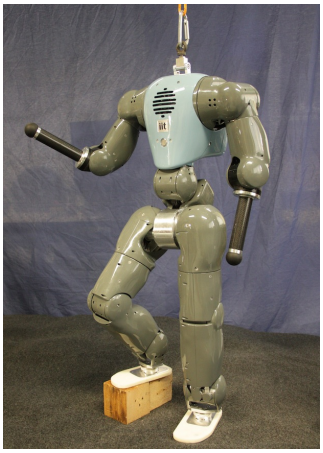

Figure 1.9: COMAN [28].

Next, COMAN is a humanoid robot designed by the Advanced Robotics department of the Italian Institute of Technology (IIT) located in Genoa, in Italy [29]. It is represented in figure 1.9. Its name stands for "COmpliant huMANoid", as the aim of its development was to build a robot with passive compliant joints [30]. The compliance allows the robot to be more robust to environment perturbations, to have safer human-robot interactions, to reduce the energy consumption and to perform more dynamic motions [29, 30].

This robot modelled on a four-year-old child, measures 95 [cm] and weighs 31 [kg] [28, 30]. It has 25 degrees of freedom and a combination of stiff and compliant joints [28].

Finally, there is Kengoro which is a musculoskeletal humanoid developed by researchers at the University of Tokyo's Jouhou System Kougaku (JSK) Laboratory in 2016 [31]. It is depicted in figure 1.10.

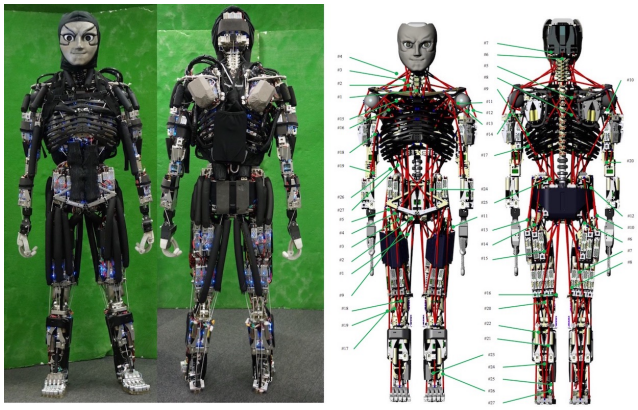

Figure 1.10: Kengoro [32].

Its main feature differentiating it from the other robots is that it sweats [32]. Indeed, in order to solve the heat-generating problem due to the motors, the Japanese researchers needed to add a cooling system. However, due to the lack of space, they could not use an active cooling system requiring fans, heat sinks or radiators. They thus developed a passive technique using the robot's skeletal structure as a coolant-delivery system: they *allow the water to seep out through the frame around the motors to cool them by evaporation* [32].

Besides, this robot has 114 degrees of freedom and 106 motors. It also has a musculoskeletal structure based on anatomy: it is composed of bones, motors and muscles. Moreover, it has a flexible spine which has a S-curve structure and which is made of three different kinds of vertebrae: the cervical, the thoracic and the lumber vertebrae. It also has a human mimetic foot structure: each feet has 19 degrees of freedom. [31]

Chapter 2

Humanoid walker based on IVTs

This second chapter presents the purpose of this master thesis: the design of a new bipedal robot using IVTs. At first, it introduces the biomechanics of humanoid locomotion and the interest of compliant elements in humanoid robots or prostheses. It then briefly presents different compliant elements focusing on the Infinite Variable Transmission. Finally, it introduces the humanoid robot designed for this master thesis.

2.1 Biomechanics of human locomotion

Humanoid robots tend to reproduce the dynamical behaviour of human joints, and therefore similar power profiles, in order to display human-like gaits. Before designing a bipedal robot, it is hence necessary to understand the biomechanics of human locomotion. This section presents the torques and powers profiles observed in human gait.

This master thesis relies on torques and powers profiles described in a study by David A. Winter [33]. This resource is widely used as reference, not only in robotics research but also in other fields like bioengineering, kinesiology, etc. The methodology allowing to derive these profiles will not be presented here.
The figures 2.1 and 2.2 respectively present the torques and powers profiles in human lower limbs during one stride at a normal walking speed. The results are normalised with respect to the mass of the individual. The graphs are represented in function of the percentage of the stride. The stance phase of a leg, i.e. when the foot is on ground, lasts approximatively the first 60% of the stride while the swing phase corresponds to the 40% remaining.

The torques profiles in the hip and knee pass several time by zero, showing that the joint changes from flexion to extension and vice-versa. The ankle presents a higher torque during the stance phase than the two others joints. This indicates that the ankle is responsible for the majority of the propulsion of the body during the stride. This information is also present in the power profile. During the swing phase, the ankle has however nearly no torque, since the foot is not in contact with the ground.

The power profiles of the hip and knee joints alternate several times between positive and negative values during the stance phase. As the energy is the integral of the power over time, this translates thus into an alternation between production and dissipation of energy. During the swing phase, the hip has a positive energy meaning that it requires energy while the knee has a negative energy resulting in a tendency to dissipate energy. Concerning the ankle, the peak at the end of the stance phase shows again its contribution to the propulsion. But before that, it dissipates energy. The ankle still has no contribution during the swing phase.

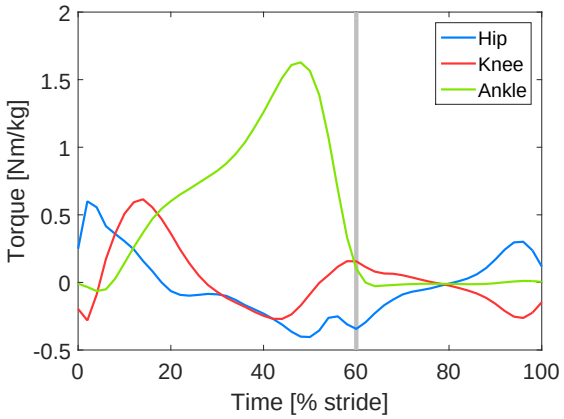

Figure 2.1: Torques profiles in human leg's joints during one stride at a normal walking speed [33].

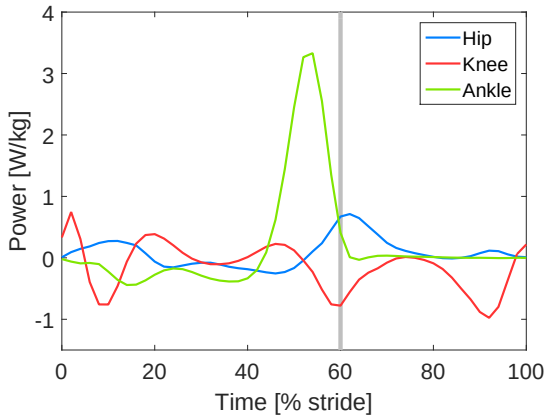

Figure 2.2: Powers profiles in human leg's joints during one stride at a normal walking speed [33].

Over a gait cycle, more power is consumed than dissipated in the hip and in the ankle, making the net energy positive. In the knee, this net energy is negative as more power is dissipated than consumed. In total over one cycle, the energy of one leg is positive and thus required.

In order to take advantage of the dissipation of energy in the joints, researchers in robotics use compliant elements with the robot's actuators. These elements have the ability to store and release mechanical energy. But as they are passive, they cannot produce energy. There still needs then a source of power to compensate the net positive energy. Therefore, the introduction of compliant elements allows to filter the power profile asked to the actuators.

2.2 Compliant transmissions and Infinitely Variable Transmission

The most used concept of compliant element in robotics is the Series Elastic Actuator (SEA) [34]. A SEA is composed of a serial connection of a standard actuator and a compliant element, such as a spring. Adding a spring in series with the actuator allows to filter the power profile, decreasing the power peak provided by the actuator. The major drawback of this technology is that the stiffness of the compliant element is optimised only for one specific type of gait and rhythm.

A Variable Stiffness Actuator (VSA) [35] represents an improvement of the SEA, in which the stiffness of the compliant element can be adapted by means of a second smaller motor in order to adapt to different gaits and rhythms. This is performed either by implementing in advance different gaits and detecting with an appropriate controller which one to use or by modifying the stiffness within a gait cycle. In the second solution, the main motor provides the mean positive power required while the smaller motor is controlled to adapt the stiffness to correspond to the desired torque.

Even with the VSA approach, the energy balance is still positive. It is then important to use a mechanism consuming as less energy as possible to vary the stiffness of the compliant element in order to minimise the total energy consumption. This point is ensured with an Infinitely Variable Transmission (IVT).

An IVT is a transmission that can continuously change its gear ratio from negative to positive values. The transmission ratio of the IVT is controlled by a smaller motor, consuming nearly no energy. The compliant behaviour with a variable stiffness of the IVT is guaranteed by connecting the motor in series with a spring and then the IVT. The stiffness of the spring does not change but the mechanism shows a

variable stiffness thanks to the IVT. This allows a storage of a constant amount of energy in the spring.

The Infinitely Variable Transmission will be presented in more detail below and corresponds to the one that has been developed by Christophe Everarts from UCL [36]. As the IVT is the extension of an other element, the Continuously Variable Transmission (CVT), this latter will be presented before the IVT. However, in order to explain the working principle of the CVT and the IVT, a first reminder about planetary gears train is appropriate.

2.2.1 Planetary gears transmission

A planetary gears (PG), or epicyclic gear train, consists of a mechanical system where n gears, called planets (2, 2' in figure 2.3), revolve around a central gear, called sun (1), and inside an outer gear, called ring (3). It is possible to have different planets' diameter for the sun/planet contact (1-2) than for the ring/planet contact (2'-3). The planets are mounted on a carrier (4). The carrier, the sun and the ring have the same centre of rotation. The figure 2.3 shows the kinematic diagram of a planetary gears train.

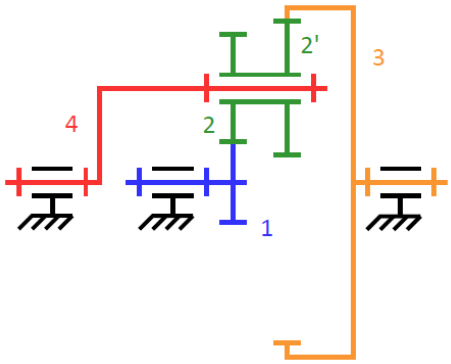

Figure 2.3: Planetary gears train kinematic diagram [36]. The sun (1) is represented in blue, the planets (2, 2') are in green, the ring (3) is in orange and the planet carrier (4) is in red.

The planetary gears train is characterised by its train value [37]:

$$\tau_{PG} = \frac{\omega_1 - \omega_4}{\omega_3 - \omega_4} = -\frac{N_3}{N_1}\frac{N_2}{N_{2'}}$$

where ω_i is the angular speed of the element i and N_i the number of teeth of the gear i. This equation also works by replacing the number of teeth N_i by the pitch diameter (or radius) of the gear i.

The construction of this mechanism has to respect some constraints [37] [38]. Firstly, for two gears to mesh, their module m (defined as the pitch diameter divided by the number of teeth) have to be same. Secondly, in order to be coaxial, the numbers of teeth, and hence their diameters, have to comply with the equation $N_3 - N_{2'} = N_2 + N_1$. Finally, in order for the n planets to be equally distributed around the sun, the number of teeth has to respect the equation $(N_1 + N_3)/n = i$, where i is an integer.

The planetary gears is usually used with one of its gears held fixed. The transmission ratio of the system is then obtain by removing the rotation speed of this gear from the train value.

2.2.2 Continuously variable transmission

The CVT concept proposed by Christophe Everarts [36] can be seen as a PG whose planets are tilted and cone-shaped. The variation of the transmission ratio is performed by moving the contact point of the ring

on the cone surface. This contact point is the key element of this new concept of CVT.

The kinematic diagram of this CVT is given in figure 2.4. The planets are conical with their shafts (8) tilted by an angle α (here by 45°). The outer surface of the cones (6') are tangent to rollers forming a continuous circle of radius R_7 concentric with the sun (5) and ring (7) axes of rotation. A scheme of the ring morphology is represented in the figure 2.5. In this way, the ring can slide along its axis, while keeping contact with the cones without friction since the roller are rolling on the planets. This translation movement makes the planet pitch radius $R_{6'}$ vary and therefore changes the transmission ratio between the ring and the cones. The transmission of torque between the ring and the planets is ensured by friction. Indeed, since the planets' radius varies continuously, the motion cannot be transmitted via gears. Because the cones' axis is tilted by an angle α with respect to the sun's axis, the dome-shaped sun is pushed on the base of the cones and the transmission of motion is achieved by friction. The contact point's radius from the sun axis is noted R_5 and is noted R_6 from the planets' axis.

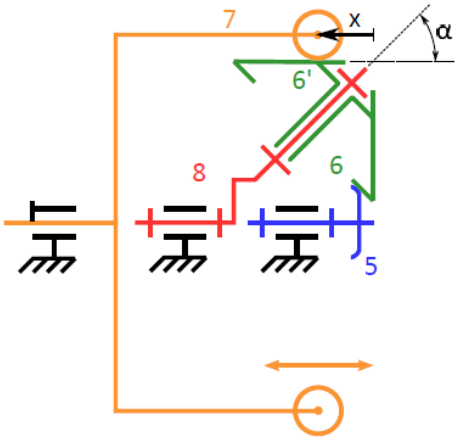

Figure 2.4: CVT kinematic diagram [36]. The sun (1) is represented in blue, the cone (6, 6') in green, the roller (7) in orange, the planet carrier (8) in red.

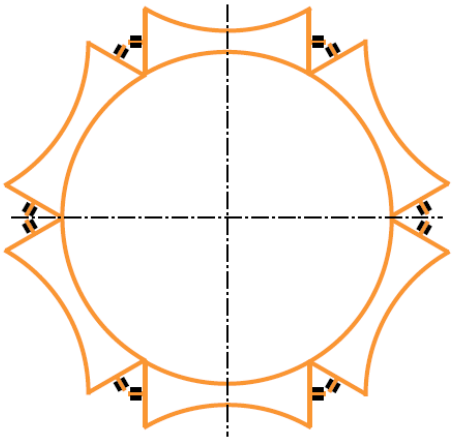

Figure 2.5: CVT ring scheme [36]. The ring is composed of several rollers forming a circle around the centre of rotation in order to have a single contact point with each cone.

The kinematic equation of the CVT is similar to that of the PG:

$$\tau_{CVT} = \frac{\omega_5 - \omega_8}{\omega_7 - \omega_8} = -\frac{R_7}{R_5}\frac{R_6}{R_{6'}}$$

but with $R_{6'}$ depending on the ring varying axial position x and the cone tilt angle α through: $R_{6'} = x \sin\alpha$. The axial position is defined as $x = 0$ when the contact point is situated at the top of the cone.

The ring of the CVT is considered blocked in rotation, which is equivalent to imposing the kinematic constraint $\omega_7 = 0$. Therefore, considering the planet carrier (8) as output and the sun (5) as input, the transmission ratio of the CVT can be written as:

$$\tau_{CVT} = \frac{\omega_5}{\omega_8} = 1 + \frac{R_7\,R_6}{R_5\,R_{6'}} = 1 + \frac{R_7\,R_6}{R_5}\frac{1}{x\,\sin\alpha} = \frac{T_8}{T_5}$$

The CVT transmission ratio is thus always positive. The equation above is theoretically valid in the range $[0\,;\,\infty]$ but these boundaries are not practically reachable. It is indeed impossible to have a cone radius equal to 0, corresponding to the infinite boundary. In the same way, the cone radius cannot be infinite and therefore the CVT cannot reach a null transmission ratio. This equation also corresponds to the torque

transmission in the other way: from (8) to (5). It is in this form that it will be used here since the purpose is to control the transmitted torque, as it will be explained later.

The number of cones and rollers is of great importance to the performance of the design. Indeed, they impact the distribution of the forces and a bad design would induce high frictions. In the paper of Chritophe Everarts, the CVT possesses four cones and six rollers. If the number of cones increases, so does the number of contact points, and thus the transmissible torque, but the space available for each cone would decrease, hence reducing the range of variation of the CVT. Therefore, this amount of cones is ideal for the force distribution while using a maximum of the available volume. Regarding the number of rollers, it has to be strictly higher than the number of cones. The reason is to avoid the case where one roller is in contact with two different cones, with different radii. This would induce high friction forces during the variation of the ratio. To maximise the force distribution, a maximum of two contact points between the cones and the extremity of the rollers is allowed. With six rollers, the two other contact points are situated at the middle of the other rollers. Finally the number of rollers should not be a multiple of the number of cones in order to reduce the vibrations.

In order to convert the CVT into an IVT, the transmission ratio has to be shifted to reach negative values too. This is done with an additional PG.

2.2.3 Infinitely variable transmission

The studied IVT model is the combination of the CVT presented above and a PG. The scheme 2.6 represents the connection between these two elements, forming the IVT. The sun of the CVT (5) is on the same shaft as the sun of the PG (1), the output of the IVT (8), corresponding to the planet carrier of the CVT, is connected to the planet carrier of the planetary gears (4) and the input of the IVT is the ring of the planetary gears (3).

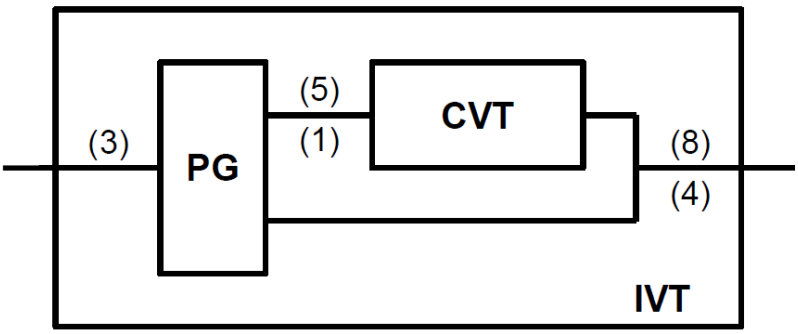

Figure 2.6: IVT scheme representing the connection between the CVT and the PG.

The kinematic diagram of the IVT is given in the figure 2.7. This is the combination of the kinematic drawing of the CVT and the PG presented before and connected as cited just above.

Therefore, the angular velocities of the planet carrier of the CVT and of the planet carrier of the PG are equal:

$$\omega_8 = \omega_4$$

The same goes for the angular velocities of the sun of the CVT and of the sun of the PG:

$$\omega_5 = \omega_1$$

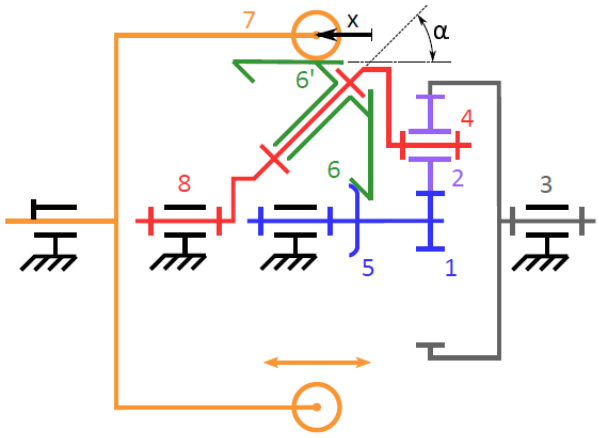

Figure 2.7: IVT kinematic diagram [36]. The different elements keep their numbering from the figures 2.3 and 2.4.

Since the ring of the PG and the planet carrier of the CVT are respectively considered as the input and output of the IVT, it gives:

$$\tau_{IVT} = \frac{\omega_3}{\omega_8} = \frac{T_8}{T_3}$$

With the equalisation of the different angular velocities, the train value of the PG is written as:

$$\tau_{PG} = \frac{\omega_5 - \omega_8}{\omega_3 - \omega_8} = -\frac{R_3}{R_1}$$

since the planets have the same radius for the ring and the sun. This equation can be organised to express the transmission ratio of the IVT as a function of the transmission ratio of the CVT and the PG.

$$\begin{aligned}
\tau_{PG} &= \frac{\omega_5 - \omega_8}{\omega_3 - \omega_8} \\
\tau_{PG}\,(\omega_3 - \omega_8) &= (\omega_5 - \omega_8) \\
\tau_{PG}\,\omega_8 \left(\frac{\omega_3}{\omega_8} - 1\right) &= \omega_8 \left(\frac{\omega_5}{\omega_8} - 1\right) \\
\tau_{PG}\,(\tau_{IVT} - 1) &= (\tau_{CVT} - 1) \\
\tau_{IVT} &= \frac{\tau_{CVT} - 1}{\tau_{PG}} + 1 \\
\tau_{IVT} &= 1 - \frac{R_1\,R_6\,R_7}{R_3\,R_5} \frac{1}{x\,\sin\alpha}
\end{aligned}$$

With x comprised between 0 and 1, the IVT transmission ration can vary from $-\infty$ to 1, passing thus by 0. Even though it is impossible to reach a value $x = 0$ as explained before, it is still possible to dimension the CVT and PG in order to have the IVT ratio increasing from negative to positive values (see chapter 6).

This equation is the relation between the angular velocities from the CVT's planet carrier (8) to the PG's ring (3). It also corresponds to the torque ratio of the reverse, from the PG's ring (3) to the CVT's planet carrier (8). It will be used in this last way.

2.3 Introduction of a humanoid walker based on IVTs

The use of the IVT presented above as a pseudo-VSA was already applied for example in a lower limb prosthesis (for the knee and ankle) [39]. The IVTs are there used in series with the motor, a torsional

spring and a mechanical differential to control the torque of the two joints. This introduces the concept of a multiple actuation from a single motor to actuate different joints. The idea is to use the power dissipated by the two joints to recharge a unique spring for the all mechanism.

This section constitutes the first original contribution of this master thesis.

The purpose of this master thesis is to introduce the design of a new humanoid walker composed of five bodies (two calves, two thighs and one trunk but no feet) and four compliant joints (two hips and two knees). This bipedal robot implements the principle of multiple actuation using IVTs.

The general morphology of the powertrain of this robot is given in the figure 2.8. Usually applied to cars, the definition of powertrain refers to the whole mechanism of transmission between the motor and the ground but this term is used here to denote the transmission chain from the power motor to the output of the planetary gears.

This powertrain describes as follows. The power motor feeds a potential energy storage which in turn discharges in the rest of the mechanism. The first differential separates the left leg to the right leg in order to keep the design as symmetrical as possible. However, the two legs will have a power profile shifted by half a period and this configuration should allow a maximum exchange of energy between the two halves of the robot.

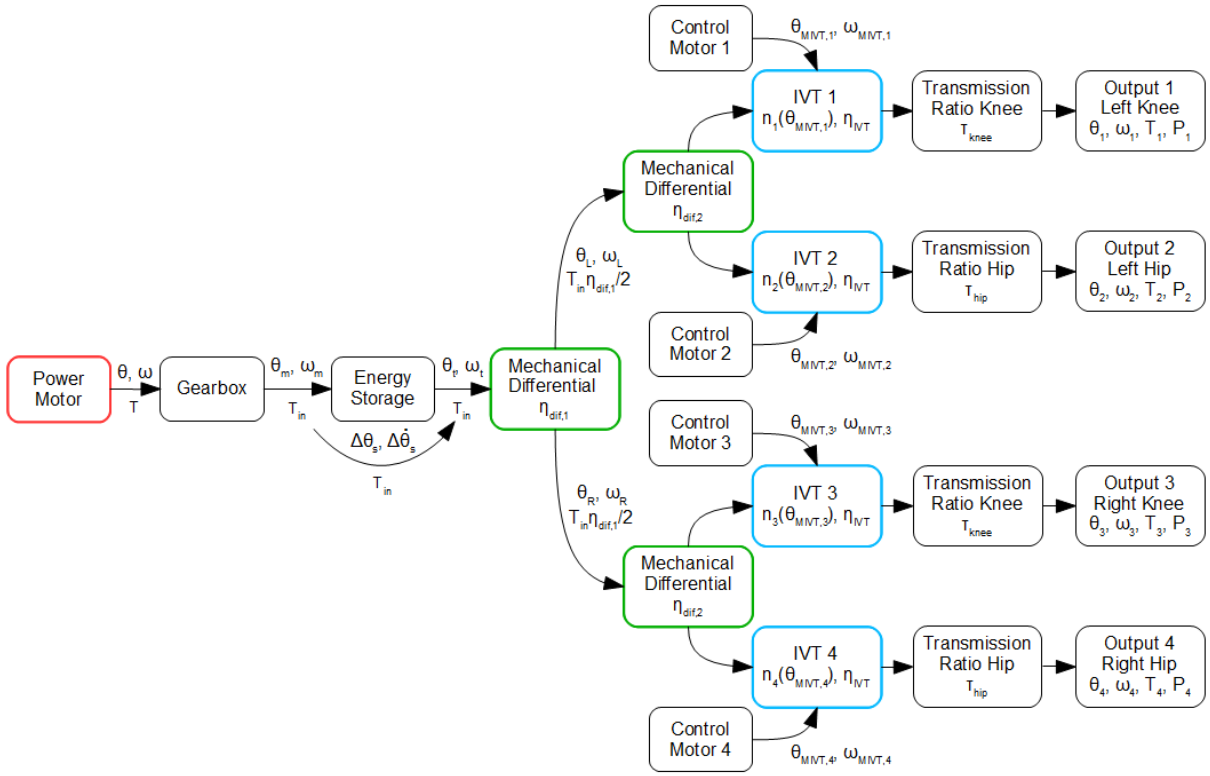

Figure 2.8: Black boxes scheme of the powertrain

The complete mechanical design of the robot is explained in the next chapter 3.

Chapter 3

Mechanical design of the humanoid walker

This chapter presents the steps followed leading to the mechanical design of the robot of this master thesis. First of all, the specifications of the robot are established according to the initial prescriptions of the thesis. Then, a function analysis is performed in order to establish the functions required in the design. From this analysis, morphological tables regrouping many different solutions for each function are written. Finally, these solutions are assessed according to several predetermined criteria, allowing thus to reach the final design.

Even though the emphasis is put on the mechanical design, the electrical design is also considered through the choice of the appropriate sensors.

3.1 Summary of the specifications

As already explained in the introduction, the purpose of this master thesis is to simulate, control and design a humanoid walker and more specifically to validate the principle of multiple actuation by IVTs in a 2D bipedal robot with four degrees of actuation.

In other words, the designed robot has to be a biped composed of five bodies (two calves, two thighs and one trunk), four compliant joints (two hips and two knees) but no ankle nor feet. Its four joints will all be actuated by a single power motor through the use of differentials and IVTs[1]. Besides, this humanoid walker will be restricted to move in the sagittal plane solely and will be able to walk straight or in a circle. Finally, it has to adopt a humanoid walking gait. Since the IVTs regulate their output torque, as explained in the previous chapter, the controller has to act by controling the torque of the joints. The chosen model for the implementation of the controller is the neuromuscular model of Geyer [40] as it fulfils these requirements. This model will be explained in the next chapter.

Upon request of the supervisor, some constraints are added to the features stated above. All the powertrain will have to be contained in the trunk, except the transmission to the knee's joint. Moreover, the humanoid walker will have to be about half the size of a human. Furthermore, it will be powered from an off-board electric power supply and will thus have no battery.

The specifications described above are given in Appendix A (page 87). The latter will be taken into account at each step of the design process.

[1] The IVTs have been described in chapter 2.2 (page 10).

3.2 Function analysis and work flow of the robot

The function analysis consists in establishing the flow of the robot from its resting position to its operation. This flow is represented in figure 3.1.

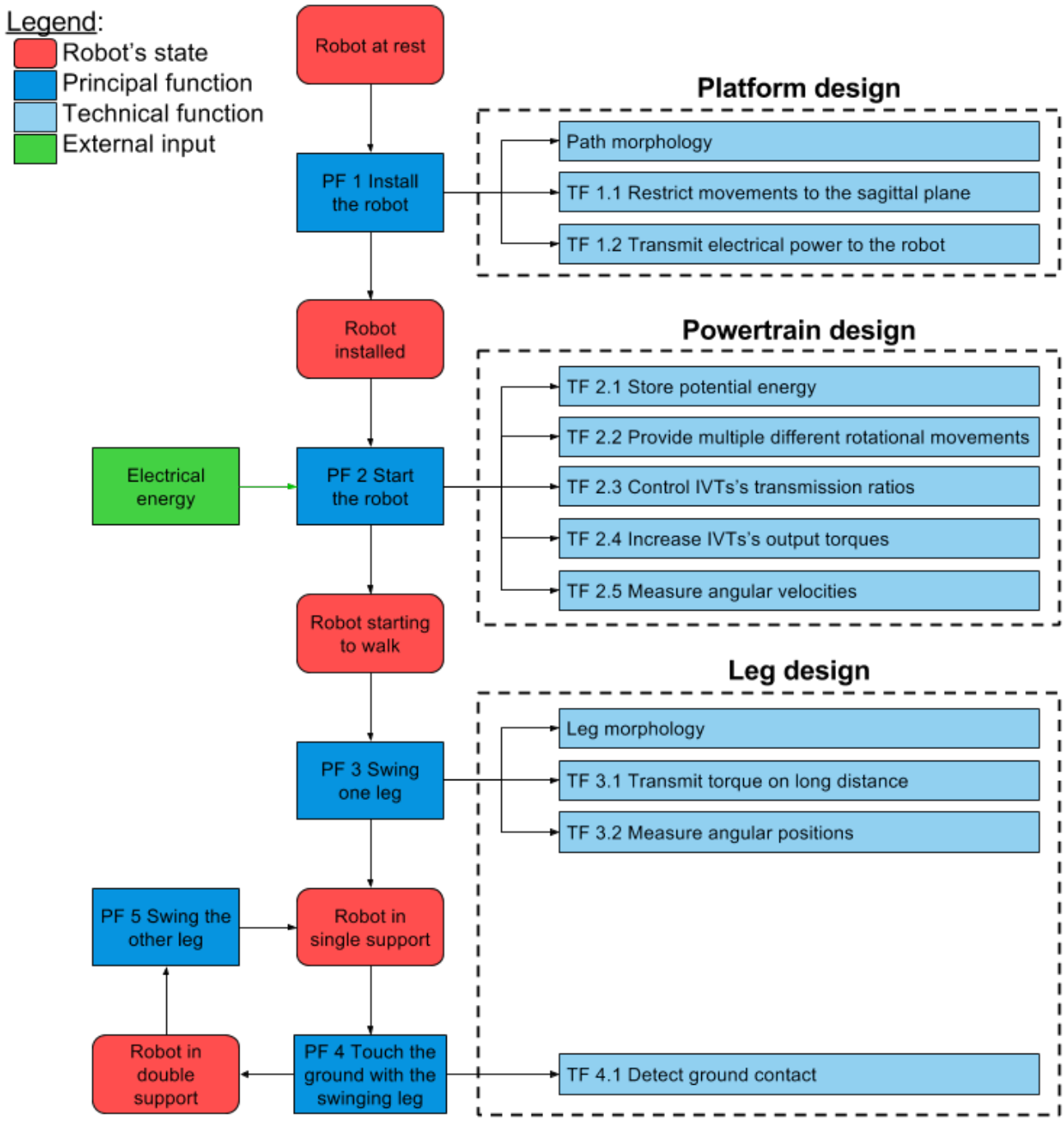

Figure 3.1: Function analysis flow chart

The robot is initially at rest before being installed on its platform, which is used to restrict its movements to the sagittal plane and to transmit electrical power from the network to the robot.

Once installed, the robot is started thanks to electrical energy provided by the network. In order to

damp the variations of power required by the robot, the power motor charges a mechanical energy storage and more precisely stores potential energy. From this single power source, the robot has to drive four different rotating shafts, with a possible power exchange between them. The latter corresponds to the input shafts of the IVTs actuating the joints of the robot. Moreover, the transmission ratio of each IVT has to be controlled and is set by a smaller motor. Besides, the required torques at the different joints are in the order of 100 [Nm], which is significantly greater than the torque delivered by the IVT that is about 1 to 3 [Nm]. The system therefore requires an additional transmission ratio between the IVTs' outputs and the legs' joints.

After being started, the robot begins to walk by swinging its legs one after the other. The actuation of the joints and more specifically the transmission of the torque from the outputs of the powertrain to the joints will be seen as a function of the leg morphology.

During the walk, several quantities have to be measured to control the different parts of the robot, such as the angular velocities and the angular positions. The robot also needs to detect when its swinging leg touches the ground.

From this function analysis, it is possible to separate the design of the robot into three different parts: the platform design, the powertrain design and the legs design. For each of these parts, technical functions have been defined (see figure 3.1).

3.3 Elaboration of morphological matrices

This section is divided into three stages, corresponding to the three different divisions of the design: the platform, the powertrain and the legs. For each technical function of these three parts, several possible solutions are presented in morphological matrices. These latter regroup all solutions in the form of drawings and will then be used to build global solutions.

3.3.1 Platform design

First, the connection between the network and the robot, called the platform, is studied. The solutions for the technical functions related to the platform are given in table 3.1.

Path morphology: The robot is only allowed to move in its sagittal plane. Two solutions are commonly used in existing robots to satisfy this condition, as it has been presented in the first chapter (page 3). The first one is to connect the robot to a rotating tower with a boom so that it walks in a circle. If the radius of the circle is sufficiently large compared to the size of the robot, the curvature can be neglected and it can be assumed that the robot only moves in its sagittal plane. The second solution is to install the robot on a treadmill of which the speed is synchronised with the gait of the robot. In this thesis, it was agreed to combine those two solutions and to be able to switch between them. In order to do that, a treadmill is simply placed at some point of the circular path.

TF 1.1 Restrict movements to the sagittal plane: The first purpose of the boom is to restrict the movements of the robot to its sagittal plane. Ideally, the radius of the circular path should be constant but a small variation is allowed to simplify the design. During the walk, the height of the trunk of the robot slightly varies and the robot leans forward in order to keep its balance. The system has thus to allow these movements but in a limited range to prevent the robot from falling. To fix the motion limits, mechanical stops can be added at the different joints, as well as safety cables attached on the robot or on the boom. Besides, the weight of the boom has to be compensated to reduce its impact on the gait of the robot.

The first solution represented in the morphological matrix consists in using as boom a single beam that is connected to the tower by mean of linear bushings. These latter allow both translational and rotational movements. To allow the robot to lean forward, the connection between the end of the boom and the robot is realised by a plain bearing. The two others solutions also use this connection to enable the robot to lean. In the second solution, the linear bushings are replaced by bearings on the tower and a slider at the end of the boom. In the third solution, a four-bar linkage is used instead of a single beam and is connected to the tower with bearings.

Due to the length of the boom (i.e. 2 [m][2]), the bending of a single beam cannot be neglected. This deflection could however be used as a solution to the vertical translation of the robot. Indeed, the height of the robot varies by about 5 [cm][3] during a step, which is an achievable amplitude for the deflection of a two metre long beam. However, this approach has not been considered in this thesis because of the unreliability of this solution. The deflection of the beam is therefore a characteristic that has to be minimised in the dimensioning of the boom.

TF 1.2 Transmit electrical power to the robot: The second purpose of the boom is to connect the robot to its platform and to transmit electrical power and sensor signals between them. A classical solution uses electrical cables and a commutator/brushes system at the tower connection. Another solution is based on the magnetic induction effect: electrical power is transmitted to the boom by intercepting a magnetic field produced at the tower.

Table 3.1: Morphological matrix for the platform design

Principal function	Technical functions	1	2	3
PF 1 Install the robot	Path morphology	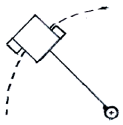	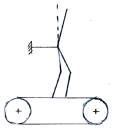	Both
	TF 1.1 Restrict movements	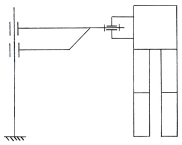	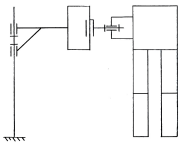	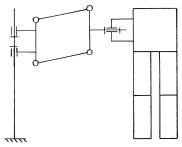
	TF 1.2 Transmit electrical power	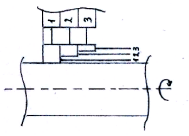	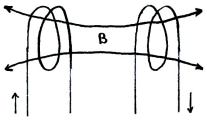	

3.3.2 Powertrain design

In a second stage, the design of the powertrain is discussed. The powertrain corresponds to the mechanical transmission from the main motor to the legs's transmission, including the energy storage, the differentials, the IVTs and the reducers. All solutions for this part of the design are given in table 3.2.

[2]This value has been fixed in the specifications (see Appendix A page 87).
[3]See the results in chapter 5 (page 45).

TF 2.1 Store potential energy: The first action of the powertrain consist in storing mechanical energy to damp the required power curve of the power motor. Two main types of solutions emerge: springs, which can in turn be divided into torsion springs or linear springs, or pneumatics. The first solution consists in a spiral spring contained in a barrel, attached to both the input and output shafts of this mechanical storage. This spring is charged at one end by the power motor and discharges more or less quickly at the other end depending on the power required by the joints. The second solution uses a linear spring, loaded in compression, combined with a ball screw which converts the rotational movement of the power motor into a linear movement. This ball screw has to be reversible and not self-locking in order to allow the spring to discharge. Concerning the pneumatic solution, it uses a compressor to store compressed air in a tank and releases it later in a turbine. This technology is called CAES, which stands for "Compressed Air Energy Storage".

TF 2.2 Provide multiple different rotational movements: To actuate multiple shafts from the output shaft of the power motor, either differentials or planetary gears trains can be used. These two solutions allow to have a power exchange between the different IVTs through the variations of angular velocities. As will be further explained, they will both be used in the global solution that has different possible morphologies.

TF 2.3 Control IVTs' transmission ratios: The IVT's transmission ratio is controlled through the linear displacement of a plate (or ring). In the design of the IVT made by Christophe Everarts [36], this movement is performed using a small motor and several screw threads synchronised with a toothed belt. Another solution for this translation is to use a rack and pinion mechanism rather than screw threads. Ball screws can also be used as they are more efficient. But this implies that the control of the IVT is reversible, since ball screws are not self-locking. This solution is therefore discarded.

TF 2.4 Increase IVTs' output torques: As already mentioned in the function analysis, the IVTs do not allow the transmission of a torque as high as required by the legs's joints. Their output torque has thus to be increased. The first solutions are the more classical ones: gearboxes with two or three gear stages or planetary gears trains. Another solution [41] consists in actuating a ball screw with the IVT, inducing thus a linear motion. This ball screw is attached to a rope or a belt connected to a pulley. This latter rotates as the ball screw moves and it drives the concerned leg's joint. Moreover, the ball screw has to be reversible and not self-locking in order to allow an exchange of energy between the joints. Alternatively, a harmonic drive [42] could be used. This indeed allows a high transmission ratio with a compact and efficient design and is often used in robotics. This component is an application of the strain wave gearing theory based on elastic dynamic using the flexibility of metal [43].

TF 2.5 Measure angular velocities: In order to control the motors, angular velocities have to be measured, which is done using sensors. The choice of these sensors does not impact the powertrain design, but rather the accuracy of the control. The two main solutions for this kind of sensor are the optical encoder and the electromagnetic sensor.

Table 3.2: Morphological matrix for the powertrain design

Principal function	Technical functions	1	2	3	4
PF 2 Start the robot	TF 2.1 Store potential energy	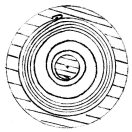	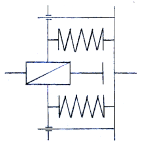	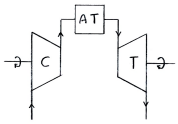	
	TF 2.2 Multiple actuation	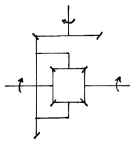	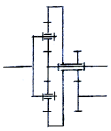		
	TF 2.3 Control IVT's ratio	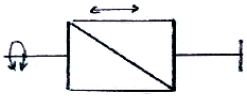	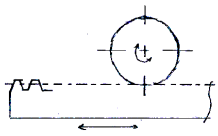		
	TF 2.4 Increase IVT's output torque	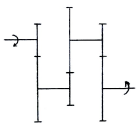	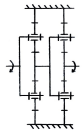	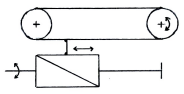	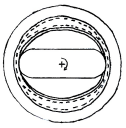
	TF 2.5 Measure angular velocity	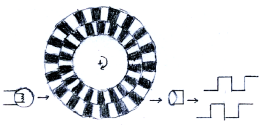	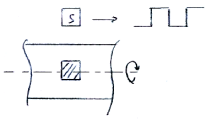		

3.3.3 Leg design

The last part of the design concerns the legs. This includes the last transmission between the powertrain and the joints (in particular the knee) and the leg morphology. The solutions are presented in table 3.3.

Leg morphology: Two leg morphologies emerge from existing bipedal robots (see chapter 1, page 3). In most cases, classical humanoid legs are used, allowing to keep the robot human-like. The actuators of the knees are usually included in the thighs of the robot. But given the specifications, this solution is immediately rejected because all the powertrain has to be contained in the trunk, including the actuators of the knees. This requires thus a transmission between the trunk and the knees. The second solution uses a four-bar linkage in order to displace all the joints that have to be controlled at the same location and to have a lighter design. The kinematics of both kinds of leg morphology is identical but the control and the robustness differ.

TF 3.1 Transmit torque on long distance: The actuation of the hip joint is the easiest to perform. It can indeed be directly connected to the powertrain's output. Otherwise, the use of a usual transmission

such as a toothed belt or gears (spur or bevel, depending on the geometry) is conceivable given the short distance between the powertrain and the hip. The best solution will depend on the design of the powertrain.

The actuation of the knee joint is however more complex because it absolutely requires a transmission on a long distance. Since the transmission requires accuracy and it operates at low speed, the most common solution is a toothed belt. Roller chains and silent chains are also potential solutions but will be eliminated early in the design due to their bad efficiency and their vibrations, as can be seen later. The last solution is a traction cable that is attached to a pulley and to the calf so that when the pulley turns, the cable is drawn, and the leg segment is pulled. A small protuberance before the attachment on the leg allows to increase the transmissible torque. This mechanism is similar to the one of an humanoid leg.

The morphological matrix 3.3 only regroups the solutions for a long distance torque transmission. The gears being too cumbersome compared to the other solutions, they are therefore eliminated.

TF 3.2 Measure angular positions & **TF 4.1 Detect ground contact:** To control the robot, angular position sensors on the different joints are needed and can either be optical encoders or angular potentiometers. For its control, the robot also has to perceive when its legs are in contact with the ground. It can thus either be equipped with force sensors at its point feet or with micro-switches.

Table 3.3: Morphological matrix for the leg design

Principal functions	Technical functions	1	2	3	4
PF 3 Swing one leg & PF 5 Swing the other leg	Leg morphology	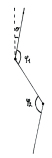	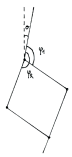		
	TF 3.1 Transmit torque on long distance		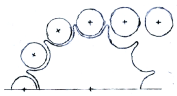	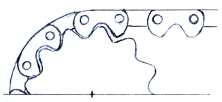	
	TF 3.2 Measure angular position	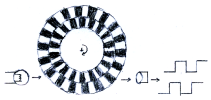	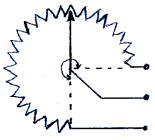		
PF 4 Touch the ground	TF 4.1 Detect ground contact	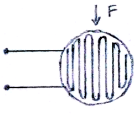	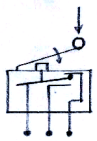		

3.4 Establishment of comparison criteria

The solutions presented above will be compared in the next section according to several predetermined criteria which are:

- Feasibility: it regroups the ease of dimensioning and assembling the mechanism and how much complexity is added to the rest of the design or to the simulation.
- Robustness: it concerns the solidity of the design and its expected lifetime.
- Weight: it takes into account the weight and/or the cumbersomeness of the solution. This is an important parameter in the design because a heavier solution implies that more power is needed.
- Efficiency: it relates to the efficiency of the power transmission and therefore to the power consumption.
- Cost: it refers to the manufacturing and maintenance costs but also to the equipment to buy or that is reusable from/for other experiments and is sometimes difficult to assess before the dimensioning.

These criteria will help to compare the different solutions through a relative comparison. Moreover, the criteria can be weighted, especially in the case of a tie.

For the design of the legs, a special criterion is added, namely the aspect. Indeed, as already explained, the morphology of the legs of bipedal robots is divided into two main categories: the humanoids and the ground-running birds. It is chosen in this master thesis to privilege a humanoid aspect. The reason behind this choice is to simplified the comparison of the datas retrieved from the simulation with humanoid profiles like those from David A. Winter [33].

3.5 Generation and comparison of solutions

In this section each part of the design is discussed and compared according to the criteria established above. At first, the independent solutions of the technical functions from the morphological matrices are compared and the best is selected. Then, one or several global solutions are generated mixing the chosen solutions with the rest of the morphological matrices. In the case of the powertrain solution, the general morphology is fixed, but the implementation presented here is the consequence of multiple optimisations. The global solutions generated for the platform and the leg are then compared according to the pre-established criteria. The final solution for each part of the design are finally presented.

3.5.1 Platform design

Both circular and straight paths present interesting features. The straight path on a treadmill is easier to build, is easier to simulate and needs less space. On the other hand, the circle path allows to change the height and composition of the path in order to simulate various terrains. In order to be able to use both paths, the robot is connected to a central tower with a boom. To switch to the straight path, a treadmill is simply placed at some point of the circular path.

TF 1.1 Restrict movements

The different solutions for the technical function TF 1.1, the design of the boom allowing to restrict the movement of the robot in the sagittal plane, are compared in the table 3.4.

The first solution, using linear bushings combining rotation and translation, is taken as a reference. Even if the cost of linear bushings is quite high, this solution provides good efficiency for both movements.

Table 3.4: Comparison platform design: TF 1.1 Restrict movements

Criteria	Solution 1 Bushings	Solution 2 Slider	Solution 3 Four-bar
Feasibility	0	0	−
Robustness	0	−	+
Weight	0	0	0
Efficiency	0	−	0
Cost	0	+	+
Total	0+ / 0−	1+ / 2−	2+ / 1−

The weight of the boom is considered as similar in all three solutions. Indeed, if the four-bar linage possesses more beams, those are lighter as there is less effort present.

The second solution, with a slider for the vertical translation, offers a cheaper solution compared to the expensive linear bushings, but trades it for a lesser efficiency. Moreover, the risk that the slider gets stuck due to the bending of the long beam makes this solution less robust.

The third solution, using a four-bar mechanism instead of a single bar as a boom, grants a high robustness to the mechanism. The boom will indeed be free of shear stress with the rotating joint of the four-bars mechanism. These joints are bearings which are cheaper than the linear bushings for an equivalent efficiency. This represent another advantage. With this solution, the variation of height of the robot induces a slight variation of the radius of the circular path. But this is negligible. The dimensioning of the four-bar mechanism may however be a bit trickier than the one of a single beam.

From the table 3.4 that summarizes the cited arguments, the third solution emerges as a more reliable and cheaper solution. Replacing the linear bushings by plain bearings in the first proposal could reduce the cost but this would lead to an even less robust and efficient solution. The four-bar mechanism is therefore kept as the solution for the design of the boom.

TF 1.2 Transmit electrical power

The proposals for the transmission of electrical power in the platform are compared using the brushes collector as reference in the table 3.5.

The magnetic induction allows to transmit electrical power on a relatively long distance compared to the brushes collector (needing a physical contact). But the more the distance increases, the more the efficiency decreases. Moreover, this distance may be variable, impacting the robustness of the system. A second parameter impacting the robustness is the influence of the environment on this magnetic field, or the influence of this magnetic field on the environment or even worse, on the robot. Finally, the cost of the components needed to build this solution are a lot higher than the cost of a single brushes collector and some electrical cables.

Table 3.5: Comparison platform design: TF 1.2 Transmit electrical power

Criteria	Solution 1 Brushes	Solution 2 Magnetic
Feasibility	0	–
Robustness	0	–
Weight	0	0
Efficiency	0	–
Cost	0	–
Total	0+ / 0–	0+ / 4–

Therefore, the brushes collector is kept as solution for the technical function TF 1.2.

Platform solution

By regrouping the solutions chosen to all independent technical functions described above, the global solution for the platform is then generated. The figure 3.2 presents the solution designed.

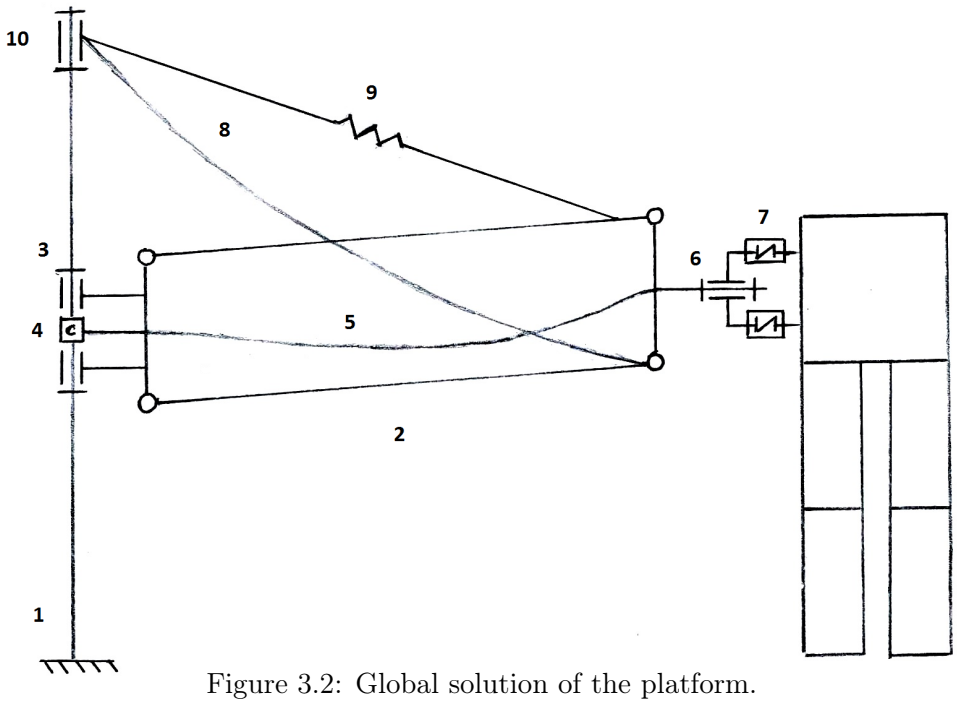

Figure 3.2: Global solution of the platform.

The central tower simply consist of a hollow pole (1), fixed vertically with respect to the ground. As the shaft is fixed and the rotating part is the hub composed of the four-bar linkage (2) constituting the boom of the platform, bearings are mounted in a "o" configuration (3). The brushes collector (4) is fixed between the two bearings. This piece provides the connection between the fixed electrical cable running inside the pole and the electrical cables attached to the rotating boom. The cables (5) are kept loose from the tower to the robot in order to allow slow deformations. The plain bearing (6) at the end of the boom ensures the last movement authorized to the robot, bending forward. Elastic couplings (7) are added between this joint and the robot to damp unwanted vibrations and shocks. A safety cable (8) is attached to the end of the boom, to prevent the robot from falling. An elastic cable (9) is also present

compensate the weight of the boom as much as possible. Those two cables are attached at the top of the central tower, with a conical bearing (10), to follow the rotational movement of the boom.

3.5.2 Powertrain design

The general morphology of the powertrain was shown in the figure 2.8 in the previous chapter.

The kinematic scheme of the powertrain is built from this scheme by replacing the black boxes by solutions from the morphological matrix in table 3.2. At first, a technical solution for the energy storage is selected. In a second time, the comparison of the solutions to increase the output torque of the IVT ends the choice of black boxes contents. Then, the kinematic scheme of the powertrain is settled after optimisation some characteristics of the powertrain.

The choice of solution to the technical function TF 2.3 Control IVT is not explained here because the original solution of the design of the IVT from Christophe Everarts [36] is kept. It consist in using several screw thread synchronized with a timing belt.

The electrical part of the design (i.e. sensors) is not developed neither. Indeed, the choice of sensors will impact the precision of the control but not the mechanical pre-dimensioning.

TF 2.1 - Energy storage

The comparison of mechanical potential energy storage takes the spiral spring as reference in the table 3.6. This solution allows a high number of turns in the spring and therefore has a lot of energy stored. Moreover, after a sufficiently high number of turns, the output torque of the spiral spring is nearly constant.

Table 3.6: Comparison powertrain design: TF 2.1 Store energy

Criteria	Solution 1 Spiral spring	Solution 2 Linear spring	Solution 3 CAES
Feasibility	0	+	−
Robustness	0	0	−
Weight	0	0	−
Efficiency	0	−	−
Cost	0	0	−
Total	0+ / 0−	1+ / 1−	0+ / 5−

The second solution mainly suffers of a lesser efficiency. Indeed, the linear springs are easier to dimension and to assemble than the spiral spring, but they can store less energy for an equivalent volume.

The third solution is the CAES. This solution present no advantage, whatever the criterion. The components of such a system are complicated to design and manufacture. They therefore are more expensive. The system needs a lot more space than a single spring. Moreover, the efficiency of the different parts such as the compressor and turbine have a relatively bad efficiency. This solution is therefore not feasible for a system of the size of this design.

The solution of the spiral spring is then selected as the potential mechanical energy storage.

TF 2.4 - Increase torque

The first solution for transmission ratio is the simple gearbox. This solution is used as reference in the table of comparison 3.7.

The efficiency criterion is based on the assumption of a transmission ratio of 100:1. Each solution has its efficiency approximated, using general values of efficiency used in mechanical design [44]. For the first solution, a single stage of gears may has a maximum gears ratio of 5:1 with an efficiency of 94%. Therefore three stages of spur gears are needed to obtain a ratio of maximum 125:1. This gives an approximated efficiency of 83%.

Table 3.7: Comparison powertrain design: TF 2.4 Increase torque

Criteria	Solution 1 Gearbox	Solution 2 Planetary box	Solution 3 Ball screw	Solution 4 Harmonic drive
Feasibility	0	0	−	−
Robustness	0	+	0	+
Weight	0	+	+	+
Efficiency	0	+	+	+
Cost	0	0	0	-
Total	0+ / 0−	3+ / 0−	2+ / 1−	3+ / 2−

The second solution uses planetary gears in series. The generally high number of teeth on the ring allows to have a greater transmission ratio than a simple stage of spur gears (10:1 instead of 5:1). It is commonly accepted that planetary gears have 3% of losses per stage [45]. Only two stages are needed, giving a efficiency of about 94%. Moreover, with the multiple planets between the sun and the ring, the number of teeth in contact is increased. This allows to have smaller gears for a same load. The spur gears may be replaced by helical gears in both solution without changing this comparison. In both case this increases the admissible load and transmission ratio but increases the axial load in the different shafts.

The third solution is a design retrieved from a prosthesis developed by the MIT [41]. The design is more complex than a simple gearbox, and the range of motion is by definition limited to a certain displacement of the belt on the pulley (at the contrary of the gearbox). The ball screw allows to have a huge transmission ratio with a good efficiency ($> 90\%$) in a single stage. But coupled with the belt, the efficiency of this solution decreases.

The last solution is the harmonic drive. This technology offers many advantages: compactness, high gear ratio, reconfigurability, efficiency, high torque, no backlash. The main disadvantage is the price, a lot higher than the other proposed solutions. Another disadvantage is the complexity of the mechanism using strain wave gearing theory, not covered in this thesis. The harmonic drive allows a transmission ratio from 30:1 up to 320:1 for the same space [43]. The efficiency of the harmonic drive is above 90%.

The solution chosen to increase the torque at the output of the IVTs is the succession of planetary gears trains. The ball screw solution was a suitable candidate, but including this solution to the design induces smaller IVTs, which would be too complex to manufacture.

Powertrain Solution

Now that the components of the technical functions are chosen, the kinematic scheme of the powertrain can be drawn. The objective is to optimize the transmission chain by minimizing the number of contacts and maximizing the size at disposal for the IVTs. The layout has to respect the given dimensions of the trunk of the robot and the output disposition. This is performed by choosing the type of mechanical differential used for the first and second stages. Another geometrical constraint, added along the optimisation, is to minimize the distance between the legs of the robot.

The figure 3.3 shows the result of this optimisation. The powertain being identical for the right and left leg, only one of them is represented for clarity.

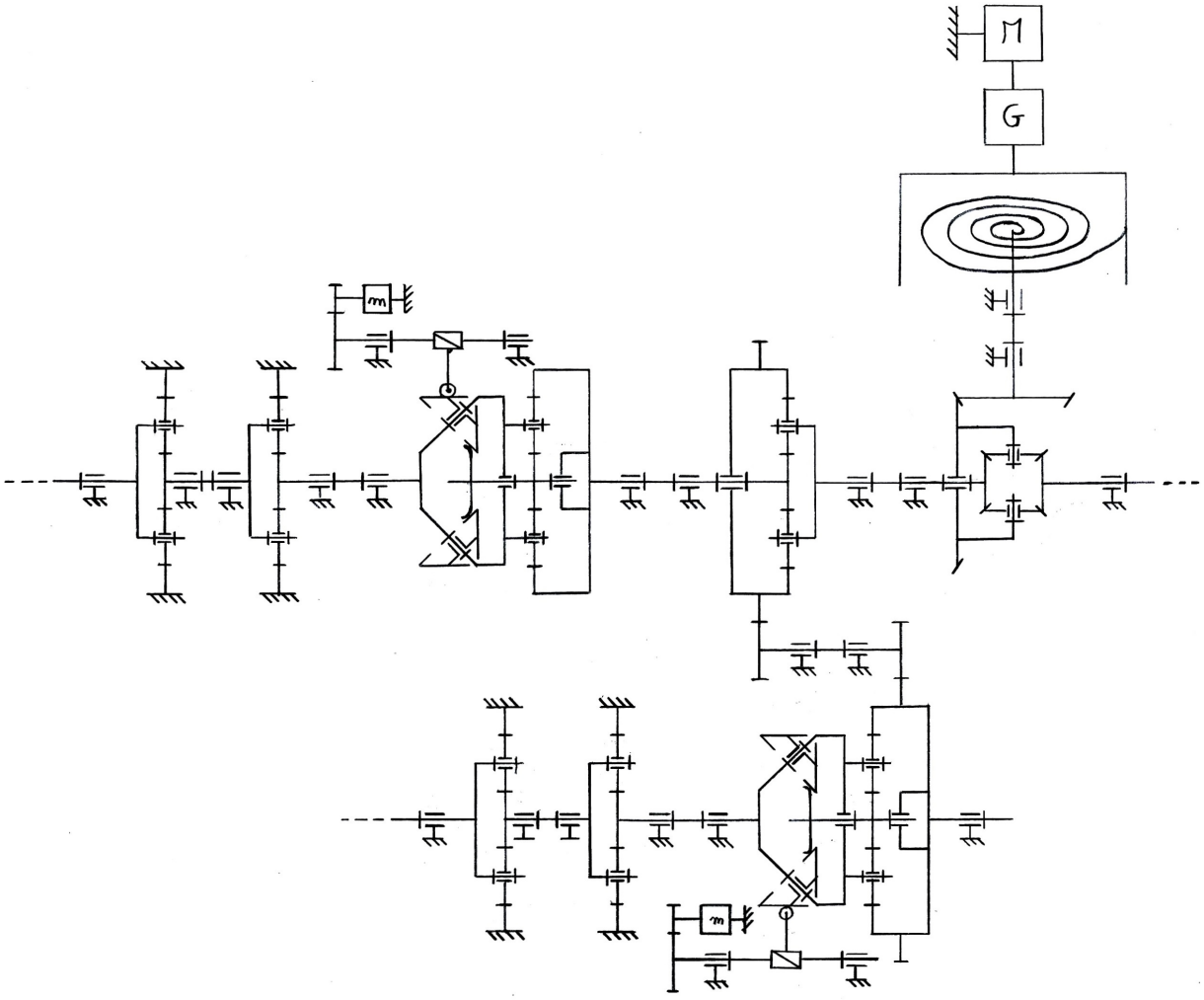

Figure 3.3: Powertrain's kinematic scheme of one half of the robot.

From a top-down approach, the powertrain starts with the power motor and its gearbox.

The spiral spring inside its barrel is fixed to the output of the gearbox and is discharged into the rest of the circuit. A large diameter is needed for this spring. It is chosen to install it at the top of the robot above the other elements. This allows to use the all width of the robot for the spring and not be restrained by the rest of the mechanism.

The first mechanical differential used is similar to the one used in automotive. It separates the design into the left and the right leg with turn angles. This design is similar to a planetary gears train with bevel gears. The input from the spring drives the planet carrier of the angular planetary gears train. A

transmission ratio is possible between these two elements. The ring and the sun are bevel gears with the same pitch diameter. This allows to distribute the torque equally between the two legs of the robot. The rotational speed of the input is the mean of the speed of the two outputs. Therefore, if one of the output changes its speed, the other compensates it, allowing an exchange of energy. Since the two legs' cycle are shifted of half a period, this permits to have a maximum of energy exchanged.

The second stage of differentials uses classical spur planetary gears, with the planet carrier as input. The first output, the sun, is mounted on the same shaft as the input of an IVT. The ring of this second mechanical differential is both an internal and external gear. The external teeth of this ring drive a smaller gear which in turn drives the ring of the second IVT. This allows to have the same direction of rotation in both IVTs. This intermediate shaft is also used to displace the input of the second IVT as close as possible to the center of the robot. This allows to minimize the distance between the two legs.

The IVTs have thus their planetary ring as input and therefore the planet carrier of the CVT as output. The linear motion controlling the transmission ratio of the IVT is ensured with a smaller motor actuating a screw thread.

Finally, two stages of planetary gears trains allow to increase the output torque to the desired range of values.

The mechanism from the power motor to the input of the IVTs always turns in the same direction, and the spiral spring allows to load the mechanism always in the same direction. There is therefore no backlash in the gears or play in the shafts in this part of the powertrain. This offers some advantages in efficiency and robustness of the transmission.

3.5.3 Leg design

The last transmission before the joint has to be selected between the solution proposed. Afterwards solutions are generated with the leg morphology and the chosen transmission. Different combination are possible, offering different advantages.

TF 3.1 - Long distance transmission

The toothed belt is the solution taken as reference for the comparison in the table 3.8. This solution ensures the synchronization and precision of the transmission on a long distance.

The solutions 2 and 3 use chains, which offer a similar efficiency to toothed belt. The chains however need lubrication and therefore a container, adding weight to the mechanism. The main disadvantage of the chains is that they add a lot of vibration in the rotary motion. The transmission has to be as smooth as possible, making these solutions less suitable than toothed belt. The roller chain is cheaper than a timing belt, but the silent chain has a similar cost.

The fourth solution, using a traction cable, is similar to the functioning of a humanoid leg. The geometry of the knee contact is to be dimensioned to ensure a correct transmission ratio for each desired leg configuration. The range of motion is limited to the humanoid leg positions. This solution may be less robust to impact loading, expected at the moment of the contact of the leg with the ground. This solution is nearly weightless, which is a particularly interesting criterion for the leg design. But the traction cable offers a lesser efficiency compared to a toothed belt.

Table 3.8: Comparison leg design: TF 3.1 Transmission on long distance

Criteria	Solution 1 Toothed belt	Solution 2 Roller Chain	Solution 3 Silent Chain	Solution 4 Traction cable
Feasibility	0	0	0	−
Robustness	0	−	−	−
Weight	0	0	0	+
Efficiency	0	0	0	−
Cost	0	+	0	+
Total	0+ / 0−	1+ / 1−	0+ / 1−	2+ / 3−

The toothed belt is kept as solution to transmit the torque to the leg's joints.

Leg solution

With the transmission selected, solution are generated. The first solution uses a belt to both of the joints. The second solution uses the four-bar mechanism as in the robot ATRIAS [15]. One of the actuation is directly mounted on the powertrain while the other one uses a belt. The third solution uses two belts in series for the actuation of the knee, and the hip is directly mounted on the output of the powertrain. The kinematic schemes of these solutions are represented in the figure 3.4, 3.5 and 3.6 respectively.

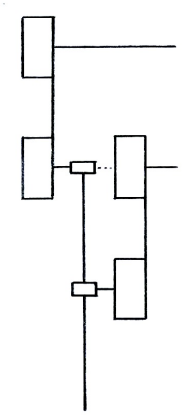

Figure 3.4: First solution of leg design, with a belt actuating each joint.

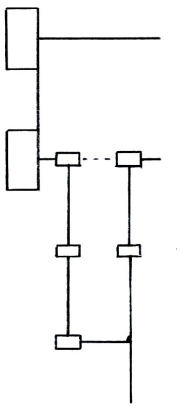

Figure 3.5: Second solution of leg design, with a four-bar mechanism.

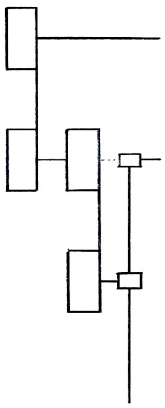

Figure 3.6: Third solution of leg design, with two belt in series and a direct mounting.

The first solution is taken as reference in the comparison table 3.9. This solution allows to distribute the loss in efficiency inherent to the belt between the two joints, rather than concentrating it only on the knee. It also gives another usable transmission ratio between the powertain and both joints. This could reduce the ratio needed into the powertrain, but would increase the weight on the leg since the greatest pinion would be on the knee.

Table 3.9: Comparison leg design solution

Criteria	Solution 1 Belt	Solution 2 Four-bar	Solution 3 Series belt
Feasibility	0	−	0
Robustness	0	+	0
Weight	0	+	0
Efficiency	0	−	0
Cost	0	0	0
Total	0+ / 0−	2+ / 2−	0+ / 0−

The second solution uses the particular morphology of a four-bar mechanism as a leg. This configuration does not change the kinematical behaviour of the contact point. However, some modifications are to be added to the simulation in order to apply the Neuromuscular model to this leg configuration [40]. A mathematical transformation to the angles and torques profiles allows to transform the four-bar into a virtual leg with the same morphology of the first solution. The Neuromuscular model is applied to this virtual leg and the results are transformed back to the four-bar configuration. For the mechanical point of view, the four-bar offers a better robustness and a lighter leg. By developing the mathematical transformation, one can found that this solution will require higher torques than in the case of a simple leg.

The aspect is however another criterion to be dealt with. Thus, as it has been decided to prefer humanoid like legs, this second proposal is not adopted.

The third solution is similar to the first one but the belts are put in series to actuate the knee and the hip is directly mounted to the powertrain.This solution offers thus a different approach to the combination with the powertrain.

The first and third solutions offer the same performances in all criteria. Therefore, the choice of solution is justified by geometrical constraints with the combination of the legs with the powertrain. The third solution is kept as it allows to reduce the distance between the two legs of the robot. In the first design, this distance would indeed increase due to the stage of belt and pinions. A 3D drawing of the legs and powertrain solutions is presented in figure 3.7.

Additional features may be needed further in the thesis. As example, in the case of huge impact forces with the ground, spring could be attached to the last segment of the leg to damp the impact. This appears in the robot DURUS-2D [4], designed to run. The run implies greater impact forces.

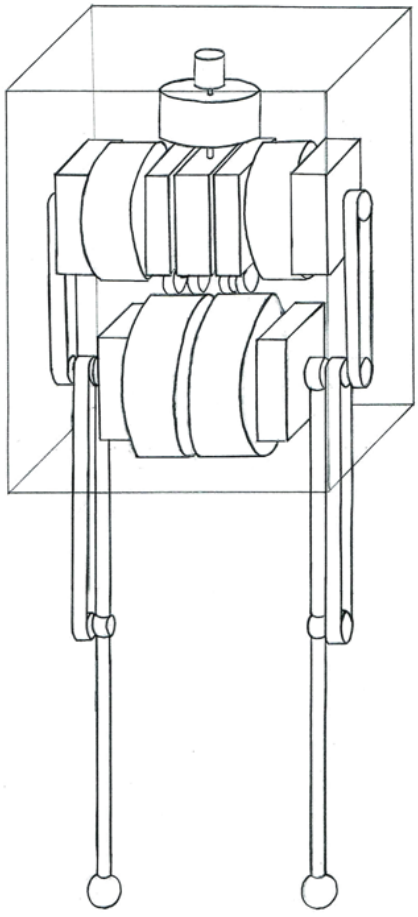

Figure 3.7: 3D drawing of the leg and powertrain solutions.

Chapter 4

Hierarchical controller and simulation

This chapter presents the controller and the simulation that have been developed in order to determine the quantities required for the design such as the torque profile in each joint, the power profile during the walk, the evolution of the position of the centre of mass, etc. The diagram of the simulation is represented in figure 4.1.

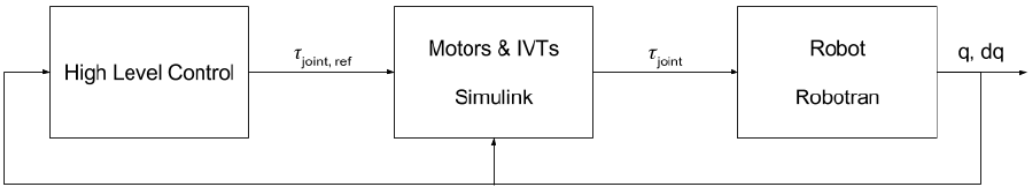

Figure 4.1: Simulation diagram.

There are three main parts in this diagram. First, the high level controller computes the referential torques $\tau_{joints,ref}$ to apply to the joints of the bipedal robot on the basis of their angular positions q, angular velocities dq and whether its legs are in contact with the ground, in order to perform a humanoid walking gait. Then, these referential torques are given as inputs of a Simulink file, which corresponds to the mid-level controller. This latter represents the whole powertrain and the transmission to the legs (see previous chapter) and computes thus the torques that will really be applied to the joints, τ_{joints}. Finally, these torques are applied to the robot that has been modelled in Robotran, where the angular positions and velocities can be retrieved, as well as whether of not the legs are in contact with the ground.

These three parts are presented in more detail here below.

However, as it will be explained in the section about the mid-level controller, the Simulink file was not integrated in the C/C++ implementation due to a lack of time. What has thus been implemented in the C/C++ project is divided into three parts: the files about the high-level control, the ones about the simulation and others making the interface between both. Therefore, the implemented case is the ideal one as the torques sent to the modelled robot are the referential torques.

4.1 High-level control

The high-level controller that was implemented is a neuromuscular controller which is based on a model developed by Hartmut Geyer [40], as already mentioned in the previous chapter. This model is a model of human locomotion that is controlled by muscle reflexes which encode principles of legged mechanics.

Moreover, it considers the human body to be one trunk and two three-segment legs. The latter are actuated by seven Hill-type muscles, which allows to make a direct comparison with the main muscles of the human leg [40].

Nevertheless, as the robot designed in this thesis has no feet, slight modifications need to be made to Hartmut Geyer's model such as considering two-segment legs instead of three-segment legs and removing the muscles related to the feet. The model described below is the model developed by taking those modifications into account and corresponds thus to what was implemented for this thesis. The explanations below summarise [40] and are thus strongly inspired by it.

Moreover, the implementation realised for this master thesis is strongly based on the one done by Nicolas Van der Noot as part of his doctoral thesis about the development of neuromuscular controllers to achieve human-like locomotion for the humanoid robot COMAN [46] (see the description of this robot in the first chapter) and is done in C/C++ code.

This section is divided into four parts. First, the neuromuscular model is presented. Then, the description of the reflex control is translated into the equations of the stimulations of the muscles. Next, the values of the parameters of these equations are given as well as the description of the optimisation realised to obtain them. Finally, it is explained how muscle stimulation translates into muscle force using the muscle-tendon model of the muscles. The torques that have to be applied to the joints can then be determined on the basis of the forces.

4.1.1 Description of the neuromuscular model

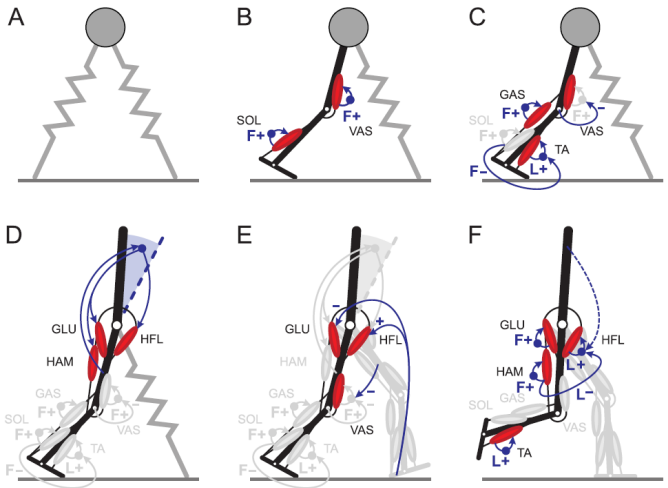

Figure 4.2: Evolution from the spring-mass model to the neuromuscular model [40]. The neuromuscular model represented here is more complex than the one implemented in this thesis as it takes the feet into account.

First of all, the human model is based on the bipedal spring-mass model, which allows to simplify human locomotion to a point mass moving on two massless spring legs (see figure 4.2 A). Such a model represents the centre-of-mass dynamics that is observed in human walking and running. However, a neuromuscular model better represents the human morphology. This spring-mass model can thus be turned into a neuromuscular one following three steps. First, the springs are replaced by two two-segment legs. Then, the point mass is replaced by a trunk. During these two first steps, muscles are added to the model in order to ensure a compliant stance behaviour as well as balance control. Finally, swing leg control is added

to this model to allow it to enter cyclic locomotion. Each of these steps is further described below.

Replace the leg springs by segmented legs

First, each spring of the spring-mass model is replaced by a segmented leg that has a thigh and a calf but no foot. Moreover, a vasti muscle group (VAS) is added and generates its own muscle activity in stance using a positive force feedback (F+) (figure 4.2 B) allowing to generate a compliant leg behaviour.

Furthermore, in order to prevent knee overextension, the biarticular gastrocnemius muscle (GAS) is added and it also uses F+ during the stance phase (figure 4.2 C). As in the case of the VAS, this muscle reflex contributes to the compliant leg behaviour. Then, an additional security concerning the knee overextension is the inhibition of the VAS if the knee extends beyond a certain threshold, $\phi_{k,off}$. This latter is determined by an optimisation, as explained later on (see 4.1.3).

Replace the point mass by a trunk

Then, the point mass of the spring-mass model is replaced by a trunk segment (figure 4.2 D) that has to be balanced during locomotion. This is done by adding to each leg a gluteus muscle group (GLU) and a hip flexor muscle group (HFL). Both are stimulated with a proportional-derivative signal of the trunk's forward lean angle θ with respect to gravity.

Besides, a biarticular hamstring muscle group (HAM) is also added. Its stimulation is proportional to the one of the GLU in order to counter knee overextension resulting from a large hip torque developed by the GLU when pulling back the heavy trunk [40].

Since the trunk can be balanced by the hip torques only if the legs bear sufficient weight on the ground, the stimulations of these three muscle groups (GLU, HAM and HFL) are thus weighted for each leg proportionally to the amount of body weight (bw) it bears. Therefore, these muscles only contribute to the trunk's balance control in stance.

Add swing leg control

Next, it is assumed that the functional importance of each leg in stance decreases as the amount of body weight borne by the other leg increases. The swing is thus initiated in double support as follows (figure 4.2 E). It should beforehand be noted that the leg which enters stance last is named the contralateral leg while the other is called the ipsilateral leg. The stimulation of the ipsilateral leg's VAS is thus inhibited proportionally to the weight borne by the contralateral leg, allowing the knee to break its functional spring behaviour and to flex. In addition, the stimulation of the HFL is increased by a fixed amount ΔS while that of the GLU is reduced by the same amount in double support. This quantity is determined by optimising the reflex control parameters (see 4.1.3).

During the swing, the leg has a ballistic trajectory that is modulated in two ways (figure 4.2 F). Firstly, the protraction of the leg is facilitated by stimulating the HFL by positive length feedback (L+) since the natural frequency of the purely ballistic movement is too low to ensure a timely foot placement. However, as the required protraction speed depends on the trunk's forward lean, this reflex L+ is biased by the trunk's pitch θ_{ref} at take off (TO). Secondly, gait stability is improved by enforcing swing-leg retraction. Indeed, if the legs have an appropriate orientation during swing, the legged system self-stabilises mechanically into a gait cycle and its tolerance against disturbances broadly improves if a leg retracts before landing. This is ensured by three muscle reflexes. One reflex inhibits the HFL's L+ proportionally to the stretch that the HAM receives in swing. This is done to compensate for the hip rotation resulting from the transfer of angular momentum when the passive knee rotates into full extension during leg

protraction [40]. The two other reflexes, F+ of the GLU and the HAM, ensure that the swing leg not only stops but also transfers part of the actual protraction momentum into leg lowering and retraction [40].

The human model hence developed uses sensors at each foot to detect ground contact, allowing to switch between the different reflexes for stance and swing for each leg, as represented in figure 4.3.

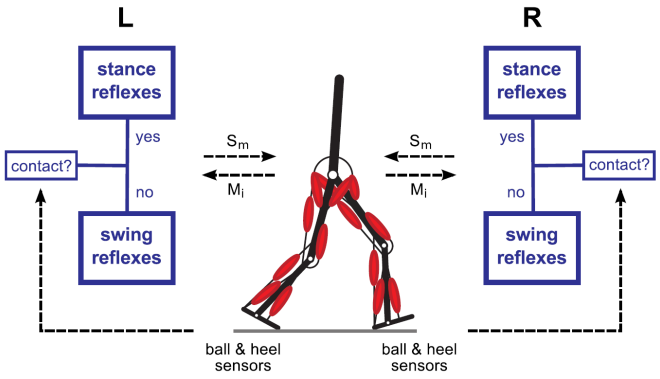

Figure 4.3: Pattern generation [40].

4.1.2 Reflex control equations

Here are presented the muscles' stimulation equations developed on the basis of the description of the neuromuscular model, which are retrieved from [40]. All stimulations are limited from 0.01 to 1 before they produce muscle activations.

But before, it is worth noting that, with a positive force feedback F+, the stimulation $S_m(t)$ of a muscle m is defined as the sum of a pre-stimulation $S_{0,m}$ and the muscle's time-delayed (Δt) and gained (G) force F_m:

$$S_m(t) = S_{0,m} + G_m F_m(t - \Delta t_m)$$

Concerning the positive length feedback L+, the stimulation $S_m(t)$ of a muscle m is expressed as the sum of a pre-stimulation $S_{0,m}$ and the muscle's fibre length $l_{CE,m}$ time-delayed (Δt) and gained (G) stretching or contraction with respect to a length offset $l_{off,m}$:

$$S_m(t) = S_{0,m} + G_m(l_{CE,m} - l_{off,m})(t - \Delta t_m)$$

The stimulations of the muscles in stance are thus defined as follows. In these equations, $DSup$ is equal to 1 if the leg considered is the trailing leg in double support and is 0 otherwise and the $\{\}_{+/-}$ refers to only positive/negative values. Besides, the k coefficients and $\mathbf{F}$ correspond respectively to gains and forces.

$$\begin{aligned}
S_{GAS} &= S_{0,GAS} + G_{GAS}F_{GAS}(t - \Delta t_{GAS}) \\
S_{VAS} &= S_{0,VAS} + G_{VAS}F_{VAS}(t - \Delta t_{VAS}) - k_\phi \Delta\phi_k(t - \Delta t_k)] - k_{bw}|\mathbf{F}_{leg}^{contra}|DSup \\
S_{HAM} &= S_{0,HAM} + \{k_p[\theta(t - \Delta t_{HAM}) - \theta_{ref}] + k_d\dot{\theta}(t - \Delta t_{HAM})\}_+ k_{bw}|\mathbf{F}_{leg}^{ipsi}| \\
S_{GLU} &= S_{0,GLU} + \{0.68k_p[\theta(t - \Delta t_{GLU}) - \theta_{ref}] + k_d\dot{\theta}(t - \Delta t_{GLU})\}_+ k_{bw}|\mathbf{F}_{leg}^{ipsi}| - \Delta SDSup \\
S_{HFL} &= S_{0,HFL} + \{k_p[\theta(t - \Delta t_{HFL}) - \theta_{ref}] + k_d\dot{\theta}(t - \Delta t_{GLU})\}_- k_{bw}|\mathbf{F}_{leg}^{ipsi}| + \Delta SDSup
\end{aligned}$$

In the equation of VAS, $\Delta\phi_k$ is defined as $\phi_k - \phi_{k,off}$ with ϕ_k and $\phi_{k,off}$ the knee angle and the threshold, respectively. Besides, the third term of this equation is only active when $\phi_k > \phi_{k,off}$ and $\dot{\phi}_k > 0$, i.e. when the knee is extending beyond the set limit.

Next, the swing reflexes are given by the following equations in which $\{\}_{PTO}$ refers to a constant value taken at previous take off.

$$
\begin{aligned}
S_{GAS} &= S_{0,GAS} \\
S_{VAS} &= S_{0,VAS} \\
S_{HAM} &= S_{0,HAM} + G_{HAM} F_{HAM}(t - \Delta t_{HAM}) \\
S_{GLU} &= S_{0,GLU} + G_{GLU} F_{GLU}(t - \Delta t_{GLU}) \\
S_{HFL} &= S_{0,HFL} + G_{HFL}[l_{CE,HFL}(t - \Delta t_{HFL}) - l_{off,HFL}] \\
&\quad - G_{HAMHFL}[l_{CE,HAM}(t - \Delta t_{HFL}) - l_{off,HAM}] + \{k_{lean}[\theta(t - \Delta t_{HFL}) - \theta_{ref}]\}_{PTO}
\end{aligned}
$$

4.1.3 Reflex control parameters

Since the segment parameters of the robot of this master thesis (see 4.3) are different from those of Geyer's article [40], the values of the reflex control parameters of the reflex control equations can not be retrieved from this article but must rather be optimised for this case. It should be mentioned that the values of the pre-stimulations $S_{0,m}$ are all equal to 0.01 except $S_{0,VAS}$ of which the value was computed by optimisation as well as the values of the other reflex control parameters.

The optimisation algorithm that was used is an evolutionary algorithm: the CMA-ES algorithm, which stands for "Covariance Matrix Adaptation Evolution Strategy" [47].

An evolutionary algorithm is broadly based on the principle of biological evolution, namely the repeated interplay of variation and selection[47]. More specifically, this means that in each generation, corresponding to an iteration, new individuals, which are the candidate solutions, are generated by varying the current parental individuals. Then, some of these new individuals are selected to become the parents in the next generation on the basis of their fitness or objective function value. By doing so, the individuals that are generated have a better fitness over the generation sequence.

Concerning the CMA-ES algorithm, the distribution according to which the new candidate solutions are sampled is a multivariate normal distribution since it is an evolution strategy. Besides, a covariance matrix is defined to represent the dependencies between the variables in this distribution and its update is achieved through the covariance matrix adaptation method [47].

The implementation of the fitness function of this master thesis has been retrieved from Nicolas Van der Noot's doctoral thesis [46]. However, some changes were made to the parameters values to better fit the case of this master thesis. The implemented fitness function takes three factors into account: the distance, the time and the metabolic energy. The contribution of each of these factors to the fitness value is limited to 100. The fitness computation is done in three stages: first, the fitness related to the distance is computed then the one about the time and finally the one related to the metabolic energy consumption. However, a certain condition has to be fulfilled to move from one stage to the next. The computation of the fitness value as well as the conditions to go to the next stage are presented here below.

Distance This stage computes the fitness related to the distance travelled by the robot. The computation is stopped when a fall is detected, i.e. if the centre of mass of the trunk goes below a defined threshold[1], and does not take walking backwards into account.

The fitness is then computed as follows:

$$\begin{aligned} f_{distance} &= 100 && \text{if } d > lim_{travel} \\ &= 100 \cdot \frac{d}{lim_{travel}} && \text{otherwise} \end{aligned}$$

where d is the distance travelled by the robot and lim_{travel} is the minimal distance wanted to be reached by the robot and was arbitrarily fixed to 15 [m].

Moreover, the condition that has to be fulfilled to go to the time stage is the following:

$$d > lim_{travel}$$

corresponding thus to a fitness value of 100.

Time This second stage calculates the fitness linked to the running time of the robot as follows:

$$f_{time} = 100 \cdot \frac{t}{t_f}$$

where t is the time during which the robot walks and t_f is the total simulation time, that is equal to 30 [s].

Besides, the next stage is unlocked if the following condition is satisfied:

$$t > t_{threshold}$$

with $t_{threshold} = t_f - 1 = 29\,[s]$. If the robot walks until the end of simulation, the fitness value is then equal to 100.

Metabolic energy The third and final stage computes the fitness related to the metabolic energy consumption of the robot, which is the sum of the energy required by its two legs. The energy is calculated at two different points, at two well-defined distances. A first computation of the energy is performed when the robot travelled 7 [m]. Next, a second calculation is done after the same distance as in the case of the fitness computation related to the distance, i.e. after 15 [m]. The energy per distance is then computed on the basis of the two previous calculations:

$$e_{dist} = \frac{e_{15m} - e_{7m}}{15 - 7}\,[{}^{J}/_{m}]$$

Thereafter, the value of the fitness function is calculated as:

$$\begin{aligned} f_{energy} &= 0 && \text{if } d < lim_{travel} \\ &= 100 \exp\left(-\left(\frac{e}{m}\right)^2 \cdot k\right) && \text{otherwise} \end{aligned}$$

with m the mass of the robot (see 4.3) and k the parameter defining the width of the Gaussian (the fitness function). This parameter was adapted so that the value of the fitness function was around 50 to allow the optimisation to not saturate after only a few iterations and thus to improve the obtained results.

[1] This threshold is arbitrarily fixed to 0.45 [m]. Knowing that the centre of mass varies around 0.648 [m], this threshold is acceptable.

However, in order to make the optimisation of the reflex control parameters, the ranges of their acceptable values have to be defined. These are given in table 4.1. Most of these minimal and maximal values are retrieved from Hartmut Geyer's article [40], where they correspond to the limits beyond which it leads to a fall. They obtained these results by considering a previous study for the initial values and by approximating the trunk as an inverted pendulum and the swing leg as a double pendulum driven at the hip.

Some ranges were modified for the implementation of this master thesis either for the sake of relevance or because the optimisation results were not concluding. Indeed, in [40], the maximum admissible values for G_{GAS}, k_ϕ, $\phi_{k,off}$ and $l_{off,HAM}$ were fixed to ∞, which can not be implemented. The maxima of G_{GAS} and k_ϕ were thus arbitrarily fixed to 100. As for the maximum of $l_{off,HAM}$, it was set to 4 on the basis of the HAM muscle-tendon unit's (MTU) lengths (see 4.1.4). Concerning $\phi_{k,off}$, its maximum value was fixed to 3.142 ($= 180°$) since it corresponds to the threshold above which the VAS is inhibited to prevent knee overextension. The last modification with respect to [40] is the maximum value of θ_{ref} which was changed from 0.11 to 0.7854 ($= 45°$) as the results were not acceptable with an upper limit of 0.11. This high value of 0.7854 was never reached and was thus chosen in order to increase the probability that θ_{ref} converges towards a global minimum rather than a local minimum, while remaining a physically correct upper bound.

The values of the reflex control parameters obtained after optimising are also given in table 4.1.

Table 4.1: Reflex control parameters and their range of acceptable values [40]. The gains G_m and k_{bw} in this table are normalised to $F_{max,m}$ (see 4.1.4) and the body weight (see 4.3). Moreover, the offsets $l_{off,m}$ are shown in fractions of the optimum muscle-tendon unit's (MTU) lengths $l_{opt,m}$ (see 4.1.4).

Parameter	value	min	...	max	Parameter	value	min	...	max
G_{GAS}	2.9393	0.0	...	100.0	ΔS	0.8169	0.14	...	1.0
$S_{0,VAS}$	0.0780	0.047	...	0.71	G_{HAM}	0.6471	0.0	...	0.67
G_{VAS}	1.1958	0.82	...	13.5	G_{GLU}	0.0252	0.0	...	0.52
k_ϕ	58.7735	0.0	...	100.0	G_{HFL}	2.9378	0.17	...	3.0
$\phi_{k,off}$	3.0134	2.71	...	3.142	$l_{off,HFL}$	0.0406	0.0	...	0.67
k_{bw}	1.3378	1.30	...	5.0	G_{HAMHFL}	86.9518	0.0	...	100.0
k_p	2.1470	1.78	...	22.0	$l_{off,HAM}$	0.9683	0.83	...	4.0
θ_{ref}	0.3468	0.017	...	0.6109	k_{lean}	3.0400	1.0	...	5.70
k_d	0.6970	0.10	...	0.75					

4.1.4 Muscle tendon units

Here are explained the main steps allowing to translate the muscle stimulations into muscle forces and then to the torques at the joints.

First, all muscle-tendon units (MTUs) of the implemented neuromuscular model have the same model structure, which is depicted in figure 4.4. This muscle-tendon model is composed of four elements: an active contractile element (CE), a series elasticity (SE), a parallel elasticity (PE) and a buffer elasticity (BE). In normal operation, only the contractile element and the series elasticity form the MTU. The parallel elasticity engages if the CE extends beyond its optimum length ($l_{CE} > l_{opt}$) while the BE prevents the CE from collapsing if the SE is slack ($l_{MTU} - l_{CE} < l_{slack}$) [40]. The values of the optimum length and slack length of each MTU are given in table 4.2 and are retrieved from [40].

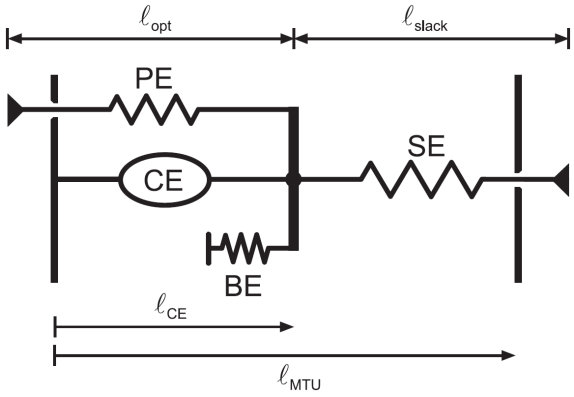

Figure 4.4: Muscle-tendon model [40].

Table 4.2: Individual MTU parameters (in [cm]) [40].

	GAS	VAS	HAM	GLU	HFL
l_{opt}	5	8	10	11	11
l_{slack}	40	23	31	13	10

The MTU's force F_m is defined as $F_m = F_{se} = F_{ce} + F_{pe} - F_{be}$ with F_x the force of the x element [40].

All the detailed calculations allowing to determine F_m will not be covered here but rather the main steps since the implementation of these calculations has been retrieved from the doctoral thesis of Nicolas Van der Noot [46] and has not been modified.

The MTU's force is computed from resolving the inner degree of freedom l_{CE} [40]. This is done by first computing the MTU's length and then by making an integration with Euler method, which computes the value of l_{CE} and its derivative according to a well-defined number of iterations for each time step.

Next, the joint torque τ_m is expressed in terms of the obtained MTU force F_m as $\tau_m = r_m(\phi)F_m$ where the lever r_m is equal to r_0 for the hip and $r_0 \cos(\phi - \phi_{max})$ for the knee [40]. The values of r_0 and ϕ_{max} are given for each joint and each MTU in table 4.3.

Table 4.3: MTU attachment parameters [40].

		knee			hip		
		GAS	VAS	HAM	HAM	GLU	HFL
r_0	[cm]	5	6	5	8	10	10
ϕ_{max}	[deg]	40	15	0	-	-	-

4.2 Mid-level controller

The mid-level controller corresponds to a Simulink file implementing the powertrain designed in the previous chapter (see figure 2.8 page 15) and the transmissions to the legs' joints. This controller takes as inputs the referential torques calculated by the high-level controller as well as the joints' velocities and computes then the torques that are really applied to the joints due to the characteristics (efficiency, dynamics, transmission ratio, etc.) of each component of the powertrain.

However, due to a lack of time, the Simulink file was not adapted and does thus not take into account all components of the dimensioned powertrain. Indeed, as it can be seen in figure 4.5, this file only considers the motor, the gear reducer and the spring (red box), three differentials (green boxes) and four IVTs (blue boxes). To match the powertrain designed in the previous chapter, planetary gears should replace the second stage of differentials and others should be placed after the IVTs to increase their output torque,

and the transmissions to the joints should also be added. Moreover, all the parameters must be tuned as well.

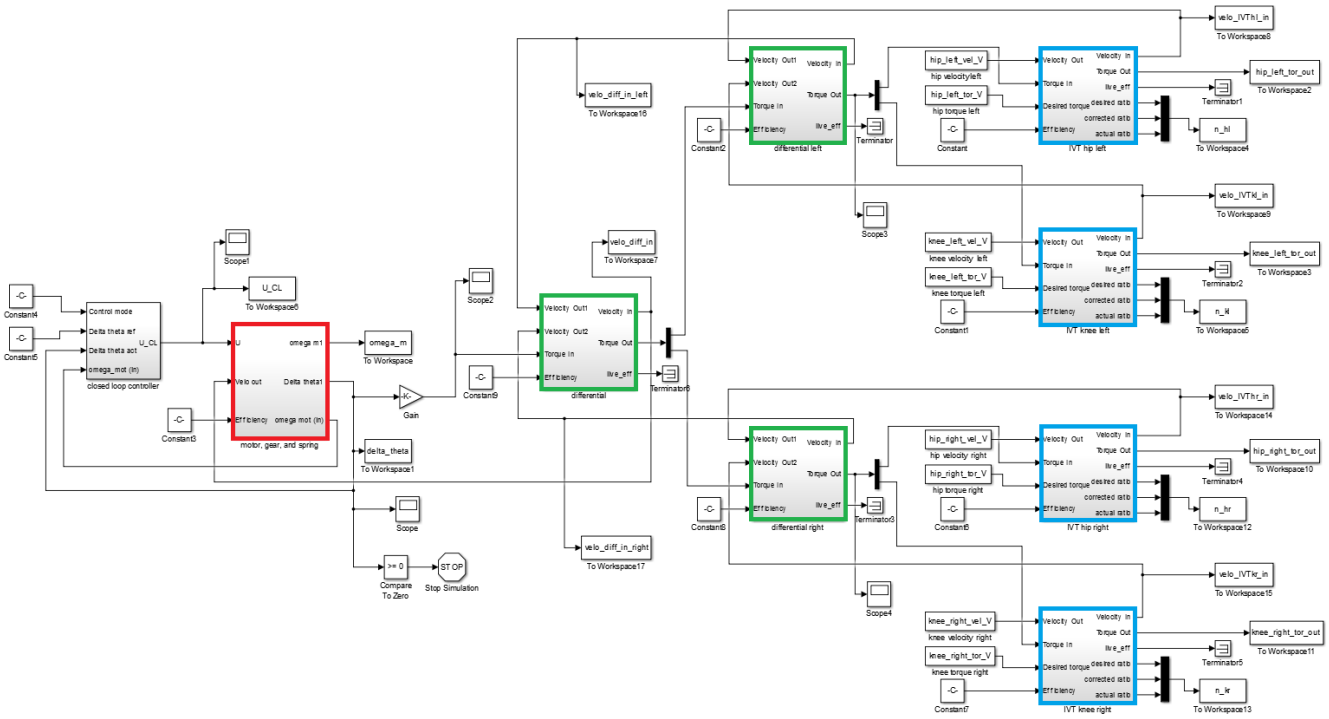

Figure 4.5: Simulink scheme.

4.3 Simulation environment

In this section, the simulation environment is presented. First, the modelling of the robot in Robotran is presented. Then, the ground contact model implemented is described.

4.3.1 Modelling in Robotran

The robot is modelled in Robotran, which is a symbolic software to model and analyse multibody systems [48]. Screenshots of the representation of the robot with the graphical editor of Robotran and of the obtained simulation are given in figure 4.6. As it can be seen in this figure, the robot is modelled by five bodies: one trunk, two thighs and two "calf and foot" sets. Indeed, since the robot has no ankle, preventing thus any motion between its calves and the spheres acting as feet, these two parts are merged into one unique body taking both masses and inertia into account. The properties of each part of the robot are given in table 4.4.

Table 4.4: Robotran parameters.

Trunk			**Thigh**			**Calf**			**Foot**		
Height	[cm]	40	Height	[cm]	25	Height	[cm]	25	Diameter	[cm]	5
Width	[cm]	30	Diameter	[cm]	7.5	Diameter	[cm]	5	Mass	[kg]	0.1
Depth	[cm]	20	Mass	[kg]	2	Mass	[kg]	1			
Mass	[kg]	29									

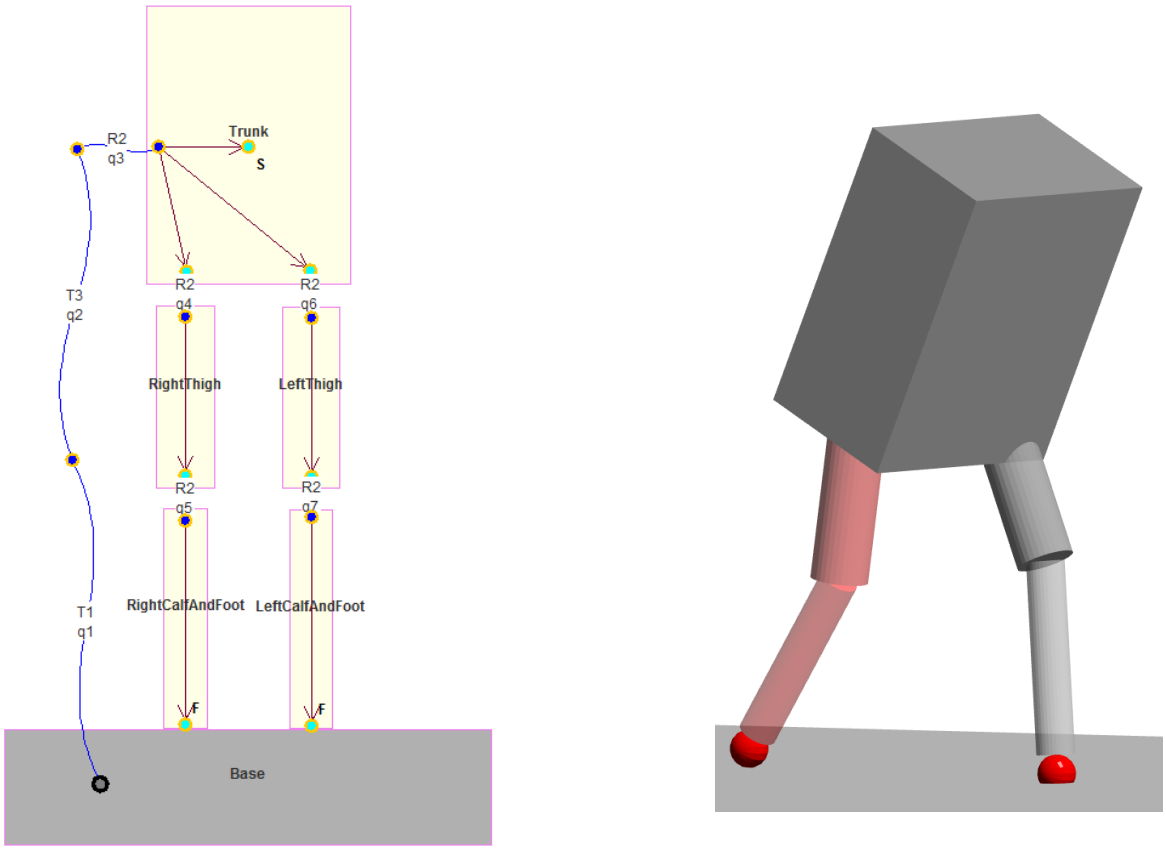

Figure 4.6: Screenshots of the representation of the robot with the graphical editor of Robotran (left) and of the simulation (right).

The masses of the thighs, calves and feet given in table 4.4 have arbitrarily been fixed. The mass of the trunk has however been set by estimating the mass of each of its main constituting elements which are dimensioned in the next chapter. The obtained value for the mass has been rounded up in order to take the mass of the shafts, electrical cables, etc. into account.

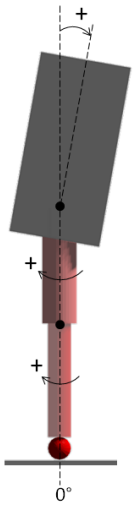

Figure 4.7: Definition of the joints' angles.

Moreover, as required by the specifications (see 3.1 page 17), the robot can solely move in its sagittal plane. Therefore, the trunk is only allowed to move up and down, back and forth and to lean. These three degrees of freedom are ensured by the three joints T3, T1 and R2 respectively (see figure 4.6). Indeed, a T_i or R_i joint corresponds respectively to a prismatic or a revolute joint in the i-direction, with i equal to 1, 2 or 3 for x, y or z, and the x-axis corresponds to the forward direction, the y-axis to the left direction and the z-axis to the upward direction. Besides, only one degree of freedom is allowed for each leg segment, which is guaranteed by a R2 joint.

Given the definition of the robot's inertial frame, the angles of the trunk, the hips and the knees are defined as it can be seen in figure 4.7. The reference for the trunk's angle is the vertical, while the hips' and knees' angles are defined with respect to their parent body. In other terms, the trunk's angle is absolute while the hips' and knees' angles are relative.

4.3.2 Ground contact model

The ground contact model that is implemented differs from what is done in Nicolas Van der Noot's doctoral thesis. The computation of the ground contact forces is divided into the calculation of the normal force and that of the tangential force.

Normal force computation

The normal force F_N is computed by considering the volume of the robot that penetrates into the ground and how quickly it does it. It expresses thus as follows:

$$F_N = K_P \cdot V \cdot \{1.0 + K_D \cdot \dot{V}\}_+$$

where

K_P	is the normal stiffness coefficient $\left[{}^{N}/_{m^3}\right]$
K_D	is the normal damping coefficient $\left[{}^{s}/_{m^3}\right]$
V	is the penetration volume $[m^3]$
$\dot{V}$	is the penetration volume derivative $\left[{}^{m^3}/_{s}\right]$
$\{x\}_+$	is a function returning 0 if x is negative and x otherwise

The values of the parameters K_P and K_D have arbitrarily been fixed to $5.0 \cdot 10^7$ $\left[{}^{N}/_{m^3}\right]$ and 5000 $\left[{}^{s}/_{m^3}\right]$ respectively, by a trial and error approach.

The normal ground contact forces obtained with this model with the simulation will be presented later, in chapter 5 (page 50).

Tangential force computation

The tangential force F_t is calculated on the basis of the normal force as follows:

$$F_t = F_N \cdot \mu_{max} \cdot \tanh(\beta \cdot v)$$

where

μ_{max}	is the maximal value for the friction coefficient [-]
β	is the inner factor of the hyperbolic tangent, $\tanh$, [-]
v	is the norm of the relative tangential speed between the foot and the ground at the contact point $\left[{}^{m}/_{s}\right]$

The values of μ_{max} and β have arbitrarily been fixed at 0.9 and 8.0, respectively. Considering this value of β, the hyperbolic tangent function is represented in figure 4.8 as a function of v. In order to see the impact of β, the hyperbolic tangent is also plotted with a unitary value of this parameter.

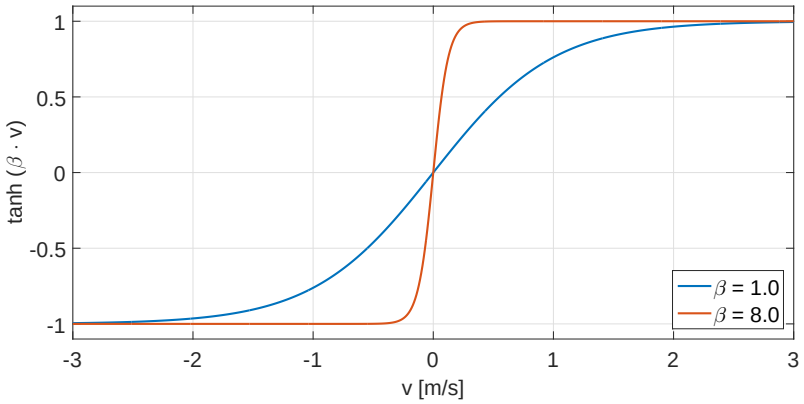

Figure 4.8: Hyperbolic tangent.

Chapter 5

Results of the simulation

This chapter presents the results obtained thanks to the simulation of a straight walking. It is worth noting that a simulation for a circular path was also implemented but due to a lack of time the implementation was not finalised and the parameters were not optimised. First of all, the results will be presented and analysed. Then, they will be compared to human walking data as well as to the results obtained by Nicolas Van der Noot with the humanoid walker COMAN (see its description in chapter 1) in its 2D configuration. The potential divergences between these data will be explained. Finally, possible improvements will be given.

It might beforehand be useful to recall that the frame (x,y,z) is defined as follows (see 4.3): the x-axis corresponds to the forward direction, the y-axis to the left-direction and the z-axis to the upward direction. The joints' angles were also defined in 4.3 according to this frame.

It is also important to mention that all results obtained with the simulation correspond to a walking frequency of about 3.7 [Hz] while the human walking frequency is half this value, i.e. about 2 [Hz] [49]. To counter this, one solution would be to impose the walking frequency as well as the length of the stride to be closer to reality.

5.1 Presentation of the results

In this first section, all quantities that are required for the design and for the control of the robot are presented. More precisely, the variables that will be analysed here are the position of the centre of mass of the robot's trunk, its lean angle, the joints' angles, velocities, torques and powers and finally, the normal ground reaction forces.

The evolution of each of these quantities will be given during half of the simulation time, i.e. 15 [s], since the second half does not bring any additional information. Indeed, as can be seen in the figures below, several seconds are necessary for the robot to stabilise and it enters then a cyclic locomotion. In addition to these 15 [s], each quantity is also represented during only one gait cycle whose beginning is defined by the contact initiation between the ground and the right leg. This cycle is represented in figure 5.1 where the stance and swing phases are defined for the right leg, coloured in red. It is worth repeating that a leg is in stance if it touches the ground and in swing otherwise and that a robot is in double support when both its legs are in contact with the ground and in single support if only one leg touches the ground. In each figure of this section representing the evolution of one quantity during one gait cycle, a grey vertical line is drawn to indicate the transition between the stance and swing phases of the right leg corresponding to about 57% of the cycle.

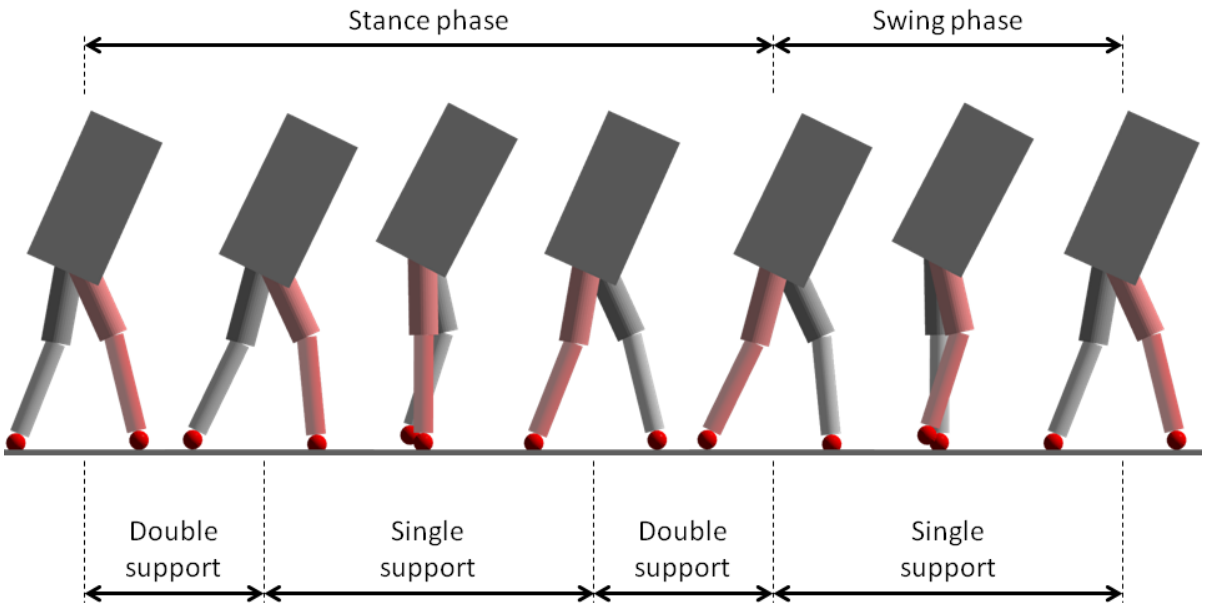

Figure 5.1: Gait cycle. The stance and swing phases are defined for the right leg (coloured in red).

5.1.1 Centre of mass and lean angle

First, the evolution of the vertical position of the centre of mass of the trunk and of its lean angle are given in figures 5.2 and 5.3, respectively.

Initially, to help the robot to start walking, its trunk's lean angle is set to 10 [deg] (see figure 5.3). This angle value has been set before the optimisation of the parameters and was not changed since given that both legs are straight and aligned at the beginning. Indeed, with this initial leg configuration, increasing the lean angle would lead to a fall of the robot. Apart from being straight initially, both legs are not in contact with the ground since the initial value for the height of the centre of mass does not take the lean angle into account. The robot's feet are thus about 2 [mm] above the ground.

Therefore, one can see in figure 5.2 that the vertical position of the centre of mass first decreases until oscillating around its steady-state value, i.e. until a cyclic-locomotion is attained.

During the double support phase at the beginning of the gait cycle (see figure 5.1), the vertical position of the trunk's centre of mass decreases as the right foot slightly sinks into the ground and as the right leg bends. Then the position increases because of the ground reaction force that prevents the foot to sink more into the ground and because the right leg stretches. Finally, it drops back since the right leg bends again, before the left leg touches the ground. The stance leg becomes now the left one and the same steps repeats until the right leg touches the ground.

The variations of the position of the centre of mass are of $\pm$ 0.014 [m] with respect to its mean value, which is of 0.648 [m].

Concerning the trunk's lean angle, its evolution is given in figure 5.3 where one can see that this angle increases progressively from 10 [deg] until a mean value of about 26 [deg], around which it oscillates of $\pm$ 1.88 [deg] during the walk. This quite significant value for the angle can be justified in two ways. On the one hand, this could be due to the high walking frequency of the robot. On the other hand, this could be a consequence of the lack of ankle for the propulsion, requiring thus that the robot leans more to unbalance

in order to walk.

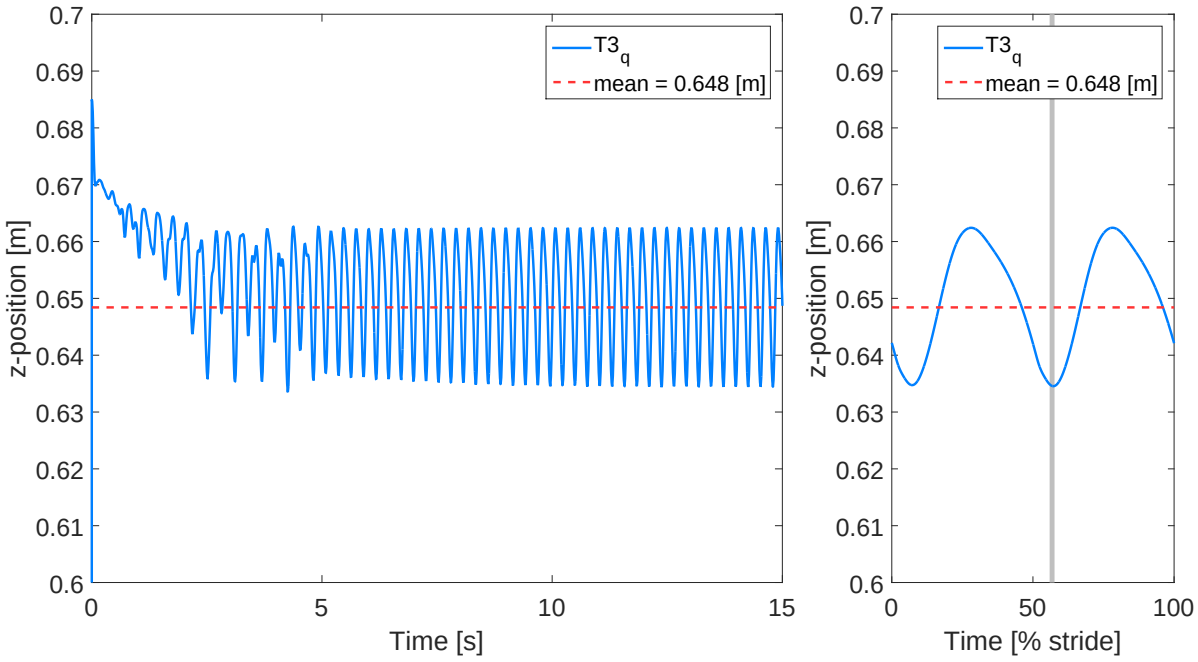

Figure 5.2: Evolution of the vertical position of the trunk's centre of mass during the first half of the simulation time (left) and during a gait cycle (right).

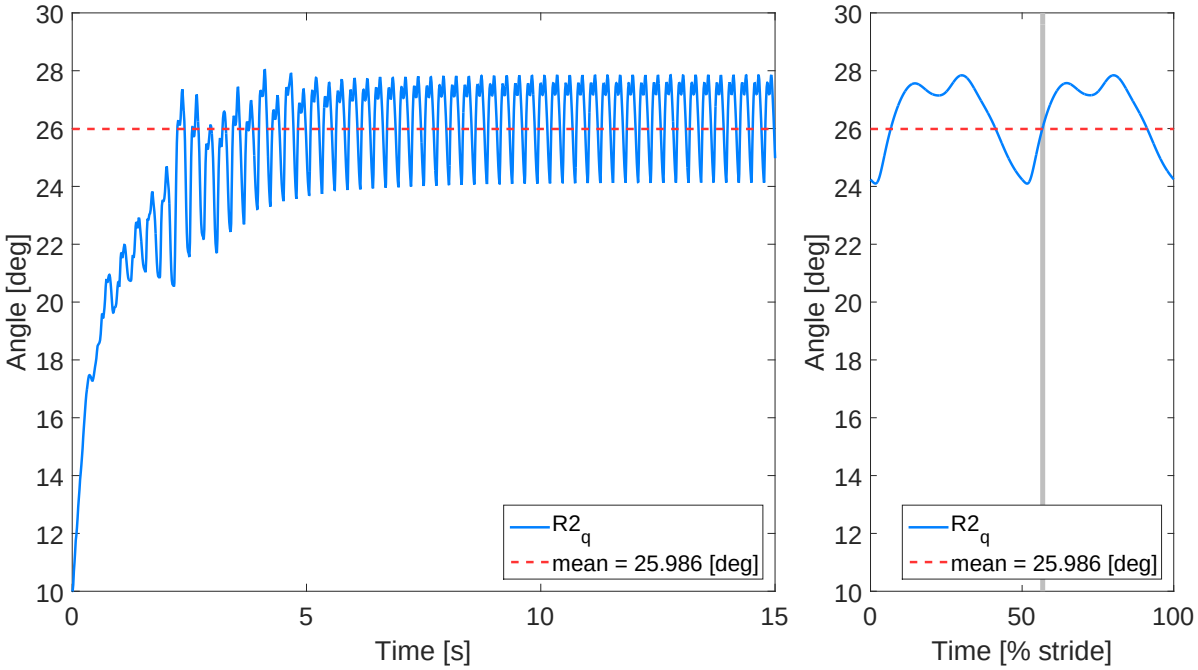

Figure 5.3: Evolution of the trunk's lean angle.

As for the centre of mass, it is possible to notice in the figure 5.3 at the right that the evolution of the trunk's lean angle can be divided into two periods since the walk is symmetric between both legs. At the beginning of these periods, the angle keeps decreasing as the foot of the stance leg penetrates into the ground. Then, because of the ground reaction and of the bending of this stance leg, the robot leans more

forward. After, the crook of the curve corresponds to the swing of the other leg, with the lowest point matching the moment at which the two thighs are aligned, i.e. at mid-stance. Finally, the angle decreases until the swing leg touches the ground.

5.1.2 Joints' angles, velocities, torques and powers

In this part, the joints' angles, velocities, torques and powers will only be given for the right leg since both legs are symmetric. Therefore the results of the left leg being equivalent to those of the right leg will not bring any new information.

The joints' angles of the right leg are given in figure 5.4. As expected, the hip's angle always remains negative while that of the knee is positive all the time except at mid-stance where the knee is slightly in overextension (from 2 [deg]). The general shape of the hip's angle curve is an increase during the stance phase followed by a decrease during the swing phase. There are two bumps in this graph corresponding to the impact with the ground and to the mid-stance. Concerning the knee's angle, there are more variations in the curve. Indeed, when the ground contact is initiated, the leg first bends to damp the shock then stretches in order to allow the swing of the other leg. After reaching the mid-stance point, the stance leg bends again until the swing leg touches the ground. Finally, during the swing phase the leg bends to avoid touching the soil and extends before reaching the ground.

In steady-state regime, the hip's angle varies between -53 [deg] and -10 [deg] while the knee's angle is comprised between 38 [deg] and -2 [deg].

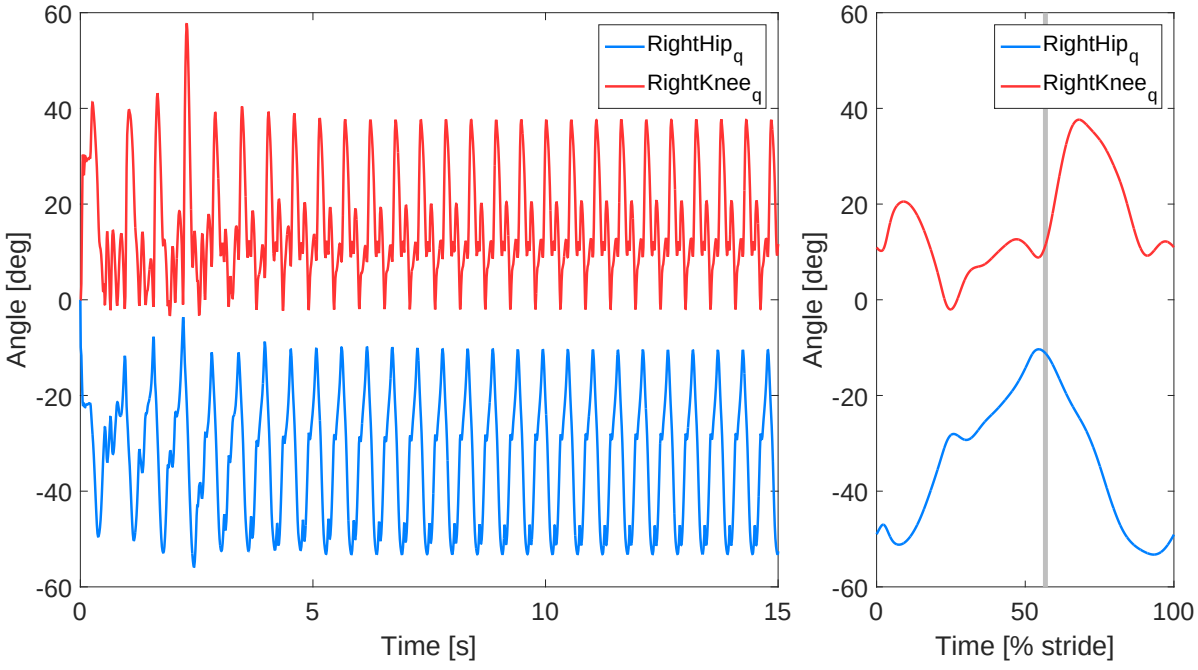

Figure 5.4: Evolution of the right leg's joints' angles.

The evolution of the joints' velocities are given in figure 5.5. It is interesting to see that at the beginning of the simulation the peak values are much higher than in steady-state because the joints start at 0 [deg] and several seconds are needed to enter a cyclic locomotion. It can also be noticed that during steady state the velocity of the knee reaches about 650 $[^{deg}/_{s}]$ while that of the hip is of about 380 $[^{deg}/_{s}]$ at most.

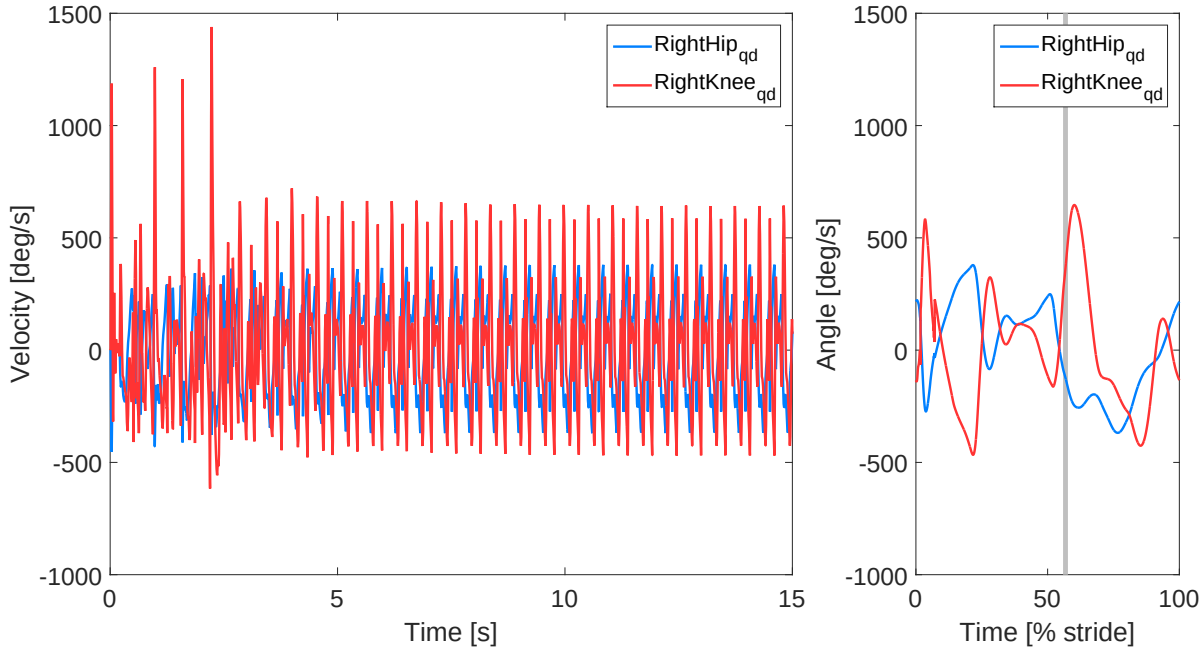

Figure 5.5: Evolution of the right leg's joints' velocities.

After, the joints' torques are represented in figure 5.6. As can be seen in the figure 5.6 at the right, there is a torque peak at the hip corresponding to the initiation of the contact with the ground. The minimal and maximal values of the hip's torque in steady state are of -20 [Nm] and 76 [Nm] respectively while those of the knee are of -18 [Nm] and 17 [Nm]. It is however important to note that the knee's joint reaches higher torque values before the steady state is attained. The maximal reached value (50 [Nm]) will be that considered in the dimensioning (see next chapter) since it corresponds to the worst case.

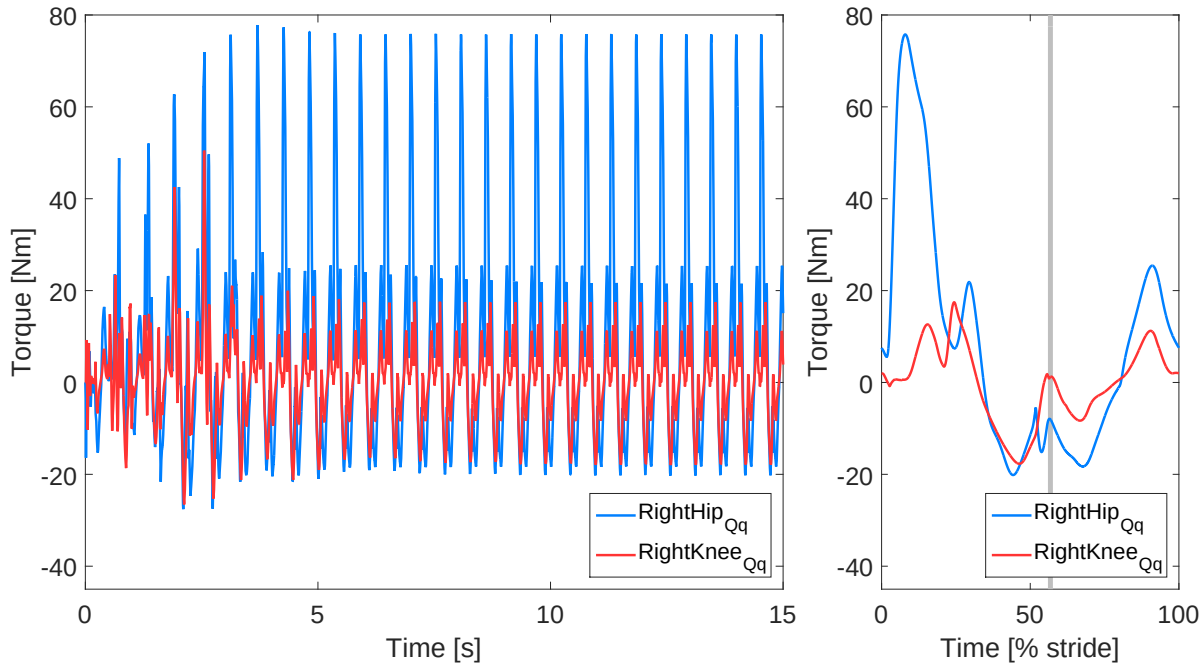

Figure 5.6: Evolution of the right leg's joints' torques.

Finally, the power required by the joints is depicted in figure 5.7. This power was computed by multi-

plying the joint's velocities by their respective torques and is normalised to the mass of the robot, which is of 35.2 [kg] (see 4.3). Because of the high torque peak, a high power is required by the hip's joint. During the steady state, the maximum power values of the hip and the knee are of about 7.35 $[^{W}/_{kg}]$ and 2.21 $[^{W}/_{kg}]$ respectively, in terms of absolute value.

The energy during one gait cycle can be retrieved from the power by integrating this latter. The value obtained for the hip is positive and is of about 0.336 $[^{J}/_{kg}]$ whereas that of the knee is negative and is equal to -0.146 $[^{J}/_{kg}]$. The total energy of one leg during one gait cycle and thus that of the robot are then of 0.190 $[^{J}/_{kg}]$ and 0.380 $[^{J}/_{kg}]$ respectively. Because the energy is positive, it means that power is dissipated in average on a gait cycle. Power must then be given to the robot in order to walk, which is consistent since the robot is active.

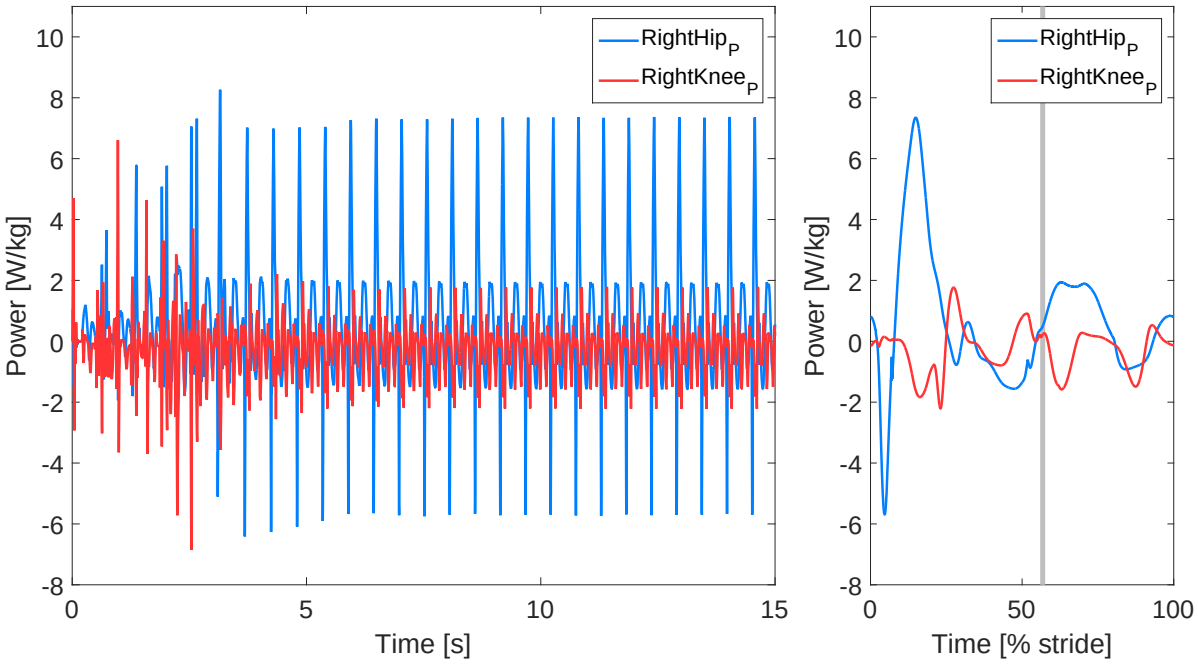

Figure 5.7: Evolution of the right leg's joints' powers.

5.1.3 Ground reaction forces

Here are shown the normal ground reaction forces that are necessary in the control to determine whether a leg is in stance or not. The forces of both legs are given in figure 5.8, as well as the mean value of these forces and the weight of the robot.

In the figure 5.8 at the right, one can confirm the symmetry between the two legs since their force profiles are identical but shifted from one period corresponding to 50% of the stride. Moreover, there are two major peaks for each leg corresponding to the impact with the ground and to the impulsion before the foot take off. One can notice that after the first peak, there is a significant drop immediately followed by an important increase. This "peak split" is probably due to the ground contact model whose parameters are such that the damping is too significant.

Moreover, a large time step is a problem since the penetration volume could rapidly increase from one time step to the following generating thus a large reaction force, which does not correspond to reality.

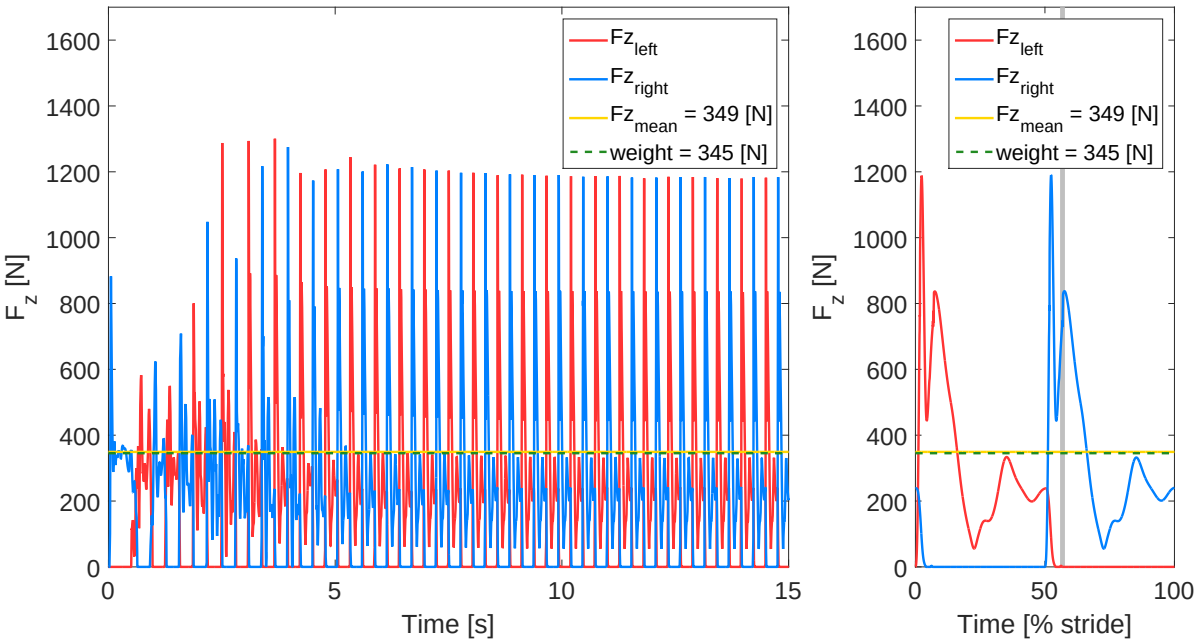

Figure 5.8: Evolution of the normal ground contact forces.

Besides, the average of the normal force over the gait cycle is nearly identical to the weight of the robot (349 [N] vs 345 [N]). This slight difference is due to the modelling since these values should be equal by writing the sum of the forces in the dynamical case:

$$\Sigma F = m\,a \Rightarrow F_N - P = m\,a$$

with F_N the normal ground reaction force, P the weight of the robot, m the mass of the robot and a the vertical acceleration of the centre of mass.

By taking the mean of this equation, it results that:

$$\bar{F_N} - P = 0$$

since $\bar{P} = P$ and $\bar{a} = 0$ because the weight is constant and the robot does not sink into the ground or rise into the air.

5.2 Comparison with human walking data

In this section, some of the results presented above will be compared to human walking data, retrieved from a study of David A. Winter [33]. The quantities that will be analysed here are the joints' angles, torques and powers as well as the normal ground reaction forces.

The robot of this master thesis presents two main differences with a human: it has no ankle and its walking frequency is almost the double. It will therefore be interesting to take these two points into account in the comparison.

First, the evolutions of the right legs' joints' angles of the robot and of a human during a gait cycle are given in figure 5.9. In this figure, the hip's curve profiles are very similar in both cases but there is an offset of about 25 [deg] between both. This is due to the trunk's lean angle that is much higher for the robot (around 26 [deg]) than for a human (around 5 to 10 [deg][50]) since this angle is defined relatively

to the trunk. Concerning the evolution of the knee's angle, the general shape of the two curves is similar but there is one significant difference: the peak is higher for the human, meaning that the leg bends more. This corresponds to the swing phase and can thus be explained by the fact that to ensure ground clearance the human has to bend more its leg than the robot since it has feet that can not touch the ground.

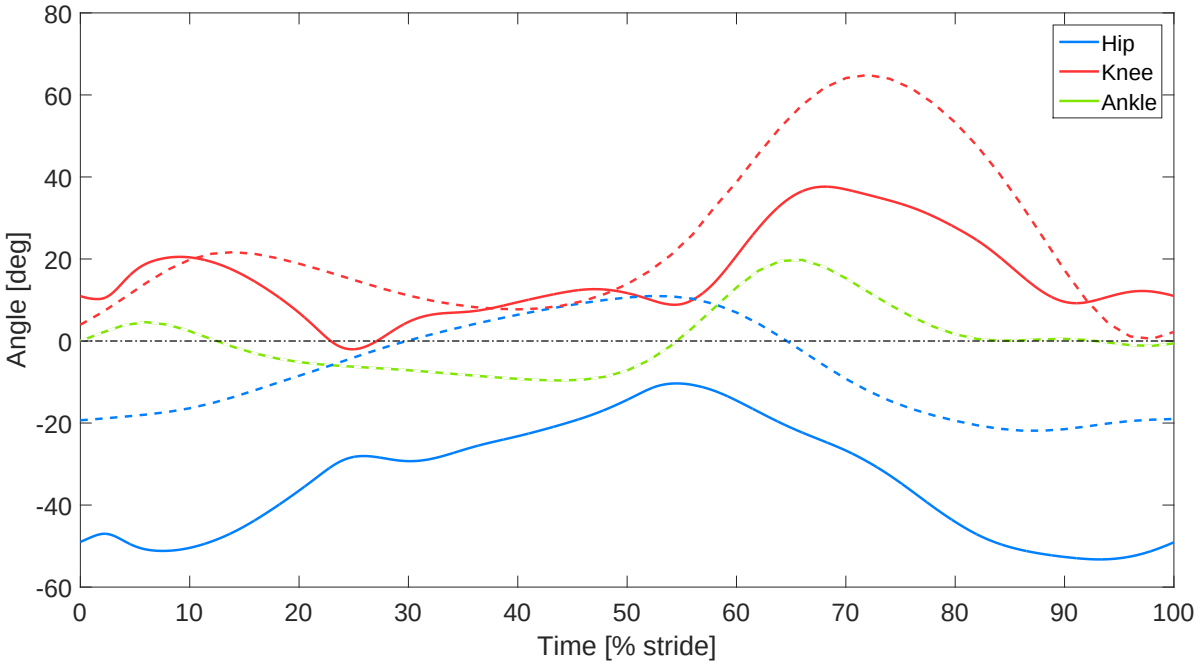

Figure 5.9: Evolution of the leg's joints' angles of the robot (solid lines) and of a human [33] (dashed lines).

Then, the joints' torques are represented in figure 5.10. The main difference between the humanoid walker data and the human data comes from the lack of ankle. Indeed, a large torque is required by the ankle to provide an impulsion at take off. As the robot has no ankle, this results in a large hip torque from the leg that just became the stance leg. In other words, the peak torque of the right hip allows the swing of the left leg and inversely. Aside from this peak, the hip's and knee's curves are quite similar.

Next, the joints' powers are given in figure 5.11 and are normalised to the mass. The lack of ankle translates into a high power peak since it is proportional to the torque by definition but also into larger power values for the hip and the knee over the entire cycle.

Finally, the normal ground reaction forces are depicted in figure 5.12. Although the order of magnitude of the first peak is quite different between a human and the robot of this master thesis, one can still notice that both curves have two major peaks. It is also possible to see that the double support phase is much shorter for the robot than for the human. This is certainly due to the lack of ankle.

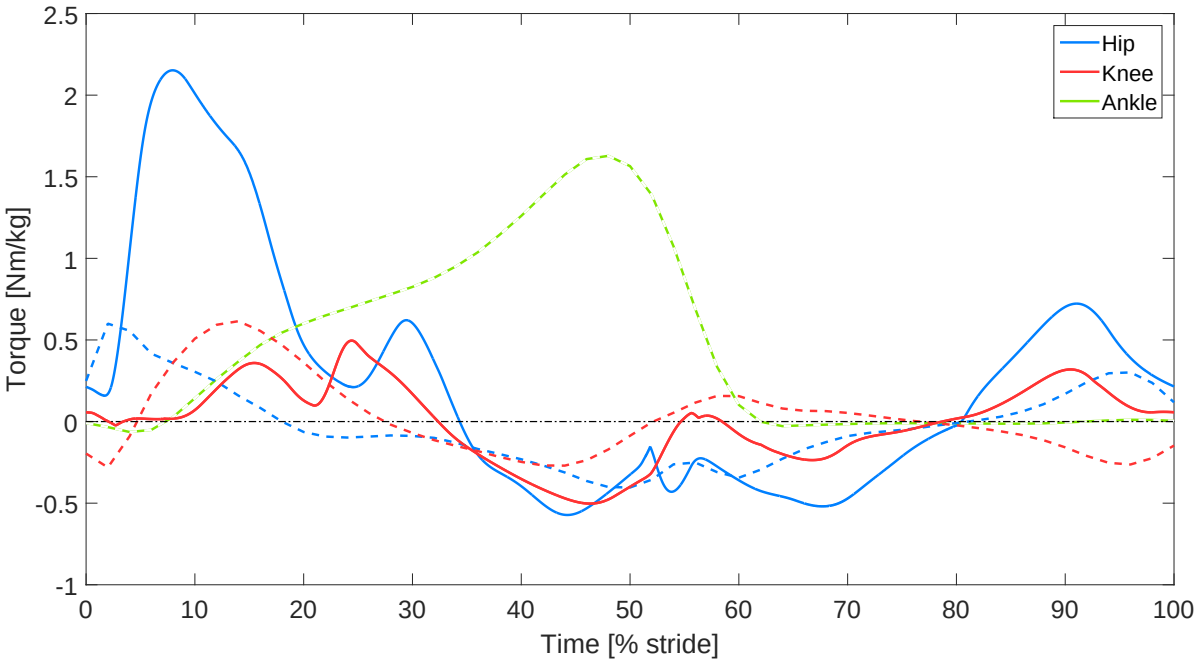

Figure 5.10: Evolution of the leg's joints' torques of the robot (solid lines) and of a human [33] (dashed lines).

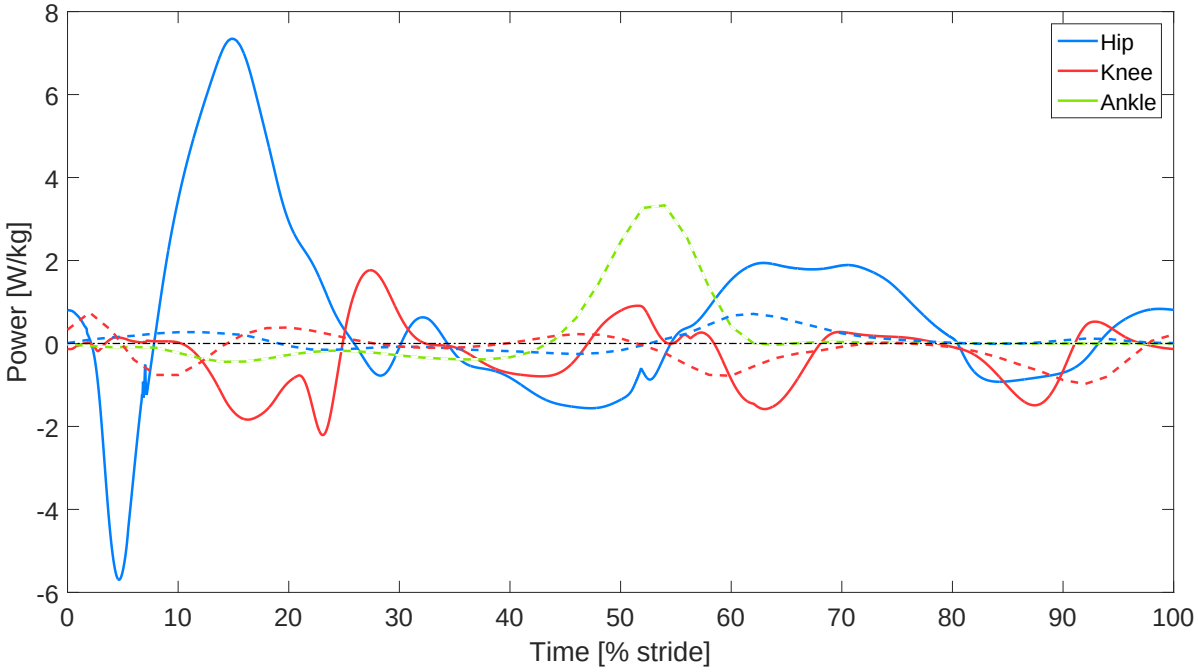

Figure 5.11: Evolution of the leg's joints' powers of the robot (solid lines) and of a human [33] (dashed lines).

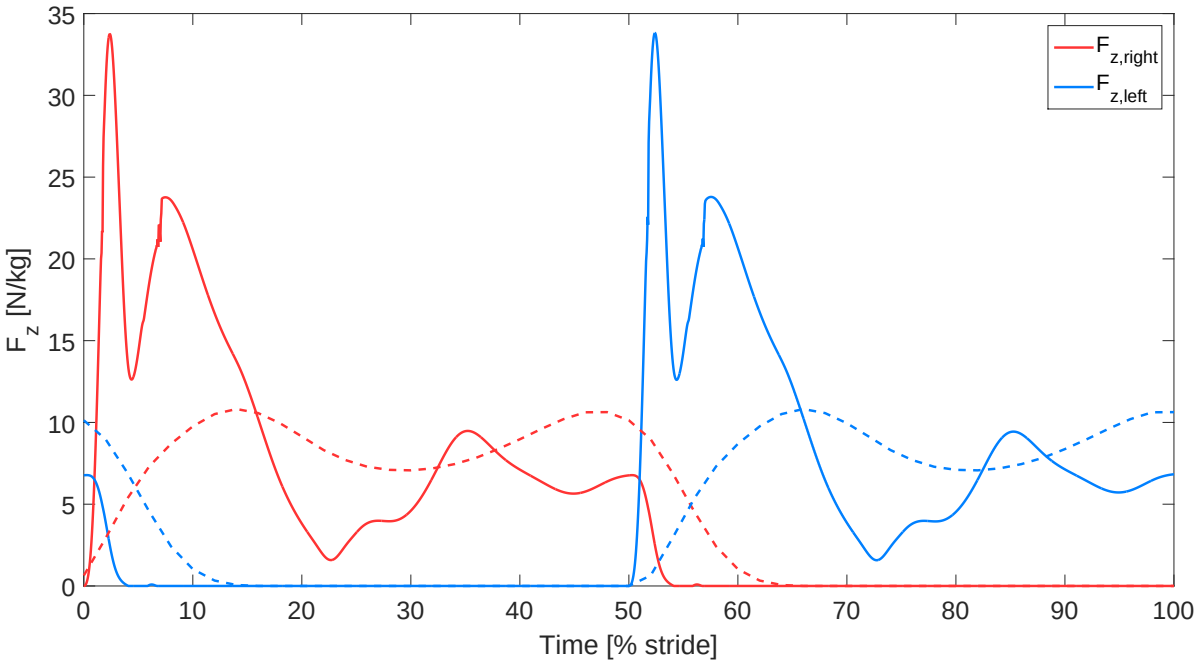

Figure 5.12: Evolution of the normal ground contact forces of the robot (solid lines) and of a human [33] (dashed lines).

5.3 Comparison with COMAN data

In this last section, the results will be compared to COMAN data that are retrieved from the doctoral thesis of Nicolas Van der Noot [51]. Although COMAN was presented as a 3D bipedal robot in the first chapter of this master thesis, the data used here for the comparison correspond to a 2D version of this robot.

The quantities that will be compared are the robot's trunk's lean angle, the joints' angles, torques and powers and the normal ground reaction forces.

Moreover, the walking frequency of COMAN is similar to that of a human, since it is equal to about 1.6 [Hz].

5.3.1 Lean angle

First, the lean angle is represented in figure 5.13. In both cases, two equal periods can be distinguished corresponding to the two legs. However, there are several differences. First, the mean value is much lower for COMAN (about 10 [deg]) than for the robot of this master thesis (about 26 [deg]). This is certainly due to the fact that COMAN has ankles, allowing him to propel itself forward. Moreover, the variations of the trunk's lean angle around these values are higher for COMAN (+5 [deg] and -5.6 [deg] at most) than for the designed humanoid walker ($\pm$1.88 [deg]).

5.3.2 Joints' angles, torques and powers

Here will be compared the joints' angles, torques and powers.

First, the evolution of the joints' angles are given in figure 5.14. The general shapes of the hip's curves are similar but shifted. Since the hip's angle is defined relatively to the trunk, this shift can be explained by the fact that the trunk's angle is higher for the robot of this master thesis than for COMAN. The knee

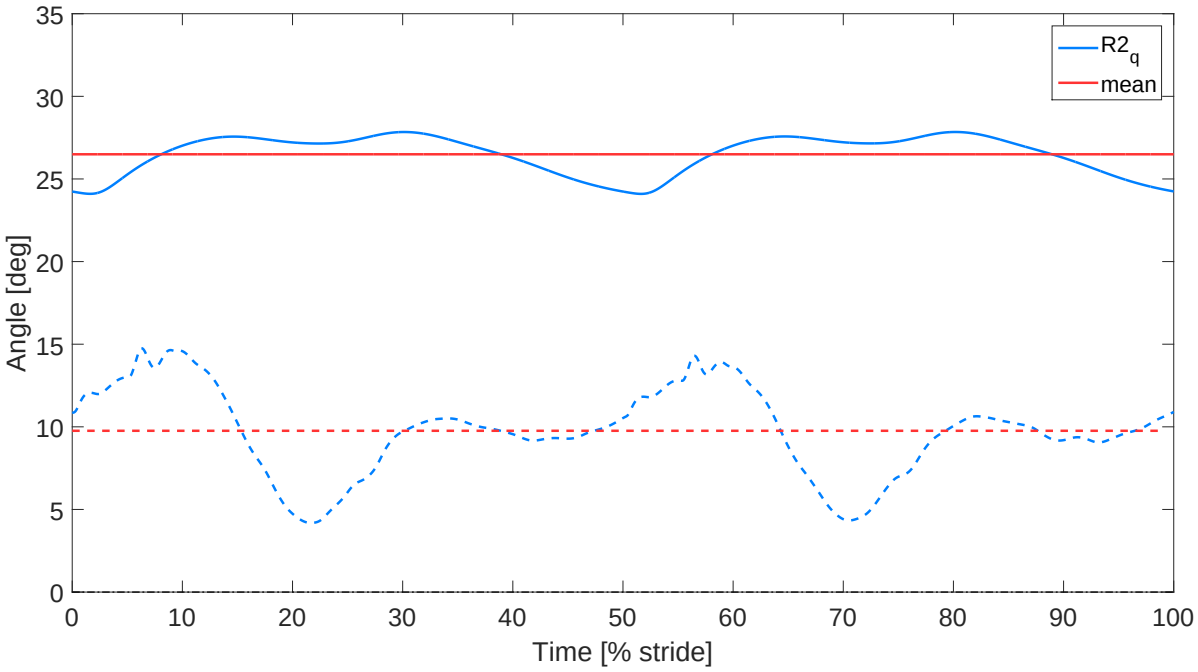

Figure 5.13: Evolution of the trunk's lean angle of the robot (solid lines) and of COMAN [51] (dashed lines).

curve seems however to be influenced by the lack of ankle. Indeed, at the beginning of the gait cycle the ankle's angle corresponds to the contact of the feet with the ground and more precisely to the heel-strike until the foot is flat. As the robot of this thesis has no feet, this contact initiation translates into a bending of the knee. Then, as explained in the comparison with human data, the robot needs to bend less its leg during the swing phase since it has no feet.

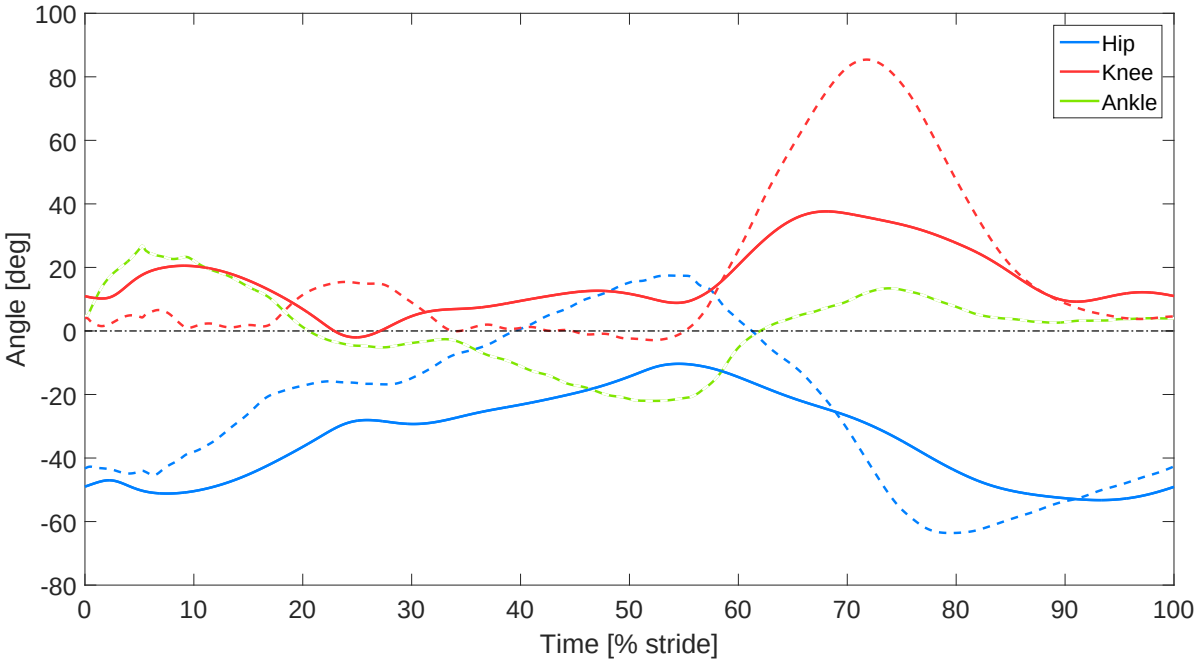

Figure 5.14: Evolution of the right leg's joints' angle of the robot (solid lines) and of COMAN [51] (dashed lines).

Next, the joint's torques are shown in figure 5.15. Such as presented in the comparison with human data, the hip's peak torque at the start of the gait cycle is due to the lack of ankle and allows the left leg to swing. Although it should be noted that the hip's torque at the beginning of the gait cycle is also quite significant.

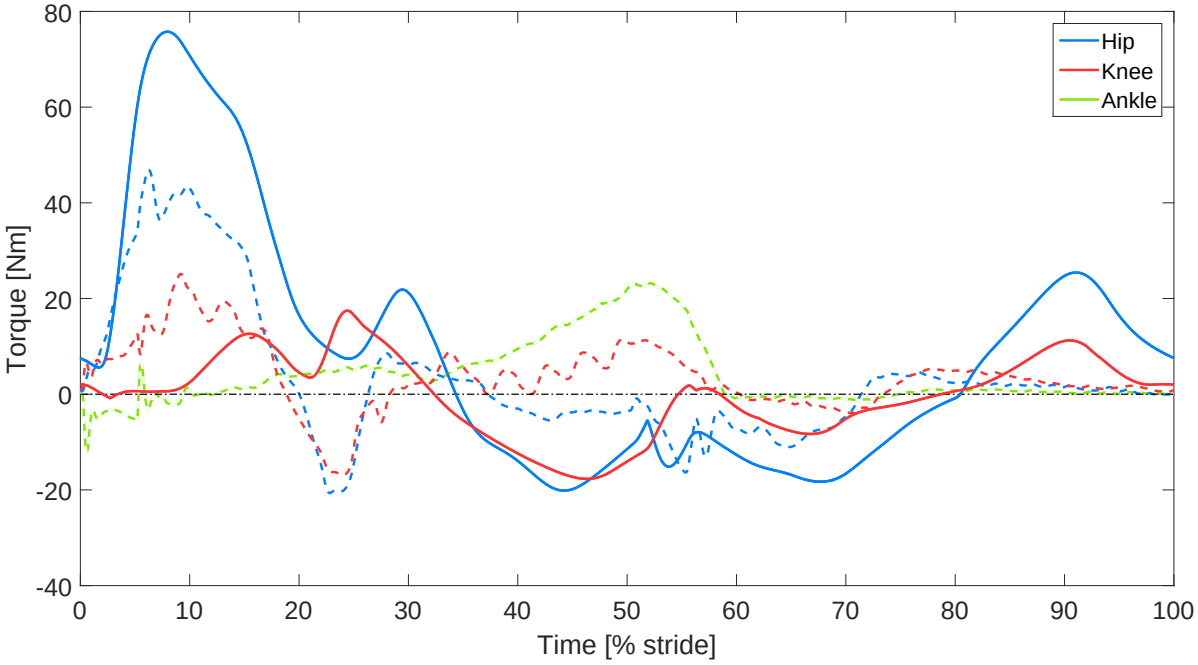

Figure 5.15: Evolution of the right leg's joints' torques of the robot (solid lines) and of COMAN [51] (dashed lines).

Then, the powers of the leg's joints are represented in figure 5.16. The results for the hip are quite similar since both have a high torque at the start of the cycle. Some divergences are noticeable concerning the knee curves which are probably due to the lack of ankle.

The energy required by each hip, knee and ankle of COMAN during one cycle is then computed and is of 0.689 [$^{J}/_{kg}$], -0.278 [$^{J}/_{kg}$] and -0.234 [$^{J}/_{kg}$]. Over one cycle, the total energy of one leg is positive and is equal to 0.177 [$^{J}/_{kg}$], which is similar to what is obtained for the robot of this master thesis.

5.3.3 Ground reaction forces

Finally, the normal ground reaction forces are given in figure 5.17. Peak forces of COMAN and of the robot of this thesis are of the same order of magnitude but it should be noted that the forces of COMAN are saturated at a value of 1000 [N]. There is also a shorter double support phase for the robot than for COMAN that can be justified by the lack of ankle.

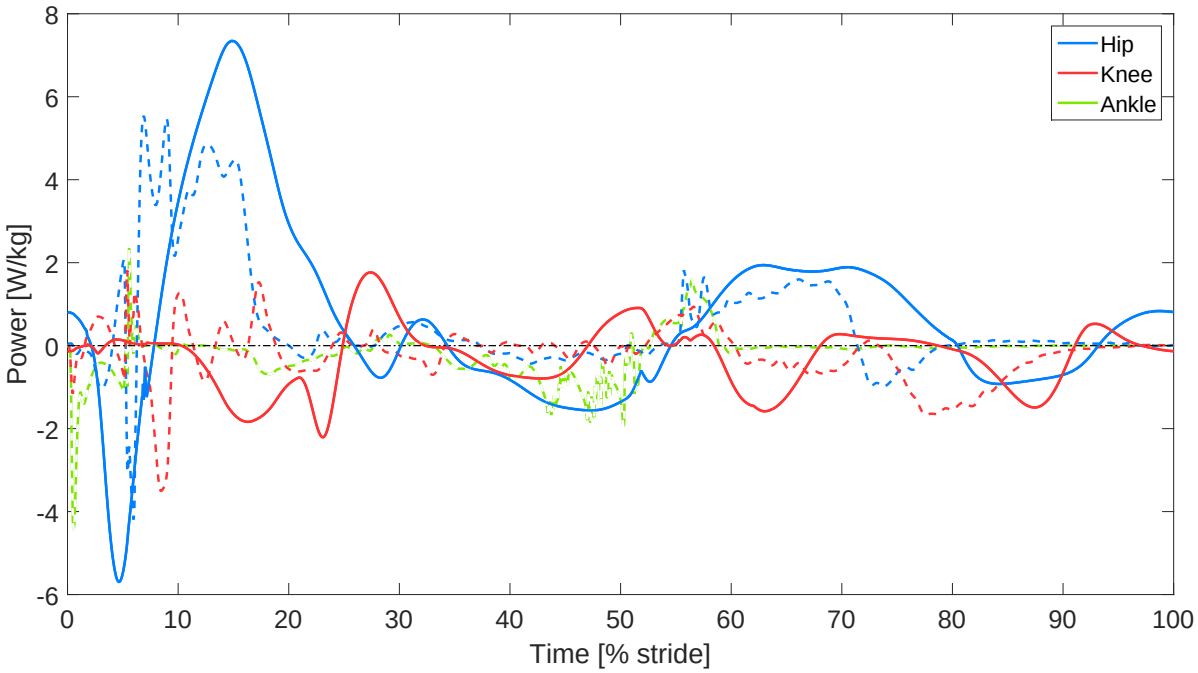

Figure 5.16: Evolution of the right leg's joints' powers of the robot (solid lines) and of COMAN [51] (dashed lines).

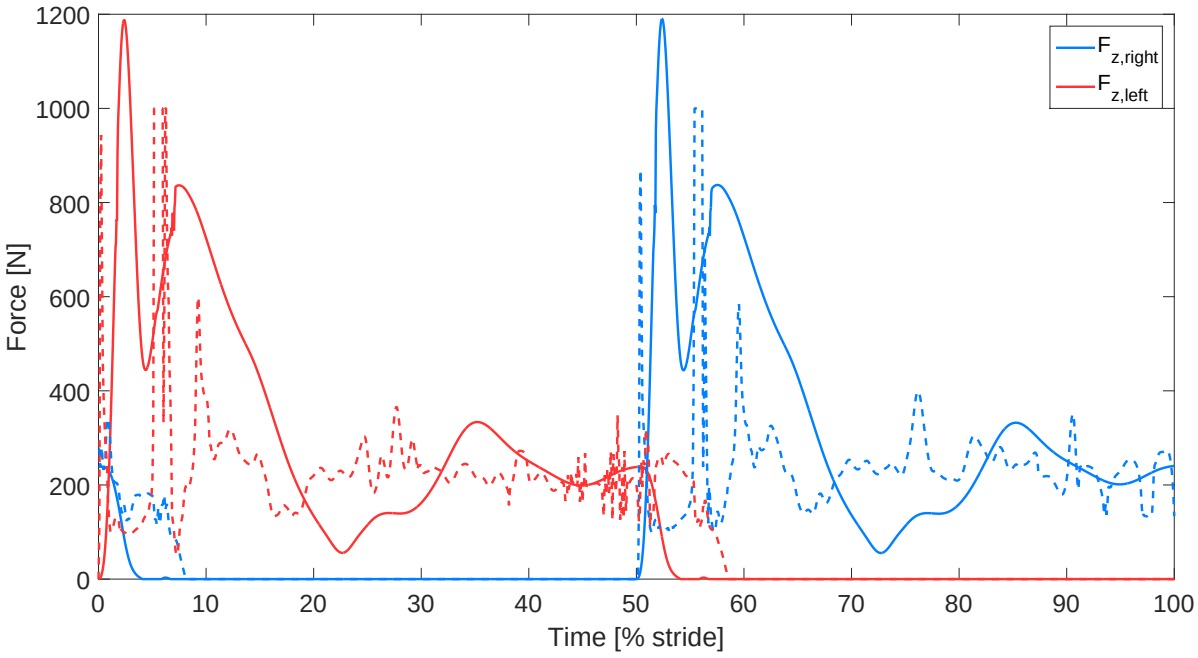

Figure 5.17: Evolution of the normal ground reaction forces of the robot (solid lines) and of COMAN [51] (dashed lines).

Chapter 6

Mechanical dimensioning of the powertrain

This chapter focuses on a pre-dimensioning of the main elements of the powertrain described in the chapter about the mechanical design (chapter 3) to respect the required torques at the different joints. First, the IVTs will be dimensioned, then the PGs' transmission ratio, followed by the mechanical differentials, the torsion spring and finally the motors. This chapter will be concluded by presenting a further development that could be done.

6.1 IVTs dimensioning

This development starts by dimensioning the IVTs. This dimensioning is highly inspired from a non-published technical report of Christophe Everarts with the MIT [52] from 2014.

At first, a general approach describes how the elements in the IVT are dimensioned. Afterwards, a force analysis explains the limits reachable by the components because of the Hertzian stresses. Finally the equations ruling the torque transmission in the IVT are detailed.

At each step, the results of all cited points are summarised in form of tables or graphs for the two different IVTs dimensioned in this master thesis: one for the hip and one for the knee.

6.1.1 CVTs geometrical dimensioning

The CVTs' maximum transmission ratio is restricted due to geometrical constraints on the cone-shaped planets, or by the Hertzian stresses present in the contact point between the different elements. The CVTs are dimensioned as big as possible in function of the available space while respecting stresses constraints. The method used for the dimensioning starts by determining the ring radius and then by expressing all the other dimensions in function of this value. The presented design has four cone-shaped planets in the CVT to increase the admissible torque.

The transmission ratio of the CVT is expressed in the section 2.2 and can be reorganised as:

$$\tau_{CVT} = 1 + \frac{R_7\, R_6}{R_5\, R_{6'}} = \frac{R_c}{R_s} + 1$$

with R_c the ratio between the ring and the planets radii $R_c = \frac{R_7}{R_{6'}}$ and R_s the ratio between the sun and the planets radii $R_s = \frac{R_5}{R_6}$. These ratios are restricted by geometric constraints.

For the ring/cone ratio R_c:

- the minimum value is 2. This boundary determining the maximum radius of the cone-shaped planets is restricted to this value due to the number of planets in the design. Indeed, if four cones are placed in the CVT, the maximal value for the bigger radius of the cone is half of the ring radius. This allows to keep a good symmetry and a good force distribution in the mechanism.
- the maximum value is 5. It was already explained that it was impossible to have a cone radius equal to zero. Due to Hertzian stresses between the rollers and the cones, the smallest radius of the cone must approximately be the same as the roller. This values optimises the geometric dimensions of the design.

This gives the maximal and minimal cones radii: $R_{6',max} = \frac{R_7}{2}$ and $R_{6',min} = \frac{R_7}{5}$ respectively.

For the sun/planets ratio R_s it was assumed in the source [52] that it was equal to 1 to reduce the size of the mechanism. In practice, this was not true due to geometric constraints.

The position of the contact point between the cones and the sun is at a distance from the cone axis arbitrarily chosen in order to have a sufficiently large width of material behind the contact point to resist the constraints. This distance corresponds to the radius R_6 and is expressed in function of the ring radius through the maximum and minimum cone radii.

$$R_6 = R_{6',max} - \frac{R_{6',min}}{2} = \frac{4}{10} R_7$$

This expression is arbitrarily chosen to correpond to the value from the design of Christophe Everarts [52] where the origin was not explained in details.

With this value, a simple trigonometric calculation allows to find the sun radius expression:

$$R_5 = R_7 - \frac{R_{6',max} + R_6}{\sqrt{2}} = \frac{10\sqrt{2} - 9}{10\sqrt{2}} R_7 \approx 0.3636\, R_7$$

This gives a value for R_s of 0.909. This change has an impact on the range of transmission ratio of the CVT. If in the paper of Christophe Everarts the CVT is described with a range value of $[3; 6]$, the CVT described with this new value of R_s gives a range of $[3.2; 6.5]$. This impacts the dimensioning of the IVT with an error on the shift operated by the PG in the next part. In the dimensioning presented here, it was chosen to adapt the value of R_s in order to keep the dimensions of the prototype built by Christophe Everarts as reference values.

The last dimension to express is the curvature radius on the edge of the dome-shaped sun (noted $R_{5'}$). This value is critical in the Hertzian stresses study, limiting the admissible force in the contact sun/cones. Again, an equation was written to correspond to the values arbitrarily chosen by Christophe Everarts. Verified a posteriori, its expression is:

$$R_{5'} = \frac{3}{4} R_{6',min} = \frac{3}{20} R_7$$

and allows to respect the Hertzian constraints with a certain security margin in the different tested cases.

This concludes the dimensioning of the CVT. This is important to note that, to this date, the methodology is not well-established but remains however logical. The curvature radius $R_{5'}$ may be dimensioned with Hertzian theory. The ratio R_s may be optimised to maximise the transmissible torque while respecting failure dimensioning. Those are examples for later improvements.

The two CVTs dimensioned for this master thesis are a bit larger than the prototype built at the UCL. The main reason was to reduce the cost of fabrication. Indeed, the tolerances imposed in the small design of the IVT induce an expensive prototyping. Making the device larger would lower the cost. A second reason was because the first simulation of the robot had much higher torques required at the joints, and it was then obvious to enlarge the IVT.

The choice of CVT ring radius R_7 for the hip joints and for the knee joints are respectively 40.0 $[mm]$ and 36.0 $[mm]$. The other dimensions are summarised in the table 6.1.

Table 6.1: CVTs geometrical dimensioning: summary of the elements' radius in the CVT.

Description	Symbol	Hip CVT	Knee CVT
CVT ring radius $[mm]$	R_7	40.0	36.0
CVT cone radius range $[mm]$	$R_{6'}$	[8.0 ; 20.0]	[7.2 ; 18.0]
CVT cone radius at the contact point with sun $[mm]$	R_6	16.0	14.4
CVT sun radius at the contact point with cones $[mm]$	R_5	14.5	13.0
CVT roller radius $[mm]$	$R_{7'}$	8.0	7.2
CVT sun curvature radius $[mm]$	$R_{5'}$	6.0	5.4

6.1.2 PGs geometrical dimensioning

In the second chapter it was explained that the PG was used to shift the CVT transmission ratio in order to have negative values and therefore creating an IVT. In the designed configuration, the IVT transmission ratio is expressed as:

$$\tau_{IVT} = \frac{\tau_{CVT} - 1}{\tau_{PG}} + 1$$

If the transmission ratio of the CVT is replaced by its expression containing the radius ratio introduced above, this equation becomes:

$$\tau_{IVT} = \frac{R_c}{R_s\,\tau_{PG}} + 1$$

The purpose of the PG dimensioning is to use this expression to compute τ_{PG} that allows to have the maximum and minimum desired ratio of the IVT.

This is performed by computing the value γ, the ratio between the maximum and minimum torque required at the joint. This ratio is equivalent to the ratio between the maximum and minimum transmission ratios of the IVT.

$$\gamma = \frac{T_{max}}{T_{min}} = \frac{\tau_{IVT,max}}{\tau_{IVT,min}}$$

Then τ_{PG} is isolated from the equation by replacing the terms by their expression:

$$\begin{aligned}
\gamma &= \frac{\frac{R_{c,max}}{R_s\,\tau_{PG}} + 1}{\frac{R_{c,min}}{R_s\,\tau_{PG}} + 1} \\
\gamma &= \frac{R_{c,max} + R_s\,\tau_{PG}}{R_{c,min} + R_s\,\tau_{PG}} \\
\gamma\,(R_{c,min} + R_s\,\tau_{PG}) &= R_{c,max} + R_s\,\tau_{PG} \\
\gamma\,R_s\,\tau_{PG} - R_s\,\tau_{PG} &= R_{c,max} - \gamma\,R_{c,min} \\
\tau_{PG} &= \frac{R_{c,max} - \gamma\,R_{c,min}}{R_s\,(\gamma - 1)}
\end{aligned}$$

This is where the precision of the value of R_s has its importance. Indeed, an imprecision of this value would lead to a different transmission range than the one initially desired.

So, this expression gives the desired train value for the PG in function of the parameter γ and the CVT dimensioning. As mentioned in the section 2.2, the train value is expressed as:

$$\tau_{PG} = -\frac{N_3}{N_1} = -\frac{R_3}{R_1}$$

where N_i and R_i are respectively the number of teeth and the pitch radius of the gear i.

It has to be noted that the erroneous value of R_s is not the only reason why the range will change, like it will be explained just after.

Therefore, to determine the dimensions of the PG, two values have to be set: the pitch radius of the ring R_3 and the module m. The first one is chosen to be equal to the radius of the ring in the CVT: $R_3 = R_7$. The module is a scaling factor to describe a set of gears meshing together. It can be described as the pitch diameter (given in $[mm]$) divided by the number of teeth of a gear. It is arbitrarily chosen in the usual set of values (0.5, 1, 1.5, 2, ...) so that the gears sustain the transmitted torque. This condition is verified a posteriori by comparing the torques and forces present in the mechanism with the maximum torque values given in manufacturer tables. In this dimensioning, $m = 1$.

From those, the number of teeth on each gear can be determined. Of course, the results are rounded to the nearest integer.

The number of teeth on the ring is, by definition of the module, expressed as:

$$N_3 = \frac{2\,R_3}{m}$$

The number of teeth on the sun is given from the desired train value:

$$N_1 = -\frac{N_3}{\tau_{PG}}$$

Those numbers of teeth have to respect the following condition:

$$\frac{N_3 + N_1}{n} = i$$

where $n = 4$ is the number of planets. The value i has to be an integer in order to have equidistant planets, and therefore equally distributed forces. If this condition is not respected, the number of teeth on the sun N_1 is incremented or decremented until the condition is satisfied. This may lead to a new value of

the train value and therefore it has to be recomputed later. This potential new value is the second reason why the IVT will not have the desired range of transmission ratio.
The number of teeth on the planets is given by the expression:

$$N_2 = \frac{N_3 - N_1}{2}$$

Finally, the pitch radius of the different gears is recomputed with:

$$R_i = \frac{N_i\, m}{2}$$

and the radius of the planet carrier of the PG is given by:

$$R_4 = R_1 + R_2$$

This concludes the dimensioning of the elements in the PG, and therefore in the IVT.

The torque profile of each joint can be found in the chapter 5 in the figure 5.6. From this graph, the maximum and minimum values are retrieved and the PGs are dimensioned following the development explained above. The results are summarised in the table 6.2.

Table 6.2: PGs geometrical dimensioning: summary of the elements' radius in the PG and the intermediate values.

Description	Symbol	Hip PG	Knee PG
Joint required torque range $[Nm]$	T	$[-27.5836\,;\,77.8078]$	$[-26.5505\,;\,50.4628]$
Torque ratio $[-]$	γ	-2.8208	-1.9006
PG ring radius $[mm]$	R_3	40.0	36.0
PG sun radius $[mm]$	R_1	14.0	12.0
PG planets radius $[mm]$	R_2	13.0	12.0
PG planet carrier radius $[mm]$	R_4	27.0	24.0
PG train value $[-]$	τ_{PG}	-2.8571	-3.0

6.1.3 Internal contact forces

Now that all dimensions of the IVT have been computed, it is possible to compute the maximum admissible forces in the design, in particularly in the CVT. The transmission is performed by friction between the rollers and the cones, and between the cones and the sun. Those elements are in single contact point, inducing high Hertzian stresses.

When two curved elements are in contact, their contact patch can be summarised by a centred ellipse where the material sustains elastic deformation. The contact patch area increases in function of the contact force F_c and materials properties. The Hertzian theory allows to determine the maximum admissible constraint before the deformation ($> 0.2\%$) is not considered elastic anymore.

The Hertzian contact parameters for the ellipsoid contact patch can be obtained by applying the

following equations:

$$\sigma_{max} = \frac{1.5\,F_c}{\pi\,a\,b}$$
$$b = \lambda \left[\frac{3\,F_c}{4\,(B+A)}\left(\frac{1-\nu_1^2}{E_1}+\frac{1-\nu_2^2}{E_2}\right)\right]^{1/3}$$
$$a = \frac{b}{\kappa}$$

where a and b are respectively the half lengths of the long and short axes of the ellipse and ν_i and E_i are respectively the Poisson's coefficient and the Young modulus of the material of the component i.

The parameters $(B-A)$ and $(B+A)$ are related to the surface principal curvatures of the elements in contact by the expressions:

$$(B+A) = 0.5\left[\frac{1}{R_{12}}+\frac{1}{R_{11}}+\frac{1}{R_{22}}+\frac{1}{R_{21}}\right]$$
$$(B-A) = 0.5\left[\left(\frac{1}{R_{12}}-\frac{1}{R_{11}}\right)^2+\left(\frac{1}{R_{22}}-\frac{1}{R_{21}}\right)^2-2\left(\frac{1}{R_{12}}-\frac{1}{R_{11}}\right)\left(\frac{1}{R_{22}}-\frac{1}{R_{21}}\right)\right]^{1/2}$$

where R_{ij} is the curvature radius of the element i in the plane j.

The parameters κ and λ depend on the surface principal curvatures. They can be approximated by linear relations with respect to $\frac{B-A}{B+A}$.

$$\kappa = 0.95 - 0.89\,\frac{B-A}{B+A}$$
$$\lambda = 1.02 - 0.60\,\frac{B-A}{B+A}$$

The maximum contact stresses can largely exceed other types of stresses (bending, torsion) without failure. This is explained by the fact that the zone of deformation is under compression. This value can reach up to 5 times the value of the yield strength depending on the geometry.

In order to use the Hertzian theory, it is necessary to determine the surface principal curvatures radius in each case.

In the case of the roller/cones contact, the roller is considered as the element 1 and the cone as the element 2. In the plane 1 (represented in the figure 6.1), the value of the curvature radius R_{11} is negative because the contact is situated inside the ring radius R_7. The value of R_{21} is the cones radius $R_{6'}$ and will vary with the desired transmission ratio. In the plane 2 (represented in the figure 6.2), the value R_{21} is the radius of the roller $R_{7'}$. The value R_{22} is infinite because it is the radius of the edge of the cones, a straight line.

In the sun/cones contact represented in the figure 6.3, the values R_{21} and R_{22} are infinite because the element 2 considered is the bottom of the cones, a plane. The other values R_{11} and R_{12} are respectively the radius of the sun R_5 and curvature radius of the edge of the sun $R_{5'}$.

The table 6.3 summarises their values.

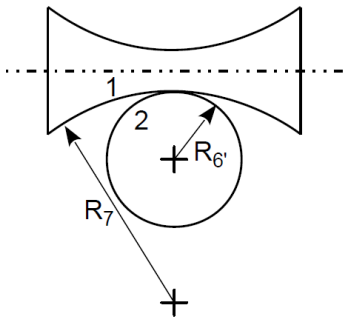

Figure 6.1: Scheme of roller/cones contact. Plane 1.

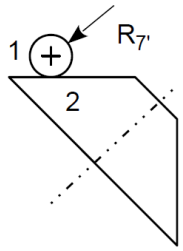

Figure 6.2: Scheme of roller/cones contact. Plane 2.

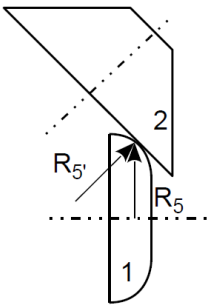

Figure 6.3: Scheme of sun/cones contact. Plane 1.

Table 6.3: CVT components surface principle curvatures for Hertz theory.

Hertz parameters	R_{11}	R_{12}	R_{21}	R_{22}
Roller/cones contact	$-R_7$	$R_{7'}$	$R_{6'}$	∞
Sun/cones contact	R_5	$R_{5'}$	∞	∞

The rollers, cones and sun of the CVT are made of Steel 100Cr6. This material is used for ball bearings and has a huge yield strength to resist to high Hertzian stresses. Its characteristics are: $\sigma_y = 2.4\,[GPa]$, $E = 210\,[GPa]$ and $\nu = 0.3$.

Then the Hertz parameters $(B+A)$, $(B-A)$, λ and κ are computed for both contact cases. Moreover, the materials characteristics are compacted into the factor:

$$D = \left(\frac{1-\nu_1^2}{E_1} + \frac{1-\nu_2^2}{E_2}\right) = 8.667 \times 10^{-12}\,[Pa^{-1}]$$

in order to express the maximum admissible contact force F_c between the elements in function of these parameters.

$$\sigma_{max} = \frac{1.5\,F_c}{\pi\,a\,b} \Rightarrow F_c = \frac{\pi\,b^2\,\sigma_{max}}{1.5\,\kappa}$$

$$b = \lambda\left[\frac{3\,F_c}{4\,(B+A)}\,D\right]^{1/3} = \lambda\left[\sigma_{max}\,\frac{3\,\pi\,b^2}{6\,\kappa\,(B+A)}\,D\right]^{1/3}$$

$$\Rightarrow b = \sigma_{max}\,\frac{\pi\beta^3 D}{2\,\kappa\,(B+A)}$$

$$\Rightarrow F_c = \frac{\pi\,\sigma_{max}}{1.5\,\kappa}\left[\sigma_{max}\,\frac{\pi\beta^3 D}{2\,\kappa\,(B+A)}\right]^2 = \sigma_{max}^3\,\frac{\pi^3\,\lambda^6\,D^2}{6\,\kappa^3\,(B+A)^2}$$

This last equation gives the maximum admissible contact force. The maximum stress is dependent on the geometry but is not determined in the case of this design. Therefore it is supposed to be equal to the yield strength of the material: $\sigma_{max} = \sigma_y$.

Now, the propagation of forces is necessary to verify that the design stays into the limits imposed by the Hertz theory. In the design, the force in the roller/cones contact induces the force in the sun/cones contact.

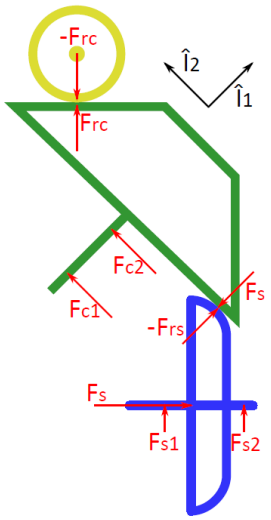

Figure 6.4: Free body diagram of the CVT's elements [52].

To help calculating the maximum forces between CVT's elements, the free body diagram is drawn in the figure 6.4.

The force equilibrium along the $\hat{I}_1$ axis on the cone gives the following equations:

$$F_{rs} = F_{rc} \cos \frac{\pi}{2} = \frac{F_{rc}}{\sqrt{2}}$$

The force equilibrium on the sun along its axis gives the following equations:

$$F_s = F_{rs} \cos \frac{\pi}{2} = \frac{F_{rs}}{\sqrt{2}}$$

The maximum value in the roller/cones contact $F_{rc,max}$ is computed from the Hertz theory. From this value, the force in the sun/cones contact is given by:

$$F_{rs} = \frac{F_{rc,max}}{\sqrt{2}} \leq F_{rs,max}$$

The maximal admissible value $F_{rs,max}$ is given by the Hertz theory within the sun/cones contact. If the condition is not respected, the curvature radius of the sun edge R_{rs} has to be increased. The force F_s to apply to the sun to make the contact with four cones in the CVT is given by:

$$F_s = 4 \frac{F_{rs}}{\sqrt{2}}$$

Table 6.4: Internal contact forces: summary of intermediate values in Hertz theory.

Hertz parameters	Hip CVT		Knee CVT	
	roller/cones contact	sun/cones contact	roller/cones contact	sun/cones contact
$(B+A)$	[75.0 ; 112.5]	117.2161	[83.3333 ; 12.5]	131.041
$(B-A)$	[12.5 ; 50.0]	48.8506	[13.8889 ; 55.5556]	54.1311
κ	[0.3567 ; 0.8511]	0.5810	[0.3567 ; 0.8511]	0.5824
λ	[0.62 ; 0.9533]	0.7714	[0.62 ; 0.9533]	0.7722
F_c	[516.2275 ; 1194.2]	414.7834	[418.1443 ; 967.3003]	335.2594

From this table 6.4, the maximum contact force used in the roller/cones contact for the design is retrieved as the minimum value of F_c. The condition on the maximum force in the sun/cones contact is verified in the dimensioning.

For the hip:

$$F_{rs} = \frac{F_{rc,max}}{\sqrt{2}} = 365.0280 \leq F_{rs,max}$$

For the knee:

$$F_{rs} = \frac{F_{rc,max}}{\sqrt{2}} = 295.6726 \leq F_{rs,max}$$

Therefore the curvature radii of the edge of the dimensioned dome-shaped sun $R_{5'}$ are sufficiently large to resist the constraints in the mechanism.

6.1.4 Torque transmission

The output torque of the IVT is the resultant of two different torques with different origins. The first one comes from the CVT, limited by the friction between its elements. The second contribution is from the PG, limited by the gears teeth maximum force.

More precisely, the CVT torque is limited by the admissible torques at the roller/cone and cone/sun contact points before slipping. The design uses traction fluid, with a friction coefficient $\mu = 0.1$.

Two cases have to be examined: the maximum torque transmitted before the cones slip on the rollers and before the cones slip on the sun.

In the first case, the roller/cones contact, the maximum tangential force applied by the cones on the roller is given by:

$$F_6 = \mu\, F_{rc,max}$$

The torque on each cone corresponds to the force multiplied by the cone radius $R_{6'}$.

$$T_6 = F_6\, R_{6'}$$

The tangential force between a cone and the sun corresponds to the torque divided by the radius of the contact.

$$F_5 = \frac{T_6}{R_6}$$

The torque transmitted to the sun T_5 corresponds to F_5 multiplied by the sun radius and the number of cones.

$$T_5 = 4\, F_5\, R_5$$

The torque transmitted to the planet carrier T_8 corresponds to the force of the sun multiplied by the sun radius plus the force from the cone multiplied by the ring radius R_7 and multiplied by the number of cones.

$$T_8 = 4\,(F_6\, R_7 + F_5\, R_5)$$

A similar reasoning is developed for the sun/cones contact slippage. The maximum tangential force applied by the cones on the sun is given by:

$$F_5 = \mu\, F_{rs,max}$$

The torque transmitted to the sun T_5 corresponds to F_5 multiplied by the sun radius and the number of cones.

$$T_5 = 4\, F_5\, R_5$$

The torque on each cone corresponds to F_5 multiplied by R_6.

$$T_6 = F_5\, R_6$$

The tangential force between a cone and a roller F_6 corresponds to T_6 divided by the cone radius $R_{6'}$

$$F_6 = T_6\, R_{6'}$$

The torque transmitted to the planet carrier T_8 corresponds to F_5 multiplied by the sun radius plus F_6 multiplied by the ring radius and multiplied by the number of cones.

$$T_8 = 4\,(F_6\, R_7 + F_5\, R_5)$$

These two developments give different values for T_5, T_6 and T_8 depending of the cones radius. The minimum between the two of them for each possible values of $R_{6'}$ determines the maximum admissible torques for the design. The figures 6.5 and 6.6 show the admissible torques in the CVTs dimensioned for the hip and the knee respectively.

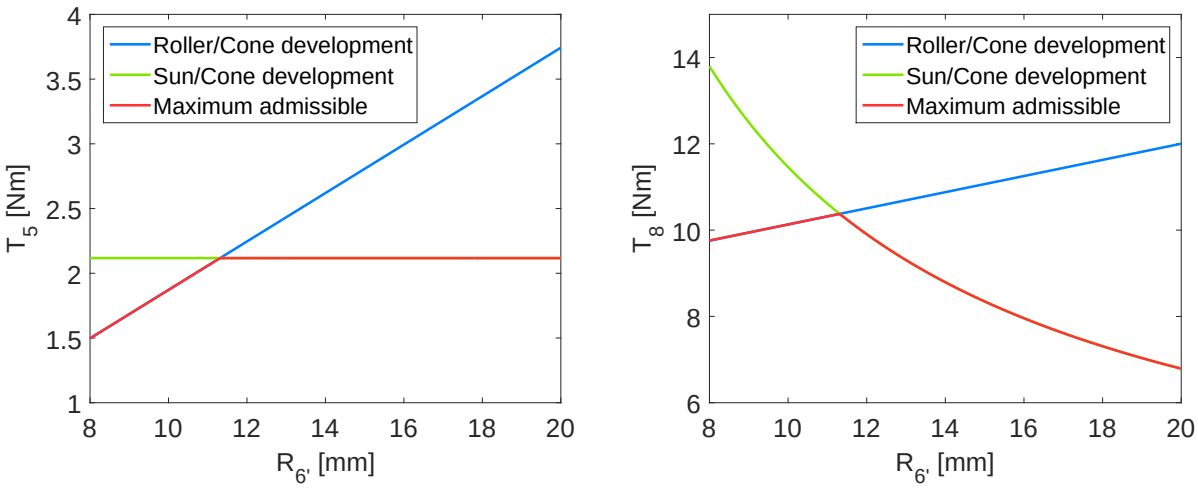

Figure 6.5: Maximum admissible torques for the sun (left) and the planet carrier (right) in the Hip CVT.

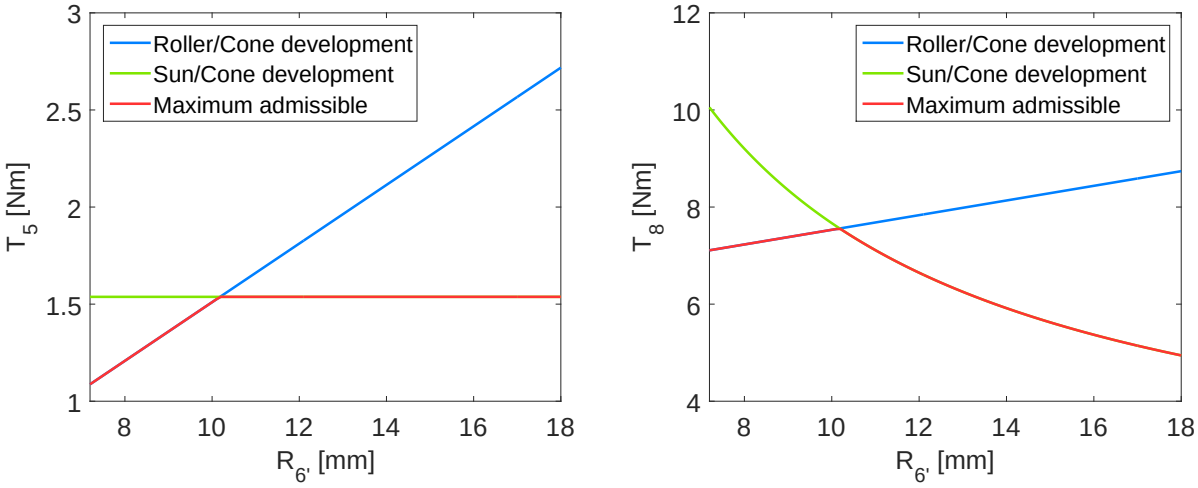

Figure 6.6: Maximum admissible torques for the sun (left) and the planet carrier (right) in the Knee CVT.

The connection of the planetary gears with the CVT adds torque on the sun and on the planet carrier of the CVT. On the PG, the sun/planets tangential force F_1 corresponds to the sun torque divided by the planetary gears sun radius and by the number of planets.

$$F_1 = \frac{T_1}{4\,R_1}$$

Due to torque equilibrium on the planet, the ring/planet tangential force F_3 is equal to the sun/planets tangential force F_1 while the force transmitted to the planet carrier F_4 is the double of the sun/planets tangential force F_1.

$$F_3 = F_1$$

$$F_4 = 2\,F_1$$

The torque transmitted to the planet carrier T_4 corresponds to F_4 multiplied by the planet carrier radius and the number of planets.

$$T_4 = 4\,F_4\,R_4$$

The torque transmitted to the ring T_3 corresponds to F_3 multiplied by the ring radius and the number of planets.

$$T_3 = 4\, F_3\, R_3$$

The IVT is the combination of the CVT and the planetary gears. The planetary gears ring is considered as the input of the IVT and the CVT planet carrier is considered as its output. The CVT planet carrier receives two torques. The first one comes from the CVT itself and the second one comes from the planetary gears. Those two torques have opposite signs and tend to cancel each other.

$$T_{8'} = T_4 - T_8$$

For a certain CVT ratio, these two torques are equal and the total torque on the CVT planet carrier is equal to zero. The figures 6.7 and 6.8 show the resulting torque $T_{8'}$ respectively in the case of the hip's IVT and the knee's IVT for the maximal torque T_3 allowed in the design and in function of the cone radius. The torque T_3 has its minimum value for the smallest cone radius and quickly reaches a plateau as $R_{6'}$ increases. The torque in the planet carrier $T_{8'}$ varies from negative to positive value as designed.

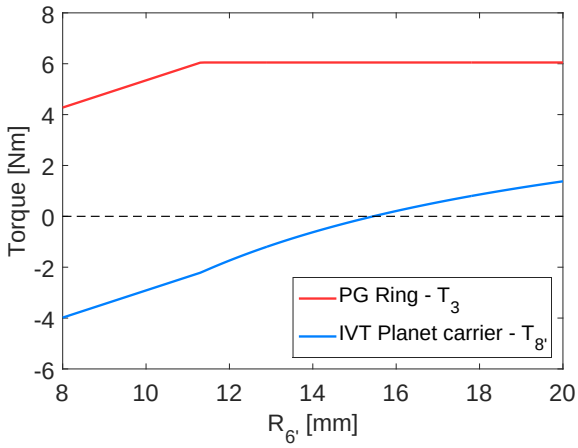

Figure 6.7: Maximum admissible torques for the PG's ring and the planet carrier in the Hip IVT.

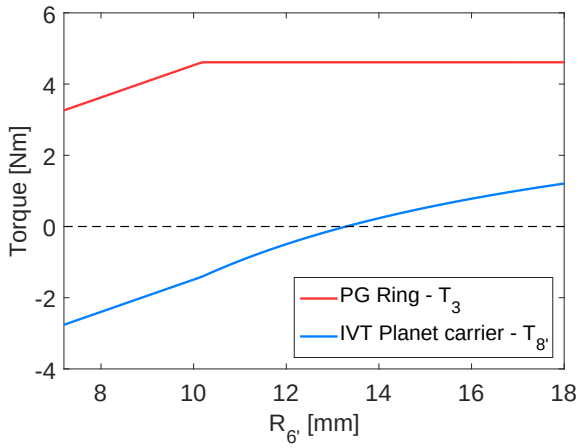

Figure 6.8: Maximum admissible torques for the ring and the planet carrier in the Knee IVT.

The ring of the planetary gears is thus considered as the input of the IVT and the planet carrier as the output. The input torque T_3 is imposed as constant, equal to $4\,[Nm]$ in the case of the hip's IVT and to $3\,[Nm]$ for the knee's IVT. Those values are chosen to respect the limitations shown in the figures 6.7 and 6.8 with a small margin. The output torque $T_{8'}$ depends on the position of the rollers on the cones, varying the effective cones radius $R_{6'}$. The values taken by $T_{8'}$ are depicted in the figures 6.9 and 6.10.

The IVT for the hip joint can provide a torque varying between $[-3.7241\,;\,0.9103]\ [Nm]$ while the one for the knee has a range of $[-2.5385\,;\,0.7846]\ [Nm]$. These torques are not sufficient for the actuation of the joints and are thus increased by the powertrain.
The dimensions of the IVT prototype [36] has a diameter of $110\,[mm]$ for a length of $50\,[mm]$. The proportions are kept from one design to another. Thus, since the prototype has a ring radius $R_7 = 30\,[mm]$, the IVTs dimensioned for the hip and knee have a diameter of $146\,[mm]$ and $132\,[mm]$ for a length of $66\,[mm]$ and $60\,[mm]$ respectively.

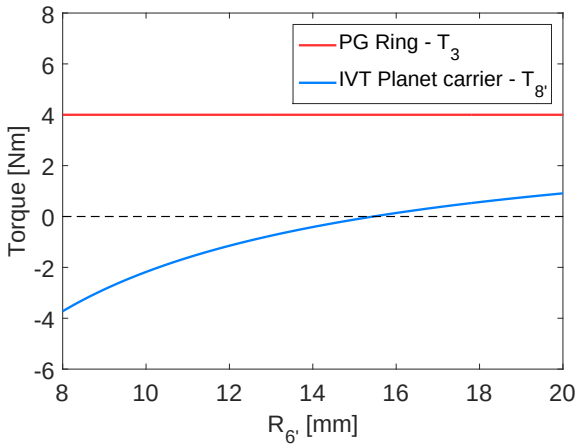

Figure 6.9: Output torque variation of the Hip IVT for an input torque of 4 $[Nm]$.

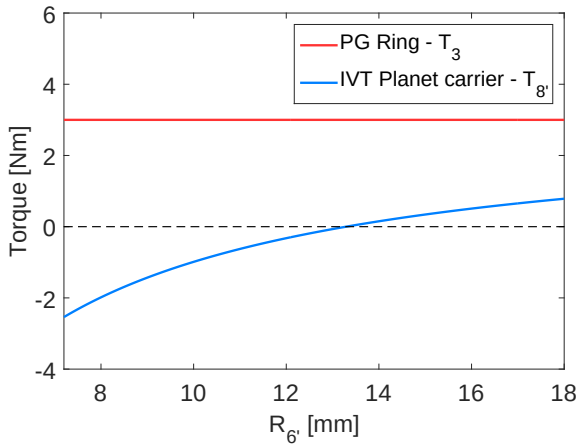

Figure 6.10: Output torque variation of the Knee IVT for an input torque of 3 $[Nm]$.

6.2 PGs' transmission ratio dimensioning

Planetary gears trains are used in series to increase the output torque of the IVTs up to the required torque in the joints of the robot. The configuration used is similar to the one presented in the section 2.2. This time, the rings are fixed and the input is at the sun while the output is on the planet carrier. This arrangement gives the following torque relation:

$$\tau_{PG} = \frac{T_c}{T_s} = \frac{N_r + N_s}{N_s}$$

The constant value of the transmission ratio τ_{PG} of this mechanism is determined as the worst case between the ratios of the torques required divided by the output torques of the IVT. Indeed, the imprecision in the dimensioning of the IVT on the range of the output torque implies this precaution. Therefore the transmission ratio is given by:

$$\tau_{PG} = max\left(\frac{T_{max}}{\tau_{IVT,max}}; \frac{T_{min}}{\tau_{IVT,min}}\right)$$

with the abstraction of the sign of these values.

The maximum value of a transmission ratio in a stage of PG is commonly set at 10:1 [45]. If τ_{PG} exceeds this value, a second stage of PG is put in series. It is asked to the first stage to maximise its gear ratio in order to decrease the size of the second stage. The module m of the set of gears used may differ from one stage to the other. In fact, the second stage will have a bigger module in order to have a higher admissible torque. The critical part is the sun gears, which are smaller, that have to sustain the input torque in each stage.

Because the mechanism is inside a complex system, the size of the ring is limited to a diameter R_r. This allows to determine the number of teeth on the ring N_r once the module is fixed. The other parameters of the PG are determined as in the other dimensioning.
The number of teeth on the sun is given with the transmission ratio formula:

$$N_s = \frac{N_r}{\tau_{PG} - 1}$$

It has to respect the condition for equidistant planets:

$$\frac{N_r + N_s}{n} = i$$

where i has to be an integer, and n is the number of planets (four planets are considered in the design). The number of teeth on the planets are then given by:

$$N_p = \frac{N_r - N_s}{2}$$

When the gears are dimensioned, the admissible torque is verified with the manufacturer's tables. If the admissible torque is not enough for one gear, the module of the set of the corresponding stage is increased and the dimensioning starts over.

Since the transmission ratio may have changed with the meshing condition it has to be recomputed. From this new value, the transmission ratio of the second stage is computed by dividing the initial ratio by the one of the first stage. Then the same steps are applied to dimension the second stage by adapting the module.

Finally, the transmission ratio of the two stages are multiplied to give the ratio of the whole system. This ratio has to be strictly greater than the one initially asked in order to be sure to deliver the required torque.

The dimensioned PGs posses a ring radius R_r of 50 $[mm]$ in order to be smaller than the IVTs. The results of the dimensioning are summarised in the table 6.5 regrouping the cited dimensions and ratio for the two different joints.

Table 6.5: Increase torque dimensioning: summary of numbers of teeth in PGs' gears and torque ratios.

Symbol	Hip PGs		Knee PGs	
	Stage 1	Stage 2	Stage 1	Stage 2
m	1	2	1	2
N_r	100	50	100	50
N_s	16	14	12	18
N_p	42	18	44	16
τ_{PG}	7.25	4.5714	9.3333	3.7778
τ	33.1429		35.2593	

The torques at the output of the IVTs are therefore multiplied by the transmission ratio of the PGs stage. The resulting torques are represented in the figure 6.11 and 6.12 in blue. The available ranges of torque for the hip and for the knee are respectively $[-31.1688\,;\,123.4179]$ and $[-27.6577\,;\,89.4808]$.

The figures 6.11 and 6.12 also show the range of torques required in the simulation. The green markings represent the maximum and minimum values of torque at the start of the walk. Those are greater than the torques required during the steady state, depicted with orange marks in the graphs. It is observed that the powertrain can delivered higher torques than those required, in particular for the knee joints. This is due to the imprecision on the dimensioning of the PG of the IVT as already mentioned. A second reason is that the values of torque used for the dimensioning were the maximal and minimal value of the entire simulation, i.e. at the start of the walk. This is less visible for the hip joint, where the positive peak of torque is close to the steady state value. But for the knee, the final result shows that nearly the half of the range will be unused in steady state.

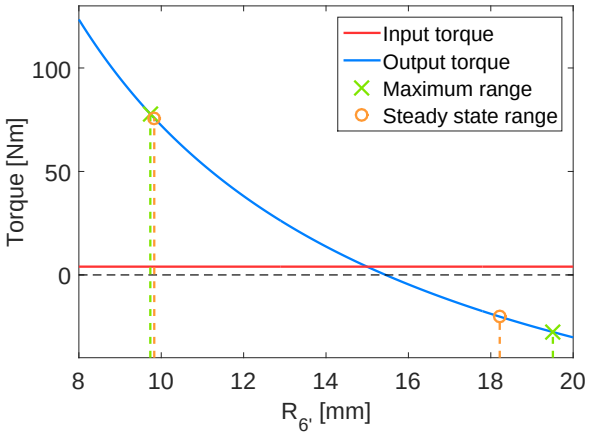

Figure 6.11: Torque available to the hip joint and range of use.

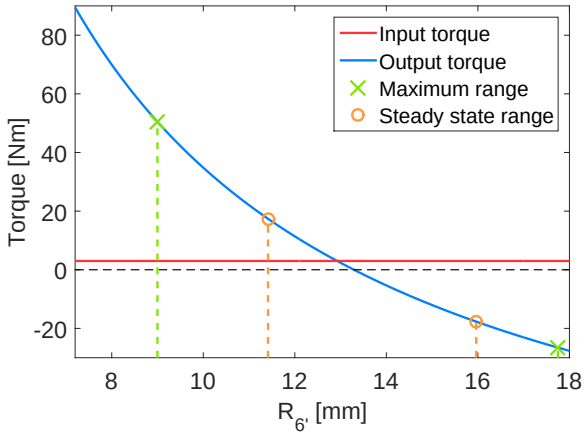

Figure 6.12: Torque available to the knee joint and range of use.

6.3 Mechanical differentials dimensioning

The mechanical differentials are used to distribute the power from the spring to the 4 IVTs. The first stage divided the robot between the left and right legs. The second one separates the torque between the hip and the knee IVTs.

The mechanical differentials have the property to fix the transmission ratio of the torques but to have variable angular velocities at their outputs.

6.3.1 First stage: bevel gears differential

The first stage of differential is similar to the one used in automotive application. The figure 6.13 represent the differential that can be seen as a planetary train with bevel gears.

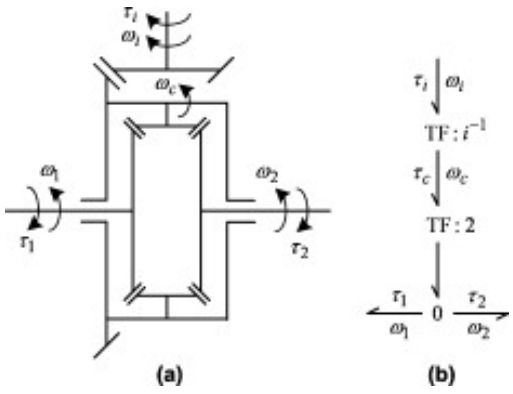

Figure 6.13: Mechanical differential with bevel gears [53].

The input shaft drives the planets carrier and a gear ratio is possible between them. The planets rotating with the carrier drive the sun and the ring which are coaxial and of the same diameter. This implies that the output torques are both equal to the half of the torque seen in the planets carrier.

$$T_r = T_s = \frac{T_c}{2}$$

The angular velocities of the outputs are related to the velocities in the carrier by the relation:

$$\omega_c = \frac{\omega_r + \omega_s}{2}$$

This means that the spring will discharge itself with a speed equal to the mean of the angular velocities needed at the output.

The pre-dimensioning of this part of the mechanism is centred on the geometrical constraints and the transmission ratio. The first stage of differential is at the centre of the robot and has a limited space available. It is chosen that it must be contains in a box of 100 $[mm]$ of diameter and 50 $[mm]$ width. Those dimensions are equivalent respectively to the size of the planets carrier and input gears. The transmission ratio between the input and the planets carrier is therefore 1:2. The sun and ring gears have to be smaller than the carrier, and the planets smaller than the input. The set of gears used to respect those dimensions are directly chosen in the catalogue from the manufacturer Misumi [54].

The tables 6.6 regroups the main dimensions of the gears set chosen to satisfy the geometrical constraints.

Table 6.6: Summary of the gears' diameter dimensioning in the first stage of differential.

Symbol	Value $[mm]$	Description
m	2.5	Gears module.
D_i	50.0	Input gear pitch diameter.
D_c	100.0	Carrier gear pitch diameter.
τ_i	1 : 2	Input/carrier gear ratio.
D_1	75.0	Sun gear pitch diameter.
D_2	75.0	Ring gear pitch diameter.
D_p	37.5	Planets gear pitch diameter.

The gears are selected in the catalogue of the manufacturer Misumi [54]. The set of bevel gears for the input and carrier contact is then labelled 20:40, corresponding to the respective numbers of teeth. In the same way, the set for the sun/ring and planets is labelled 15:30. The pitch diameters allow to select the correct pair of gears in the tables in order to verify their admissible torque transmission.

6.3.2 Second stage: planetary gears train

The second stage of mechanical differential uses planetary gears trains. This time, no part of the system is held fixed. The input is at the planets carrier, the ring is the output leading to the IVT of the Hip joint while the sun is the output to the knee joint. The torque ratio between the two outputs corresponds to the ratio of required input torque of the IVTs. This expression leads the dimensioning of the trains.

$$\frac{T_r}{T_s} = \frac{N_r}{N_s} = \frac{4}{3}$$

The dimensioning of the gears in this kind of mechanism is already seen multiple times in this master thesis, as in 2.2. The tables 6.7 regroups the result of this dimensioning.

Table 6.7: Summary of the gears' number of teeth dimensioning in the second stage of differential.

Symbol	Value $[mm]$	Description
m	1.0	Gears module.
N_r	96	Ring number of teeth.
N_p	12	Planets number of teeth.
N_s	72	Sun number of teeth.

The torque ratio between the ring and sun outputs does respect the desired value as defined above.

6.4 Torsion spring dimensioning

The torsion spring is used in the design to store a huge amount of mechanical energy. Its dimensions and characteristics will influence the efficiency of the system.

In particular, the stiffness is needed as low as possible. It directly influences the amplitude of the oscillations of torque around the mean value imposed by the main motor. The lower the stiffness, the lower the oscillations will be. These oscillations of torque are equivalent to oscillations of power provided by the motor. But to have a low the stiffness, the spring dimensions will be large.

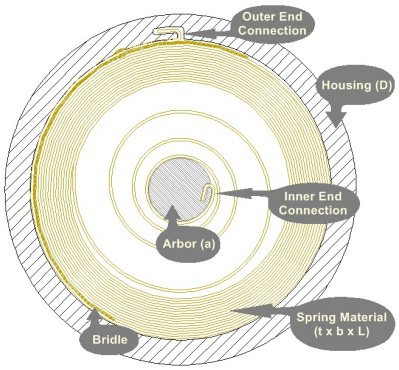

Figure 6.14: Power spring [55].

The spiral spring is dimensioned in order to deliver the required torque at the input of the first differential which is:

$$T_{spring} = 7.0\,[Nm]$$

The oscillations are not yet predicted, therefore a safety factor $k_s = 1.5$ is used to dimension the spring to not break.

The geometrical constraints imposed in the design is the available space for the spring. In the powertrain, the spring is put at the top of the mechanism in order to have a maximum of space available. The limits imposed in this dimensioning are:

- Barrel diameter: $D_b = 100\,[mm]$
- Arbor diameter: D_a
- Barrel length: $b_l = 50\,[mm]$

The arbor diameter is the diameter of the shaft on which the spring is mounted. A quick torsion dimensioning (the main component of stresses in this case) allows to determined its value:

$$D_a = \left(\frac{16\sqrt{3}\, k_s\, T_{spring}}{\pi\, \sigma_y} \right)^{1/3} = 4.6\,[mm]$$

The length of the barrel is equivalent to the width of the steel band constituting the spring. The larger it is, the smaller the stiffness will be for the same maximum loading torque.

The others dimensions are computed in order to be able to deliver the required torque.

The spring is made of steel with a good yield strength, the steel AISI E9312 is chosen and its characteristics are: Young modulus $E = 210\,[GPa]$, yield strength $sigma_y = 952\,[MPa]$.

The main stress in a torsional spring as the spiral spring is bending stress:

$$\sigma_{max} = \frac{32\, k_s\, T_{spring}\, c}{I}\, K_{i,rect}$$

with $I = \frac{b_l\, h^3}{12}$ the moment of inertia of the rectangular area and $c = \frac{h}{2}$ the distance between the neutral axis and the edge of the material.

The spiral spring is rolled inside the barrel and fill a large part of its diameter. It is considered in horology [56] that the spring used the half of the diameter of the barrel: $D = \frac{D_b}{2} = 50\,[mm]$.

The spring index $C = \frac{D_s}{h} = 41.667$ allows to find the value of the curvature stress concentration $K_{i,rect} = 1.05$[1].

Therefore, the thickness wire can be computed by reorganising the terms in the bending stress equation giving:

$$h = \left(\frac{6\, K_s\, T_{spring}}{b_l\, \sigma_y}\, K_{i,rect} \right)^{1/2} = 1.2\,[mm]$$

The length of the wire L is then given by [56]:

$$L = \frac{1}{2\, h} \left[\left(\frac{\pi\, D_b^2}{4} \right) - \left(\frac{\pi\, D_a^2}{4} \right) \right] = 3.2656\,[m]$$

The stiffness k_spring of the spring is equal $\frac{E\, I}{L}$ or, by replacing the terms by their expression:

$$k_spring = \frac{E\, b_l\, h^3}{12\, L} = 0.4630\,[Nm/rad]$$

It will be important to check that such a stiffness k_spring does not lead to torque oscillations too large around the required torque.

6.5 Motors dimensioning

Two types of motor have to be dimensioned: the main motor giving the power to the entire powertrain and the smaller motors controlling the IVTs' transmission ratio.

[1] The value of the curvature stress concentration is retrieved from a graph available in the Juvinall [37], figure 12.30

6.5.1 Main motor specifications

The main power has to deliver the mean power P_m required at the four joints:

$$P_m = mean\left(\Sigma \frac{P_i}{\eta_i}\right)$$

where P_i is the power profile of the joint i and η_i the mechanical efficiency between the motor and the joint. The total efficiency is the multiplication of the efficiencies of all the elements between the joint and the motor.

At first, the gearbox's efficiency is considered around 75% (according to the Maxon catalog of gears). The efficiency of the first differential η_{diff} should be at least 95% and the second stage of differential has its efficiency computed with the efficiency of a planetary gears train $\eta_{PG} = 0.97$ [45]. The IVT efficiency η_{IVT} is approximated to a value of 80%, according to the experiments on a prototype [36]. The efficiency of the intermediate gears and belts are respectively taken as 93% and 95%. The table 6.8 summarises these values.

Table 6.8: Summary of elements' efficiency.

Efficiency	Value [−]	Description
$\eta_{gearbox}$	0.75	Gearbox efficiency.
η_{diff}	0.95	Mechanical differential efficiency.
η_{PG}	0.97	planetary gears train efficiency.
η_{gears}	0.93	Pair of gears efficiency.
η_{IVT}	0.80	IVT efficiency.
η_{belt}	0.95	Belt efficiency.

Thus, the efficiencies to the hips and knees are computed according to the powertrain morphology:

$$\eta_{knee} = \eta_{gearbox}\,\eta_{diff}\,\eta_{PG}\,\eta_{IVT}\,\eta_{PG}^2\,\eta_{belt}^2 = 0.6254$$
$$\eta_{hip} = \eta_{gearbox}\,\eta_{diff}\,\eta_{PG}\eta_{gears}\,\eta_{IVT}\,\eta_{PG}^2 = 0.5993$$

Finally the mean power of the motor is computed with the power profiles from the simulation 5:

$$P_m = 56.226\,[W]$$

6.5.2 IVT's control motor specifications

The variation of the IVT's transmission ratio is performed with the linear displacement of the ring on the cones in the CVT. This linear movement is translated from the rotary motion coming from the motor through synchronised screw threads. The development below considers values for the hip joint. The same motor for the knee joint will be used.

The threads considered in the design have a pitch of $p = 2\,[mm]$ and a diameter of $d_{nom} = 14\,[mm]$. The mass to displace is approximated to $m_r = 120\,[g]$ (the mass of the ring). The corresponding weight W to slide is computed considering a friction coefficient $\mu = 0.1$ (from the transmission fluids as in the CVT).

$$W = \mu\, m_r\, 9.81 = 0.1177\,[N]$$

The required torque to slide the ring is thus equal to $T_{screw} = 0.1238\,[mNm]$[2]. The efficiency of the screw thread is computed as $\eta_{screw} = \frac{W\,p}{2\,\pi\,T} = 0.3027\,[-]$

[2]The formula used to retrieved this value comes from the reference book Juvinall [37], eq. 10.3

From the data acquired in the simulation (see chapter 5), the torque in the joint varies from its maximum to minimum value in $t = 0.05\,[s]$. This means that the distance $l = \frac{20-8}{\sin 45\,\mathrm{deg}} = 17.0\,[mm]$, corresponding to the length of a cone side, is travelled at this rate cycle. This implies an angular velocities of:

$$\omega_{screw} = \frac{2\,\pi\,l}{p\,t} = 1066.3\,[rad/s]$$

corresponding to $10182\,[rpm]$. The required rotation speed is that high because, as mentioned in the simulation results, the walking frequency of the robot is too high.

Finally, the power required at the IVT's motor is computed as:

$$P_{m,IVT} = \frac{T_{screw}\,\omega_{screw}}{\eta_{screw}} = 0.43\,[W]$$

6.6 Further development

The next step of the dimensioning should be to compute the different parameters used in the Simulink file presented in the section 4.2. However as already explained there, due to a lack of time, this development is not performed.

Conclusion

This master thesis presented the first steps of the development of a humanoid walker of which all joints are actuated by a unique power motor using several differentials, Infinitely Variable Transmissions and planetary gears.

First, the biomechanics of human locomotion was presented to justify the interest of the use of IVTs. Indeed, as the net energy during one gait cycle is positive, it is interesting to retrieve the dissipated energy in the joints to reduce the energy that has to be provided by the power motor. This is realised thanks to compliant elements. In order not to limit the performances to a given walking speed, the stiffness of these elements is varied. This variation has to be performed by consuming as less energy as possible and this is why IVTs are used since nearly no energy is necessary for this stiffness variation.

Then, a mechanical design of the humanoid walker was achieved to meet the specifications. A functional analysis was realised on the basis of the specifications, allowing to divide the design into three parts with each its functions to fill. Solutions were then proposed and evaluated to finally reach a global solution. The system restricting the robot to its sagittal plane is done with a four bar linkage. Concerning the powertrain, the torque distribution to the two legs from the power motor is performed with several differentials. To provide the desired torque to the joints, IVTs are used as well as planetary gears allowing to increase the output torques of these latter. Besides, a potential energy storage, and more precisely a spring, is added at the output of the motor in order to smooth its power curve. About the legs, the human morphology is privileged to the four bar linkage, and for a reason of space optimisation, the hip joints are in direct mounting to the planetary gears while the knee joints are connected to the powertrain via two belts in series.

After having explained the design steps, the scheme of the controller was presented. The implemented high-level controller is a neuromuscular one based on the model of Geyer [40]. It is a model of human locomotion that is controlled by muscle reflexes which encode principles of legged mechanics. It allows to compute the referential torques to apply to the joints on the basis of their angular position and speed. A major part of the implementation of this model was retrieved from the doctoral thesis of Nicolas Van der Noot [46]. Some modifications have however been made to adapt it to the morphology of the robot of this master thesis, which was modelled in Robotran. Due to a lack of time, the developed simulation does not corresponds to reality but rather to the ideal case since the torques that are applied to the joints are those of reference. In fact, a Simulink file representing the powertrain allows to calculate the torques that are really sent to the joints on the basis of the referential torques. However the parameters of this file have not been tuned to match the realised dimensioning.

Next, the results of the simulation of a straight walking were presented and compared to human walking data [33] and to the data of the 2D version of COMAN obtained by Nicolas Van der Noot as part of his doctoral thesis [51]. It results from this that the obtained results are consistent and that the lack of ankle mainly reflects in the hip results and in a shorter double support phase, i.e. when both legs are in contact with the ground.

Several improvements could however be noted. The main one is to tune the parameters of the Simulink file to include it in the simulation, allowing then to analyse more realistic results rather than the ideal ones. Then, as the walking frequency of the robot is double that of a human, it could be preferable to impose the walking frequency as well as the stride length in order to have more realistic results. Moreover, the parameters of the ground contact model could be improved to get better results. Decrease the time step of the simulation could also allow to have more realistic results but since it increases the optimisation time, a trade-off has to be concluded. The implementation of a simulation for a circular path could also be realised by finalising what is already implemented and by optimising the parameters.

Finally, the last chapter of this master thesis presented the dimensioning of the main parts of the powertrain, namely the IVTs, the planetary gears, the differentials, the torsion spring and the motor. These computations were achieved on the basis of the values obtained with the simulation.
However, several improvements can be suggested. First of all, about the dimensioning of the IVTs, some geometrical hypotheses were made but could be modified in order to obtain more optimal results. Moreover, the available space for all the elements is critical and restricts thus the dimensioning. A larger robot would therefore allow to have more freedom. Next, the dimensioning of the spring and the motor could be more deeply realised. Finally, as the emphasis was put on the dimensioning of the powertrain, one could also dimension the belts, the legs, the boom and the other smaller elements that were neglected such as the shafts, intermediate gears, etc. in order to complete the mechanical dimensioning of the whole humanoid walker.

Bibliography

[1] *Biped robot RABBIT-ROBEA Project : "Control of a biped on walking and running gaits"*. URL: http://www.gipsa-lab.grenoble-inp.fr/projet/Rabbit/English/index.php (visited on 05/29/2017).

[2] Eric R. Westervelt et al. *Feedback control of dynamic bipedal robot locomotion*. CRC press, 2007.

[3] *Locomotion and Biomechanics Laboratory - Walking Robots*. URL: http://ame-robotics.nd.edu/LAB/Robots/Walking.php (visited on 05/29/2017).

[4] *AMBER Lab*. URL: http://www.bipedalrobotics.com/ (visited on 05/13/2017).

[5] *AMBER-Lab*. URL: https://www.youtube.com/user/ProfAmes (visited on 05/14/2017).

[6] *Watch Durus-2D, the jogging robot that moves like a human jogger*. Mar. 2016. URL: http://www.dailymail.co.uk/sciencetech/article-3499206/Watch-robot-jog-like-human-Researchers-say-Durus-2D-lead-radical-new-prosthetic-limbs.html (visited on 05/14/2017).

[7] Eric Cousineau and Aaron D. Ames. "Realizing underactuated bipedal walking with torque controllers via the ideal model resolved motion method". In: *Robotics and Automation (ICRA), 2015 IEEE International Conference on*. IEEE, 2015, pp. 5747–5753. URL: http://ieeexplore.ieee.org/abstract/document/7140004/ (visited on 05/14/2017).

[8] *Dynamic Robotics Laboratory*. URL: http://mime.oregonstate.edu/research/drl/robots/ (visited on 05/14/2017).

[9] *Dynamic Robotics Laboratory*. URL: http://mime.oregonstate.edu/research/drl/robots/mabel/ (visited on 05/14/2017).

[10] Koushil Sreenath et al. "Embedding active force control within the compliant hybrid zero dynamics to achieve stable, fast running on MABEL". In: *The International Journal of Robotics Research* 32.3 (2013), pp. 324–345. URL: http://journals.sagepub.com/doi/abs/10.1177/0278364912473344 (visited on 05/14/2017).

[11] Evan Ackerman. *MABEL Bipedal Robot is Fast Enough to Run You Down*. Aug. 2011. URL: http://spectrum.ieee.org/automaton/robotics/humanoids/mabel-bipedal-robot-is-now-fast-enough-to-catch-you (visited on 05/14/2017).

[12] *ATRIAS*. URL: http://daniel.human-motion-engineering.org/atrias/ (visited on 05/13/2017).

[13] *ATRIAS*. URL: http://mime.oregonstate.edu/research/drl/atrias/# (visited on 05/14/2017).

[14] *Dynamic Robotics Laboratory*. URL: http://mime.oregonstate.edu/research/drl/robots/atrias_1_0/ (visited on 05/14/2017).

[15] Christian Hubicki et al. "ATRIAS: Design and validation of a tether-free 3D-capable spring-mass bipedal robot". In: *The International Journal of Robotics Research* 35.12 (2016), pp. 1497–1521. URL: http://journals.sagepub.com/doi/abs/10.1177/0278364916648388 (visited on 05/13/2017).

[16] *ASIMO by Honda | The World's Most Advanced Humanoid Robot*. URL: http://asimo.honda.com/ (visited on 05/14/2017).

[17] *ASIMO Photo Gallery | ASIMO Innovations by Honda*. URL: http://asimo.honda.com/gallery/ (visited on 05/14/2017).

[18] *Boston Dynamics: Dedicated to the Science and Art of How Things Move*. URL: http://www.bostondynamics.com/robot_Atlas.html (visited on 05/14/2017).

[19] Siyuan Feng et al. "Optimization based full body control for the atlas robot". In: *Humanoid Robots (Humanoids), 2014 14th IEEE-RAS International Conference on*. IEEE, 2014, pp. 120–127. URL: http://ieeexplore.ieee.org/abstract/document/7041347/ (visited on 05/14/2017).

[20] *DARPA Robotics Challenge*. en. Page Version ID: 777974973. Apr. 2017. URL: https://en.wikipedia.org/w/index.php?title=DARPA_Robotics_Challenge&oldid=777974973 (visited on 05/29/2017).

[21] *DARPA*. en. Page Version ID: 782328827. May 2017. URL: https://en.wikipedia.org/w/index.php?title=DARPA&oldid=782328827 (visited on 05/29/2017).

[22] *DARPA Robotics Challenge (DRC)*. URL: http://www.darpa.mil/program/darpa-robotics-challenge (visited on 05/29/2017).

[23] DRCihmcRobotics. *Atlas Walking over Partial Footholds*. URL: https://www.youtube.com/watch?v=_5PtxHsr038 (visited on 05/14/2017).

[24] DRCihmcRobotics. *IHMC DRC Trials Preview*. URL: https://www.youtube.com/watch?v=RxubYsB8_Tg (visited on 05/14/2017).

[25] Erico Guizzo and Evan Ackerman. *WALK-MAN Team Built Brand New, Highly Custom Robot for DRC Finals*. June 2015. URL: http://spectrum.ieee.org/automaton/robotics/humanoids/walkman-humanoid-robot-iit (visited on 05/29/2017).

[26] *WALK-MAN - Walk-Man*. URL: https://www.walk-man.eu/ (visited on 05/29/2017).

[27] Istituto Italiano di Tecnologia. *IIT robot WALKMAN ready for the DARPA Robotics Challenge 2015*. URL: https://www.youtube.com/watch?v=kZzwVwzAWME.

[28] Jason Falconer. *This Humanoid Robot Gets Pushed Around But Stays on Its Feet*. Apr. 2013. URL: http://spectrum.ieee.org/automaton/robotics/humanoids/iit-coman-humanoid-robot (visited on 05/31/2017).

[29] *COMAN - compliant humanoid robot*. June 2011. URL: http://kormushev.com/topics/coman-robot/ (visited on 05/31/2017).

[30] *COmpliant HuMANoid Platform (COMAN) | AMARSi Project*. URL: https://www.amarsi-project.eu/coman (visited on 05/31/2017).

[31] *Kengoro*. URL: http://www.jsk.t.u-tokyo.ac.jp/research/kengoro.html (visited on 05/14/2017).

[32] Evan Ackerman. *This Robot Can Do More Push-Ups Because It Sweats*. Oct. 2016. URL: http://spectrum.ieee.org/automaton/robotics/humanoids/this-robot-can-do-more-pushups-because-it-sweats (visited on 05/14/2017).

[33] David A. Winter. *Biomechanics and Motor Control of Human Movement, 4th Edition*. 2009.

[34] D. W. Robinson et al. "Series elastic actuator development for a biomimetic walking robot". In: *1999 IEEE/ASME International Conference on Advanced Intelligent Mechatronics (Cat. No.99TH8399)*. Sept. 1999, pp. 561–568.

[35] Alin Albu-Schäffer et al. "Dynamic modelling and control of variable stiffness actuators". In: *Robotics and Automation (ICRA), 2010 IEEE International Conference on*. IEEE, 2010, pp. 2155–2162. URL: http://ieeexplore.ieee.org/abstract/document/5509850/ (visited on 06/08/2017).

[36] Christophe Everarts, Bruno Dehez, and Renaud Ronsse. "Novel infinitely Variable Transmission allowing efficient transmission ratio variations at rest". In: IEEE, Sept. 2015, pp. 5844–5849. ISBN: 978-1-4799-9994-1. URL: http://ieeexplore.ieee.org/document/7354207/.

[37] Robert C. Juvinall and Kurt M. Marshek. *Fundamentals of Machine Component Design*. Anglais. 5th Edition. Hoboken, NJ: John Wiley & Sons, Oct. 2011. ISBN: 978-1-118-01289-5.

[38] *Planetary gear ratio calculations*. URL: https://woodgears.ca/gear/planetary.html (visited on 06/09/2017).

[39] Alexandre Debarsy. "Energy transfer in an IVT based powered transfermoral prosthesis". MA thesis. Université Catholique de Louvain, 2014.

[40] H. Geyer and H. Herr. "A Muscle-Reflex Model That Encodes Principles of Legged Mechanics Produces Human Walking Dynamics and Muscle Activities". In: *IEEE Transactions on Neural Systems and Rehabilitation Engineering* 18.3 (June 2010), pp. 263–273. ISSN: 1534-4320.

[41] E. J. Rouse et al. "Clutchable series-elastic actuator: Design of a robotic knee prosthesis for minimum energy consumption". In: *2013 IEEE 13th International Conference on Rehabilitation Robotics (ICORR)*. June 2013, pp. 1–6.

[42] *Harmonic Drive gear | High precision gear | Strain wave gear*. URL: http://harmonicdrive.de/en/home/ (visited on 06/09/2017).

[43] *Harmonic drive*. en. Page Version ID: 766530853. Feb. 2017. URL: https://en.wikipedia.org/w/index.php?title=Harmonic_drive&oldid=766530853.

[44] *Comparison of Gear Efficiencies - Spur, Helical, Bevel, Worm, Hypoid, Cycloid*. URL: http://www.meadinfo.org/2008/11/gear-efficiency-spur-helical-bevel-worm.html (visited on 06/09/2017).

[45] *The World of Planetary Gears*. Mar. 2000. URL: http://www.machinedesign.com/motion-control/world-planetary-gears (visited on 06/08/2017).

[46] Nicolas Van der Noot, Auke J. Ijspeert, and Renaud Ronsse. "Biped gait controller for large speed variations, combining reflexes and a central pattern generator in a neuromuscular model". In: *Robotics and Automation (ICRA), 2015 IEEE International Conference on*. IEEE, 2015, pp. 6267–6274. URL: http://ieeexplore.ieee.org/abstract/document/7140079/ (visited on 06/08/2017).

[47] *CMA-ES*. en. Page Version ID: 759814959. Jan. 2017. URL: https://en.wikipedia.org/w/index.php?title=CMA-ES&oldid=759814959.

[48] *Robotran - Home*. URL: http://www.robotran.be/ (visited on 06/01/2017).

[49] Diego A. Garcıa, Marta B. Rosales, and Rubens Sampaio. *Dynamic behavior of timber footbridges with stochastic mechanical properties*. URL: https://www.researchgate.net/publication/290378272_DYNAMIC_BEHAVIOR_OF_TIMBER_FOOTBRIDGES_WITH_STOCHASTIC_MECHANICAL_PROPERTIES (visited on 06/03/2017).

[50] Soran Aminiaghdam et al. "Increasing trunk flexion transforms human leg function into that of birds despite different leg morphology". en. In: *Journal of Experimental Biology* 220.3 (Feb. 2017), pp. 478–486. ISSN: 0022-0949, 1477-9145. URL: http://jeb.biologists.org/content/220/3/478 (visited on 06/07/2017).

[51] Nicolas Van der Noot et al. "Experimental validation of a bio-inspired controller for dynamic walking with a humanoid robot". In: *Intelligent Robots and Systems (IROS), 2015 IEEE/RSJ International Conference on*. IEEE, 2015, pp. 393–400. URL: http://ieeexplore.ieee.org/abstract/document/7353403/ (visited on 06/08/2017).

[52] Christophe Everarts. "Infinitely Variable Transmission Design for Lower Limb Prosthesis Applications". unpublished technical report. 2014.

[53] Joško Deur et al. "Modeling and Analysis of Active Differential Dynamics". In: *Journal of Dynamic Systems, Measurement, and Control* 132.6 (Oct. 2010), pp. 061501–061501–14. ISSN: 0022-0434. URL: http://dx.doi.org/10.1115/1.4002482 (visited on 06/04/2017).

[54] *Gears of MISUMI | MISUMI*. URL: http://www.misumi-europe.com/en/catalog/vona2/maker/misumi/mech/M1000000000/M1006000000/ (visited on 06/08/2017).

[55] *About Power Springs*. URL: http://www.spiral-spring.com/about_power_springs.html (visited on 06/08/2017).

[56] *Calculate Mainspring Length | Horology - The Index*. URL: http://www.nawcc-index.net/CalcMainspringLength.php (visited on 06/08/2017).

Appendices

A Specifications

21/02/2017	Students	**Specifications** Version 1.2
Context **"Development of a humanoid walker: simulation, control and design."** The purpose of this master thesis is to validate the principle of multiple actuation with IVTs in a 2D bipedal robot with four degrees of actuation.		
Date	Origin	
		Functions:
28/09/2016	Advisor	**F1**: Be a bipedal robot
28/09/2016	Advisor	**F2**: Use multiple actuation
28/09/2016	Advisor	**F3**: Move in the sagittal plane solely (2D)
28/09/2016	Advisor	**F4**: Have a humanoid walking gait
		Functional requirements (FR) criteria and levels:
28/09/2016	Advisor	**FR1.1**: Composed of five bodies (two calves, two thighs and one trunk) and four compliant joints (two hips and two knees)
28/09/2016	Advisor	**FR1.2**: No feet, no ankle
28/09/2016	Advisor	**FR2.1**: Actuation of all joints by a single power motor, using differentials and IVTs
07/10/2016	Advisor	**FR3.1**: Straight path and/or circular path (radius of 2 [m])
25/10/2016	Advisor	**FR4.1**: Torque controlled joints
18/11/2016	Advisor	**FR4.2**: Based on the neuromuscular model (Geyer 2010)
		Constraints:
28/09/2016	Advisor	**C5**: Size limits
21/02/2017	Advisor	**C6**: All the powertrain contained in the trunk
21/02/2017	Students	**C7**: Off-board electric power supply
		Constraints requirements (CR) criteria and level:
28/09/2016	Advisor	**CR5.1**: Respect given dimensions (about half the size of a human)
21/02/2017	Advisor	**CR6.1**: Only the transmission to the knee is allowed on the leg
21/02/2017	Students	**CR7.1**: Connected to a standard electrical plug: 220-230 [V], 50 [Hz]

Rue Archimède, 1 bte L6.11.01, 1348 Louvain-la-Neuve **www.uclouvain.be/epl**